Mechanistic Insights from the ^{15}N-Site Preference of Nitrous Oxide utilizing High Resolution Near-Infrared *cw* Cavity Ringdown Spectroscopy and Density Functional Theory Calculations

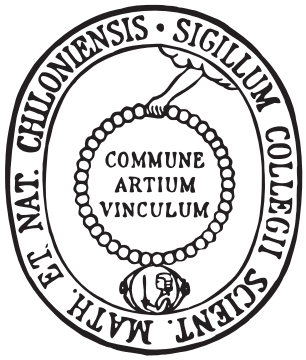

Dissertation
in fulfillment of the requirements
for the degree
"**Dr. rer. nat.**"
of the Faculty of Mathematics and Natural Sciences
at Kiel University

submitted by

Dipl.-Chem. Carsten Fehling

Kiel, 2012

Carsten Fehling: *Mechanistic Insights from the ^{15}N-Site Preference of Nitrous Oxide utilizing High Resolution Near-Infrared cw Cavity Ringdown Spectroscopy and Density Functional Theory Calculations* , © 2012

FIRST REFEREE:	Prof. Dr. Gernot Friedrichs
SECOND REFEREE:	Prof. Dr. Martin Beyer
DATE OF THE ORAL EXAMINATION:	March 28, 2012
APPROVED FOR PUBLICATION:	March 28, 2012
SIGNED:	Prof. Dr. Lutz Kipp, Dean

Für meine Eltern

ABSTRACT

The ^{15}N-site preference, the ratio between the single ^{15}N-substituted nitrous oxide isotopomers $^{14}N^{15}N^{16}O$ and $^{15}N^{14}N^{16}O$, is discussed as an important proxy for formation and decomposition pathways of N_2O in environmental sciences. So far, calibration problems in mass spectrometric techniques complicated its accurate determination. In this thesis, an alternative approach to determine this parameter based on cavity ringdown spectroscopy has been investigated and the detailed formation mechanism of N_2O from HNO dimerization has been assessed.

In the first section, the detailed setup of a novel ultrasensitive cavity ringdown spectrometer combined with a Fourier transform based high resolution wavelength calibration scheme is described. Using an external cavity diode laser system as a light source, the temperature stabilized spectrometer enabled sensitive gas phase absorption measurements down to minimum absorptions of $1 \times 10^{-9}\,\mathrm{cm}^{-1}$ in the wavelength range from 1620 to 1690 nm and with an absolute accuracy in spectral resolution of $\Delta\lambda/\lambda = 1 \times 10^{-7}$.

In a next step, a combination of high resolution ion cyclotron resonance mass spectrometry and high resolution cavity ringdown spectroscopy was used to characterize the precise isotopologue composition of highly ^{15}N-isotopically enriched samples of the two N_2O isotopomers. These samples were used to determine accurate absorption line strengths and broadening parameters of isolated rotational-vibrational transitions in the 3001←0000 band of the corresponding nitrous oxide isotopomers. Following a strategy of selective detection of the isotopomers to determine the ^{15}N-site preference, it was possible to verify previous IRMS measurements indicating a clear preference of $^{14}N^{15}N^{16}O$ formation in the selective inorganic reduction of nitrite in aqueous solution.

Furthermore, DFT based calculations have been used to investigate the mechanism underlying the nitrous oxide formation from nitroxyl dimerization. It could be shown that previous mechanistic assumptions are basically inconsistent with experimental results. Consequently, a new mechanism mainly based on a fast acid-base equilibration scheme has been worked out. Here, solvation effects suggested a change of *cis-trans* preference in favor of the *cis* dimer in the initial dimerization reaction. Moreover, the final step forming nitrous oxide was related to the previously unconsidered *cis*-hyponitrite anion. The acid-base equilibrium of the latter reveals remarkable differences compared to the *trans* isomer. Additional experiments and kinetic simulation underlined the feasibility of the fundamentally new mechanism. Finally, isotopomer analysis of nitrous oxide from *trans*-hyponitrous acid decomposition yielded a significantly different site preference compared to HNO dimerization. As the associated reaction dynamics of the hyponitrite isomers could be understood in terms of molecular orbital theory arguments, inclusion of the underlying reaction schemes enabled theoretical confirmation of the experimental results. Interesting parallels to site preferences found for diverse biochemical formation pathways are discussed.

ZUSAMMENFASSUNG

Das Verhältnis der ^{15}N-substituierten Isotopomere von Lachgas, $^{14}N^{15}N^{16}O$ und $^{15}N^{14}N^{16}O$, die sogenannte ^{15}N-Vorzugsposition, wird als interessanter Parameter zur Charakterisierung von Bildungs- und Abbaumechanismen von N_2O in den Umweltwissenschaften diskutiert. Da bisher die exakte Bestimmung dieses Parameters durch Kalibrierungsprobleme der Massenspektrometrie erschwert wird, wurde in dieser Arbeit ein auf der Cavity-Ringdown (CRD) Spektroskopie basierender, alternativer Weg zu dessen Bestimmung untersucht und zusätzlich der Bildungsmechanismus von N_2O durch Dimerisierung von HNO analysiert.
Im ersten Teil der Arbeit wird der Aufbau eines neuen CRD-Spektrometers in Kombination mit einer Fourier-Transformations-Methode zur exakten Wellenlängenbestimmung detailliert beschrieben. Mit dem temperaturstabilisierten Spektrometer konnten im Wellenlängenbereich von 1620 bis 1690 nm sehr empfindlich Absorptionsspektren ($\alpha_{min} < 1 \times 10^{-9}\,cm^{-1}$) mit einer absoluten spektralen Auflösegenauigkeit von $\Delta\lambda/\lambda = 1 \times 10^{-7}$ aufgenommen werden.
Mittels einer Kombination von FT-ICR-Massenspektrometrie und CRD-Spektroskopie wurde daraufhin die Isotopologenzusammensetzung von hoch-angereicherten Proben der beiden N_2O-Isotopomere bestimmt. Diese Proben wurden für eine genaue Bestimmung der Absorptionslinienstärke und der Linienverbreiterungsparameter einzelner isolierter Schwingungs-Rotations-Übergänge der beiden N_2O-Isotopomere verwendet. Darauf aufbauend gelang es, die ^{15}N-Vorzugsposition optisch zu bestimmen. Die Methodik wurde durch Vergleich mit massenspektrometrisch gewonnenen Literaturdaten, die eine bevorzugte Bildung von $^{14}N^{15}N^{16}O$ bei der selektiven anorganischen Reduktion von Nitrit in wässriger Lösung zeigten, verifiziert.
Weiterhin wurden theoretische DFT-Rechnungen durchgeführt, um den Mechanismus der N_2O Bildung bei der Dimerisierung von HNO in Lösung aufzuklären. Da die experimentellen Ergebnisse von bisher vorgeschlagenen Mechanismen nicht ausreichend wiedergegeben werden konnten, wurden verschiedene Modelle untersucht. Ein neuer auf schnellen Säure-Base-Reaktionen basierender Mechanismus zeigte, dass eine bevorzugte Bildung des *cis*-HNO-Dimers im primären Reaktionsschritt erfolgt und für die N_2O-Bildungsreaktion der Zerfall des bisher weitgehend unberücksichtigten *cis*-Hyponitritanions maßgeblich ist. Zudem weist das Säure-Base-Gleichgewicht des *cis*-Hyponitritanions erhebliche Unterschiede zum bisher besser bekannten *trans* Isomer auf. Kinetische Simulationen und zusätzliche Experimente wurden zur Verifizierung verwendet.
Im letzten Teil der Arbeit konnte schließlich gezeigt werden, dass die Zersetzung von *trans*-Hyponitrit eine deutlich andere Isotopomerensignatur von N_2O liefert. Ausgehend von Molekülorbitalbetrachtungen konnte die unterschiedliche Reaktionsdynamik der Zersetzungsreaktionen beider Isomere theoretisch erklärt werden. Unter Berücksichtigung der zugrundeliegenden Kinetik gelang es ferner, die experimentellen Ergebnisse nachzuvollziehen. Abschließend werden interessante Parallelen mit der in biochemischen Bildungswegen beobachteten Isotopomerenpräferenz diskutiert.

CONTENTS

LIST OF FIGURES

LIST OF TABLES

ACRONYMS

CRD	cavity ringdown
CRDS	cavity ringdown spectroscopy
CEAS	cavity enhanced absorption spectroscopy
FMS	frequency modulation spectroscopy
WMS	wavelength modulation spectroscopy
EIE	equilibrium isotope effect
KIE	kinetic isotope effect
DFB	distributed feedback
ECDL	external cavity diode laser
BO	Born Oppenheimer
DFT	density functional theory
HF	Hartree-Fock
PCM	polarizable continuum model
NIR	near infrared
FTIR	Fourier transform infrared
ODS	ozone-depleting substance
QCL	quantum cascade laser
IRMS	isotope ratio mass spectrometry
FT-ICR	Fourier transform-ion cyclotron resonance

1 INTRODUCTION

It is not the possession of truth,
but the success which attends the seeking after it,
that enriches the seeker and brings happiness to him.

— Max Planck (1858 - 1947)

1.1 EARTH'S ATMOSPHERE AND THE CLIMATE SYSTEM

The changes in earth's atmosphere have already affected human life in many different ways. In the past and present, for example, air pollution has influenced human health and acid rain has lead to dramatic effects on nature. The currently most frequently and to certain extent controversially discussed issue is the changing climate system and its impact on future human life.[1] Numerous climate models predict an increasing global temperature and high fluctuations of extreme weather conditions such that decision makers are faced with the serious question whether active countermeasures will have a reasonable effect on preventing these scenarios to come true. In order to give reliable answers to many related questions, it is necessary to understand the changes in the atmosphere in general and, in particular, the details of the climate system.
Basically, the atmosphere can be described as an interplay of physical (motion, dynamics and energy) and chemical (composition and reaction) processes. The early energetic picture of the atmosphere drastically changed when first Fourier (qualitative) in 1827, then Arrhenius[2] (quantitative) in 1896, and finally Keeling[3] (systematic measurements) in the sixties of the past century recognized the influence of the so called 'greenhouse gases' for the earth heat balance. In a simplified model for the earth radiation balance, the black body radiation emitted from the sun is effectively filtered in the upper atmosphere for its UV spectral content and, except for scattering and reflection from clouds and particles, the residual radiation penetrates the earth's atmosphere unaffected and is either reflected or absorbed at the surface. The absorbed radiation is considered to account for the major part of the thermal surface energy and leads to a significant increase of the surface temperature. The earth, a black body emitter itself, loses thermal energy by emission of radiation with a maximum in the infrared spectral region corresponding to the lower surface temperature. In such a simple reductive model, an effective temperature of approximately 255 K (-18 °C) would result in equilibrium. At this point, the presence of the greenhouse gases in the atmosphere comes into play by affecting the radiation balance due to absorption and reemission of terrestrial infrared radiation such that parts of thermal energy are stored in earth's atmosphere. Consequently, the average surface temperature is significantly higher. The overall average temperature increase due to the presence of greenhouse gases is stated to be on the order of 33 K such that a mean temperature of 288 K (15 °C) results. Thus, the pure existence of the greenhouse effect is considered to enable life on earth.

The prerequisite of acting as a greenhouse gas is the ability of a gas to absorb infrared radiation. According to quantum mechanics, this implies a changing dipole moment during a molecular vibration that interacts with the light field. This general selection rule excludes major permanent constituents of the atmosphere (N_2, O_2 and the noble gases) to act as a greenhouse gas. Beside H_2O with the largest but strongly varying contribution, only certain trace gases, which are present in very low concentrations, need to be considered. The range of possible compounds persisting in the overall quite constant composition of the troposphere is further limited by tropospheric chemistry. For example, the lifetime of many organic compounds in the troposphere is extremely short such that no accumulation in the atmosphere takes place. In most cases it is the high reactivity of these compounds with OH that limits the lifetime. Therefore, the ultra trace species OH is denoted as detergent of the atmosphere. Another frequent decomposition pathway is photolysis; but due to the effective filtering of UV light in the stratosphere only compounds exhibiting absorption bands in the visible and near ultraviolet spectral region are affected.
According to the recent IPCC report (2007),[4] next to H_2O, the three most important greenhouse gases are carbon dioxide, methane and nitrous oxide with atmospheric concentrations of approximately 380 ppm, 1.8 ppm and 320 ppb, respectively. The analysis of gas samples preserved inside ice cores revealed that concentrations of all three gases have significantly increased since the beginning of the industrial age (278 ppm, 715 ppb and 270 ppb, respectively). This increase has basically been attributed to an additional input from anthropogenic sources such as fuel combustion in the case of carbon dioxide and agricultural changes in the case of methane and nitrous oxide.[1]
Precise measurements of the small concentration changes require very sensitive and quantitative detection techniques. Therefore, in the field of atmospheric sciences, especially optical spectroscopy and mass spectrometry (often in combination with gas chromatographic separation) are applied for this purpose.[5] However, due to fast gas mixing in the troposphere these concentration measurements provide no precise assignment of these trace gases to their corresponding sources.
Further information on the global fluxes of the gas of interest is often derived from isotope patterns, but isotope enrichment and depletion can originate from several processes such as chemical formation mechanisms, physical phase changes and specific biological metabolisms.[6] Thus, the informative value of a single isotopic measurement is often ambiguous and multiple isotope measurements and/or correlations are needed to certify the conclusions drawn from it. Experimentally, these precise isotope measurements are very demanding, because each of the applied techniques is affected by its own specific drawbacks.

1.2 THE DIVERSE ROLES OF NITROUS OXIDE IN EARTH'S ATMOSPHERE

Nitrous oxide, N_2O, at the time being frequently named the forgotten (atmospheric) gas,[7] has a quite significant effect in the troposphere and in the stratosphere as well (see Figure 1.1). Despite its low tropospheric concentration, its long term (100 yr) global warming potential has been estimated to be 300 times that of carbon dioxide such that it contributes approximately 6% to the overall radiative forcing in the atmosphere.[4] This high impact as a greenhouse gas originates partly from its

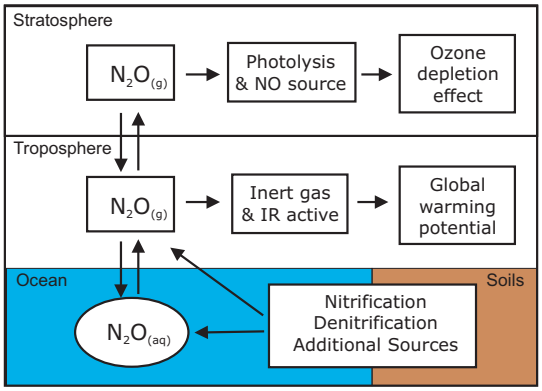

Figure 1.1: Impact of nitrous oxide formation affecting earth's radiation balance as a greenhouse gas in the troposphere and as an effective ozone depletion agent in the stratosphere.

long atmospheric lifetime of 114 years due to the absence of possible decomposition pathways in the troposphere. On the one hand, the possible reaction with OH forming a hyponitrite radical has been calculated to be very slow.[8] On the other hand, photolysis of N_2O requires wavelengths below 230 nm and hence is irrelevant in the troposphere as well.
In contrast, besides the reaction with $O(^1D)$ (10 %), photolysis turned out to be a major destruction pathway (90 %) for nitrous oxide in the stratosphere.

$$N_2O \xrightarrow{h\nu} N_2 + O(^1D) \tag{1.1}$$
$$N_2O + O(^1D) \rightarrow N_2 + O_2 \tag{1.2}$$
$$N_2O + O(^1D) \rightarrow 2\ NO \tag{1.3}$$

In fact, the occurrence of these reactions have important consequences for the composition of the stratosphere. The works of Crutzen[9] and Johnston[10] in the 1970s revealed that the formed NO can react according to the following catalytic cycle

$$NO + O_3 \rightarrow NO_2 + O_2 \tag{1.4}$$
$$NO_2 + O(^1D) \rightarrow NO + O_2 \tag{1.5}$$
$$\text{net reaction: } O_3 + O(^1D) \rightarrow 2\ O_2 \tag{1.6}$$

This catalytic cycle results in an effective destruction of ozone in the stratosphere. As a consequence of the effective decrease of the banned hydrochlorofluorocarbon emissions, Ravishankara *et al.*[11] pointed out that nitrous oxide is and will be the dominant ozone-depleting substance (ODS) in the stratosphere of the 21^{th} century.
Due to the significance as tropospheric sink and stratospheric ODS, efforts have been undertaken to gain information of the underlying kinetics. As predicted earlier, both photolysis and $O(^1D)$ reactions are affected by isotopic fractionation.[13] It is quite constant in the case of $O(^1D)$ reactions and significantly wavelength dependent and temperature dependent in the case of nitrous oxide photolysis. The combined effect is an enrichment of the heavier ^{15}N containing isotopologues in the stratosphere, which was verified by airborne measurements. Subsequent modeling approaches showed that isotopic patterns of the troposphere could be well explained by fluxes of

Table 1.1: Estimates of nitrous oxide emissions and decomposition from different sources and sinks affecting the atmospheric budget in Tg N yr^{-1}.[1,12]

N_2O sources	total natural	**10 - 12**
	soils	8 - 10
	oceans	2
	total anthropogenic	**3.7 - 7.7**
	cultivated soils	1.8 - 5.3
	cattle and feed lots	0.2 - 0.5
	biomass burning	0.2 - 1.0
	industrial	0.7 - 1.8
N_2O sinks	total stratospheric loss	**11.9**
	N_2O photolysis	10.7
	$O(^1D)$ reactions	1.2
Tropospheric inventory	increase	**3.9**

heavy isotopologues from the stratosphere. Refined isotopic investigations pointed out that the two single ^{15}N substituted nitrous oxide isotopomers, $^{14}N^{15}N^{16}O$ and $^{15}N^{14}N^{16}O$, undergo a quite different fractionation and, in addition to bulk ^{15}N enrichment, its ratio (the so called site preference) might be highly informative for determining global fluxes.[14] Despite calibration problems of the mass spectrometric technique used for site-preference determination,[15] such measurements contributed to characterize the decomposition of the stratospheric sink, which is now comparatively well understood.[12]

In contrast, contributions of different sources of nitrous oxide to the tropospheric inventory are rather uncertain. Table 1.1 lists estimates of sources and sinks of different processes as taken from Crutzen *et al.*[12] and Möller.[1] Natural sources cover mainly biological nitrous oxide production in soils and oceans, whereas anthropogenic sources are dominated by agricultural and industrial contributions. Although the given values of the sources cover a quite large range, in numerous studies further (in some cases controversial) corrections have been suggested. For example, Bange[16] pointed out that oceanic contributions are underestimated because of additional significant contributions of the coastal areas, whereas Rhee *et al.*[17] suggested a much lower contribution based on their field measurements. Thus, one of the major problems with estimating the source strength of nitrous oxide lies in the biogenic sources varying with high temporal and local fluctuations. This is in particular problematic for the often followed bottom-up approach (e.g., pursued in the IPCC report 2007[4]) to determine the global budget. Therefore, Crutzen *et al.*[12] presented a quite consistent top-down approach to determine the anthropogenic input making use of the well characterized atmospheric sink and the accurately known global concentration of nitrous oxide. But this estimation did not enable detailed source assignments.

Inspired by the successful work of characterizing the stratospheric sink using isotopomer ratios, the concept of using isotopomer ratios to characterize sources came up. In a series of empirical isotope ratio mass spectrometry (IRMS) studies, Toyoda and Yoshida[18–20] as well as Sutka and Ostrom[21–23] presented isotopomer ratios of numerous sources. Indeed, these studies revealed source specific values for certain nitrous oxide forming bacteria and fungi as well as chemical reactions. Simultaneously, several N_2O site preference field measurements have been performed. In natural environments such as forests and grassland[24] as well as anthropogenic sources such as biogas and wastewater treatment plants,[25,26] N_2O has been shown to exhibit significant variations in the isotopomer ratio depending on its formation mechanism.

1.3 PATHWAYS OF NITROUS OXIDE FORMATION

Natural nitrous oxide formation in oceans and soils is basically considered to be biogenic as part of the nitrogen cycle. The nitrogen cycle as a whole describes the biochemical conversion pathways of natural nitrogen species and can be dissected into *fixation*, *nitrification*, *denitrification*, *assimilation*, and *mineralization*. Formation of nitrous oxide takes place as part of *nitrification* and *denitrification*.[1]
Nitrification is an aerobic process in which ammonia is oxidized sequentially by enzymes forming finally nitrate according to

$$NH_4^+ \xrightarrow{AMO} NH_2OH \xrightarrow{HAO} NO_2^- \xrightarrow{NXR} NO_3^- \tag{1.7}$$

Nitrous oxide is considered to be a byproduct of hydroxylamine oxidation.
In contrast, *denitrification* is an anaerobic process describing the reduction of nitrate towards molecular nitrogen according to

$$NO_3^- \xrightarrow{NAR} NO_2^- \xrightarrow{NIR} NO \xrightarrow{NOR} N_2O \xrightarrow{N_2OR} N_2 \tag{1.8}$$

Here, nitrous oxide appears as an intermediate arising from nitric oxide dimerization catalyzed by nitric oxide reductase followed by reduction towards molecular nitrogen. At least two structurally different nitric oxide reductase (NOR) enzymes are known from bacteria (norBC) and fungi (P450nor), containing two and one iron center located at the active site, respectively. In addition to this, dimerization of NO is also possible via catalysis of the bacterial ba3 oxidase, which contains a copper center instead of a second iron center. First single crystal structures of bNOR became only recently available by Hino *et al.*[27] and are shown in Figure 1.2. Despite this deeper structural understanding, the actual mechanisms of N-N bond formation and N-O bond cleavage are still subject of discussion.[28]
In the case of bacterial NOR, three different mechanisms have been discussed, the *trans* mechanism, the *cis*-heme b3 mechanism, and the *cis*-Fe_B mechanism. These mechanisms differ in the coordination site of nitric oxide by assuming coordination of NO at both metal ions each, simultaneous coordination of the two NO at the non-heme Fe_B, or a sequential coordination mechanism at the heme iron, respectively. In most cases, density functional theory (DFT) calculations assisted by spectroscopic studies have been performed to support the stable key intermediates and to suggest a valid reaction sequence. Typically, a hyponitrite species is postulated to be the final intermediate that decomposes to form nitrous oxide. For example, Varotsis *et al.*[29]

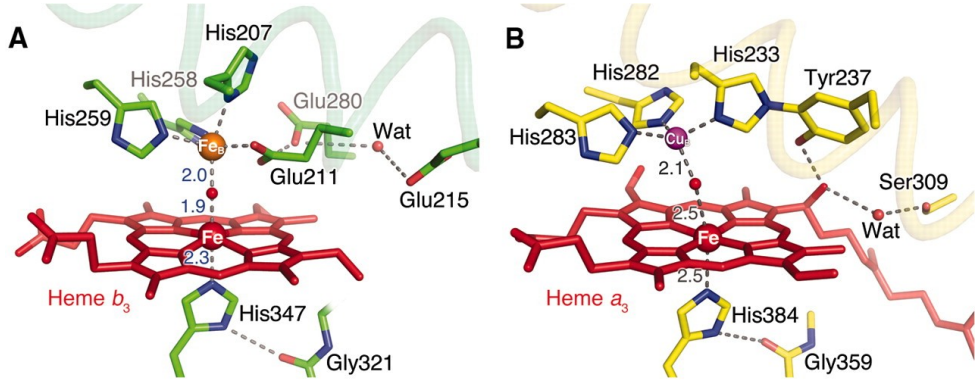

Figure 1.2: Active sites of nitrous oxide reductase (cNOR) (A) and b3 oxidase (B) as determined by crystal structure analysis from isolated enzymes. Both structures with two metal centers are known to catalyse NO dimerization towards N_2O formation. From Hino *et al.*, *Science* **2010**, *330*, 1666-1670. Reprinted with permission from AAAS.

presented calculations of a stable *trans*-hyponitrite complex and recent synthesis approaches of Xu *et al.*[30] indeed were able to isolate hyponitrite-heme-complexes of certain stability.

Fungal denitrification involves the better characterized P450nor containing only a single heme-iron center and nitrous oxide formation follows a different mechanism. Detailed calculations of the intermediate structures pointed out that an iron-*cis*-hyponitrite-complex is formed and sequential decomposition of *cis*-hyponitrite finally yields nitrous oxide.[31,32]

Prior to this detailed analysis of nitric oxide reductase, the final formation of nitrous oxide had been suggested to originate from a non-enzymatic reaction.[33] After enzymatic reduction of NO, free nitroxyl (HNO) was considered to undergo rapid dimerization according to

$$HNO + HNO \rightarrow [HONNOH] \rightarrow N_2O + H_2O \tag{1.9}$$

Although no intermediates could be observed experimentally, hyponitrous acid (*cis*) had been suggested as transient intermediate finally forming nitrous oxide. The same reaction was considered to be responsible for nitrous oxide formation as byproduct of *nitrification* under *anaerobic* conditions. In very recent discussions concerning the involvement of archaea as an important group of single-cell microorganisms in connection with the nitrogen cycle, the relevance of this reaction was discussed as well.[34]

Another non-enzymatic nitrous oxide formation pathway is the comproportionation reaction of hydroxylamine with nitrous acid. This reaction has been studied to take place under acidic conditions or in presence of certain anionic species according to[35–37]

$$H_3NOH^+ + HNO_2 \rightarrow [HONNOH] + H_3O^+ \rightarrow N_2O + H_2O + H_3O^+ \tag{1.10}$$

This net reaction follows a complex reaction mechanism involving numerous intermediates in solution. It finally yields nitrous oxide and varying amounts of *trans*-hyponitrite as byproduct. Whereas the latter is stable under the reaction conditions,

the formed nitrous oxide has been assigned to originate from the unstable intermediate *cis*-hyponitrite. A pathway through a symmetric intermediate [HONNOH] structure is consistent with ^{15}N-isotope tracer studies that showed an almost equal distribution of ^{15}N in nitrous oxide independent of the initial educt labeling. In order to explain the observed rate increase under acidic conditions, it was suggested that the mechanism depends on initial NO^+-adduct formation from nitrous acid and an available anion followed by nitrosation of hydroxylamine. Recently, attempts to understand the underlying mechanism based on DFT calculation have been presented, but certain difficulties to model the detailed kinetics of this system remained.[38–40] Under physiological conditions this reaction is of minor significance due to the absence of NO^+ activation. However, enzymatic isotope studies revealed that increased nitrous oxide formation occurs if an additional nitrogen source being not convertible by the enzyme itself is available.[41] Recently, Spott *et al.*[42] came to the conclusion that the possibility of enzymatic NO^+-adduct formation followed by nitrosation and decomposition of a non-enzyme bound species might exist as additional pathway termed codenitrification, which was largely unrecognized in related discussions.
Summarized, nitrous oxide formation is mainly considered to be related to chemical and biochemical conversion of hydroxylamine, nitroxyl, and nitrite. In almost all cases, the final decomposition pathways are postulated to include hyponitrite species. Consequently, Toyoda *et al.*[19] suggested that (*i*) the site preference of a nitrous oxide source is directly connected with the decomposition of the respective symmetric hyponitrite species and that (*ii*) measurements of chemical reactions forming nitrous oxide reflect the isotope effect of N-O bond cleavage. This interpretation of the origin of site preference was supported by the theoretical considerations of Schmidt *et al.*[43] based on earlier calculations and experiments. They underlined the necessity of an isotope effect occurring in the chemical reactions, but contradicted the earlier statement of Stein and Yung[44] that isotopomer formation would follow a statistical distribution and isotopic discrimination at the enzymatic iron centers would be the reason for isotopomer changes. The possible role of the *cis*/*trans* isomer structure, which will be discussed in some detail in this thesis, has so far not been addressed in this context.

1.4 OBJECTIVE AND UNDERLYING RESEARCH STRATEGY

In order to gain a better understanding of the global nutrient cycles and its impact on the atmosphere, refined tools are needed that allow one to identify sources and sinks of trace gases. In the case of nitrous oxide, the approach of isotopomer selective detection holds potential to overcome the drawbacks of bulk isotope measurements such as the influence of the isotopic composition of the source. Isotopomer enrichment in the stratosphere serves as a good example for such an approach. Compared to standard isotopic measurements, the independence from isotopic abundance of the source and the progress of the reaction is clearly advantageous.
Despite the quite successful measurements, ongoing discussions regarding the calibration of specially designed isotope ratio mass spectrometers used for this purpose suggest applications of other, possibly more suitable techniques. As a very sensitive and quantitative optical technique, cavity ringdown spectroscopy (CRDS) is a potential candidate for such a isotopomer selective detection scheme. Recent progress in

diode laser technology made available tunable narrow-band laser systems in the near-infrared range that serve as suitable light sources for high-resolution detection of N_2O. Accurate, precise, and reproducible line shape measurements are needed to enable highly accurate line strength measurements. In this context, chapter 2 describes the setup of a novel continuous wave cavity ringdown spectrometer making use of a Fourier transform wavelength calibration.

Application of this spectroscopic technique for isotopomer measurements, requires the determination of line strength parameters for selected rotational-vibrational transitions of the N_2O isotopomers in the near infrared. Therefore, in chapter 3 measurements on pure isotopomer samples, which have been characterized by high resolution mass spectrometry beforehand, were used to determine accurate integrated line strength and line shape parameters. The potential and the achieved accuracy of this approach will be discussed.

Another open question addresses the intermediates and reaction pathways of the significant but poorly understood HNO dimerization reaction. Corresponding experiments performed by Toyoda *et al.*[19] indicated that a significant isotopomeric effect exists. Due to the fact that the previously suggested reaction mechanisms turned out to be quite inconsistent with experimental results, an investigation based on quantum chemical DFT calculations and subsequent kinetic modeling appeared reasonable (chapter 4).

Finally, two different isomer structures of hyponitrite have been found or have been predicted to play a role in the overall decomposition mechanism. The effect of the structure of the N_2O precursor on the isotopomer ratio of the formed nitrous oxide has not been investigated so far. A theoretical quantum chemical study, corresponding kinetic modeling as well as experimental results will be presented to evalutate structure related effects (chapter 5).

2 SETUP OF A *CW* CAVITY RING-DOWN SPECTROMETER

Because a thing seems difficult for you,
do not think it impossible for anyone to accomplish.

— Marcus Aurelius (102 - 180)

2.1 SCOPE OF THE PROJECT

Light absorption has long been used to determine sample concentrations and the characteristics of absorption spectra frequently shed light on the molecular structure of matter. Early instrumentations typically utilized incoherent light sources, in combination with a dispersive element, a sample cell, and a light detector to determine the change of light intensity. The inherent noise of the light source and the detector remained a major problem limiting the quality and reproducibility. With the emergence of the laser as a highly coherent light source, more sophisticated techniques could be developed. Tunable, narrowband light sources were often used in combination with lock-in detection to improve the sensitivity by modulating the light source, termed wavelength modulation spectroscopy (WMS) at low modulation frequencies and frequency modulation spectroscopy (FMS) at high modulation frequencies. Furthermore, the low divergence of the laser beam enabled the realization of long absorption path lengths by use of White and Herriott multipass cells providing effective path lengths of several hundred meters. Even longer absorption path lengths on the order of hundreds of kilometers could be easily achieved using optical cavities formed by highly reflective mirrors, however, often the frequency dependent transmission of such an optical system turned out to be problematic. Therefore, first spectroscopic applications of optical cavities were based on schemes with absorption cells placed directly inside a laser cavity. Changes in the gain spectrum could then be converted into absorption.

A different approach making use of the spectral characteristics of optical cavities was presented by Anderson *et al.*[45] in 1984. Initially intended for mirror reflectivity measurements, the basic idea was to use the long decay times of the stored light field inside a cavity to gain information about the quality of the cavity. The first application of such decay time measurements for absorption measurements, i.e., the very weak absorption lines of oxygen in the visible range, can be attributed to O'Keefe and Deacon.[46] These measurements, which were based on pulsed laser systems, are commonly cited as the start of CRDS. Especially when dielectric mirrors with very high reflectivity became commercially available, the achievable sensitivity turned out to match or overcome those of conventional and often much more sophisticated traditional techniques.

However, improvement of the technique by ever increasing mirror reflectivity is limited due to the sharpening of the transmission fringes. Another intrinsic problem arose from the simultaneous excitation of several cavity modes yielding multi-exponential decays.[47] Consequently, by reintroducing narrowband continuous wave

(*cw*) laser systems, at least tenfold higher sensitivities could be obtained.[48] These *cw* techniques required (*i*) matching of laser frequency and cavity mode structure and, following the intensity built-up in the cavity, (*ii*) rapid switching of light source and cavity off-resonance to obtain an undisturbed single exponential decay. Whereas the first condition can be fulfilled by slow modulation of the laser light source or the cavity length, the second condition is usually been met by using fast optical switches.[48] Alternatively, it is possible to rapidly sweep the cavity.[49] Next to sensitivity gain, the higher experimental effort of *cw* CRDS commonly yields higher repetition rates (50 Hz up to 2 kHz) and a better wavelength accuracy than the pulsed setup.[50] The spectrometer characteristics can be even further improved by laser frequency stabilization techniques, but these require ultrastable cavities and additional locking devices.[51,52]

Beside sensitivity, spectral resolution is another aspect. In contrast to broadband light sources where additional external dispersive elements are used, spectral resolution of this narrowband laser spectroscopic technique is determined by linewidth of the laser emission and/or cavity transmission. Although a remarkable relative wavelength accuracy can be achieved by using the transmission frequencies of a stabilized cavity as a frequency scale, absolute wavelength determination of narrow bandwidth, not stabilized laser systems is crucial for high resolution spectrometers. In the case of the external cavity diode laser (ECDL) used in this work, the emission wavelength fluctuates due to influences of temperature, alignment, and imperfect coatings.[53] Hence, the achievable narrow laser line width of typically 500 kHz is only reached on a short time scale (20 ms). The effective line broadening on a 1 s time scale reaches 2 MHz and reflects the short term fluctuations. Typically, the long term drift adds up to 300 MHz after 24 h. Highly accurate spectral measurements therefore have to rely on in situ monitoring of the wavelength. Common tools for this purpose are etalons, gas cells for reference absorption, and commercially available wavelength meters, which are often based on Fizeau or Michelson type interferometers. The latter often provide an excellent choice, but the resolution necessary to resolve Doppler broadened rovibrational lines in the NIR faces the border of technical feasibility and is only achieved by high-end equipment.

In order to enable quantitative, sensitive, and selective detection of nitrous oxide isotopomers, the application of CRDS in combination with a continuous wave laser system and an accurate wavelength monitor appears a reasonable choice. In this work, a state-of-the-art ECDL has been tested for applicability and has been characterized in detail.

2.2 THEORETICAL BACKGROUND

2.2.1 *Cavity ringdown absorption spectroscopy*

Absorption spectroscopy in general describes the wavelength dependent attenuation of a static electromagnetic wave induced by passing the medium of interest. In the limiting case of weak electric fields and low absorption of the medium, it is termed

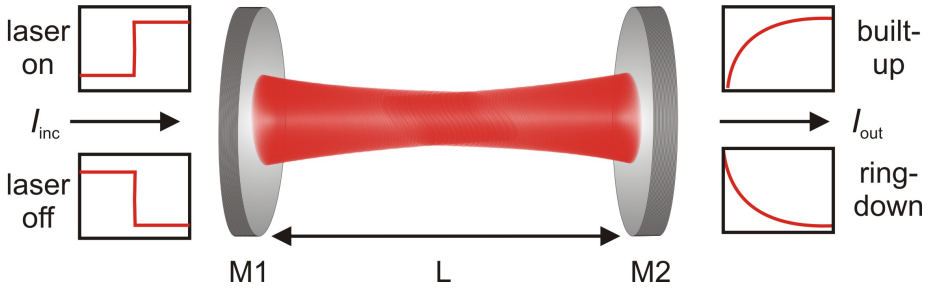

Figure 2.1: Schematic of the transmission of a resonant optical cavity forming a stable mode. In the upper and lower corners, the intensity increase and decrease behind the cavity after switching the laser is shown.

'linear' and the light intensity I after passing the medium of length l is related to the initial light intensity I_0 by Beer's law according to[54]

$$I(\nu) = I_0(\nu) \times \exp\left(-\alpha(\nu)l\right) = I_0(\nu) \times \exp\left(-\sigma(\nu)Nl\right). \tag{2.1}$$

Thus, an absorption coefficient $\alpha(\nu)$ is defined, which can be further dissected into number density N (or concentration c) of the absorbing species and the cross section of the transition, $\sigma(\nu)$. Usually, the napierian logarithm is used in gas phase measurements in contrast to the log-10 based logarithm typically used for condensed phase measurements.
A cavity as used for cavity ringdown spectroscopy is an optical system consisting of two or more mirrors with high reflectivity ($R > 0.995$). This system can be characterized in terms of stability parameters g_i, which are related to the radii r_i and distances d_{ij} of the mirrors used.

$$g_i = \left(1 - \frac{d_{ij}}{r_i}\right) \tag{2.2}$$

A two-mirror cavity is termed stable if the condition

$$0 < g_1 g_2 < 1 \tag{2.3}$$

holds. Such a cavity is capable to confine a light field inside, but at the same time it allows transmission only for wavelengths whose multiples coincide with the mirror distance. A quantitative description can be derived from etalon theory.[54]
The finesse F describes the quality of a cavity and is related to the mirror reflectivity by

$$F = \frac{\pi\sqrt{R}}{1 - R}. \tag{2.4}$$

With increasing finesse the mode structure of the cavity becomes more pronounced and the line width of the corresponding modes is given by

$$\delta\nu = \frac{c}{2\,L\,F} \tag{2.5}$$

with c as the speed of light and L the length of the cavity.
In general, the frequency of a resonant mode is given by the following expression

$$\nu_{qmn} = \frac{c}{2L}\left[q + \frac{n + m + 1}{\pi}\arccos(\sqrt{g_1 g_2})\right] \tag{2.6}$$

The difference between frequencies of two allowed modes (q_i,q_{i+1}) is known as the longitudinal mode spacing of the cavity $\Delta\nu_{\text{long}}$, which assumes a fundamental Gaussian mode at the center of the mirrors ($n = m = 0$). In cases with a light beam off-axis or for an imperfect alignment of the mirrors, additional transversal modes ($n \neq 0$ and/or $m \neq 0$) become stable resulting in an additional set of frequencies following the mode specific transversal distance of $\Delta\nu_{\text{trans},n,m}$.
For an empty cavity with identical mirrors as shown in Figure 2.1, the intensity transmitted through the cavity, I_{out}, is given by[55]

$$I_{\text{out}} = I_{\text{inc}} \times \frac{T^2}{(1-R)^2 + 4R\sin^2(\frac{\nu\pi}{\Delta\nu_{\text{long}}})} \tag{2.7}$$

with I_{inc} being the intensity of the incident light field and T the transmission of the mirrors. If the frequency of the incident light matches the corresponding frequency according to $\nu = \nu_{qmn}$, the maximum transmission, $T_{\text{max}} = T^2/(1-R)^2$, is reached, which in theory equals unity in case of negligible absorption and scattering of the mirrors. In real experiments this value is only on the order of a few percent, because - in addition to the previously mentioned processes - the coupling efficiency is typically below 100%. Provided resonance is maintained, a *cw* laser exhibiting a long coherence time and narrow line width will increase intracavity intensity until the maximum transmittance T_{max} is reached. The time necessary to build up intensity inside the cavity and achieve saturation depends on the mirror reflectivity. The efficiency of light injection into a cavity is therefore significantly better for a *cw* laser than that obtained with a pulsed laser system. Further improvement is obtained if active frequency-locking is used.[50]
After switching the incident wave off and assuming that intensity loss is only based on mirror reflectivity, the stored intensity inside the cavity I_0 decays according to

$$I_t = I_0 \times \exp\left(\frac{c\ln R(\nu)}{L}t\right) = I_0 \times \exp\left(-t/\tau_0(\nu)\right). \tag{2.8}$$

where τ_0 denotes the empty cavity decay time given by

$$\tau_0(\nu) = \frac{-L}{c\ln R(\nu)} = \frac{L}{c(1-R(\nu))}. \tag{2.9}$$

If an additional absorber with an absorption coefficient $\alpha(\nu)$ is present inside the cavity, Beer's law as in Equation 2.1 provides an additional loss term and Equation 2.8 changes to

$$I_t = I_0 \times \exp\left(\frac{c(\ln R(\nu) - \alpha(\nu)l)}{L}t\right) = I_0 \times \exp\left(-t/\tau(\nu)\right) \tag{2.10}$$

with τ, the cavity decay time including absorber loss, is given by

$$\tau(\nu) = \frac{L}{c(1-R(\nu)+\alpha(\nu)l)}. \tag{2.11}$$

Combining Equation 2.9 and Equation 2.11 and taking $L = l$ yields

$$\alpha(\nu) = \frac{1}{c} \times \left(\frac{1}{\tau(\nu)} - \frac{1}{\tau_0(\nu)}\right). \tag{2.12}$$

Thus, in contrast to conventional spectroscopy, the absorption coefficient $\alpha(\nu)$ is directly determined from the time constant measurement and is independent of the light intensity. This light intensity noise immunity together with the long effective absorption path length are the primal reasons for the extraordinary sensitivity of the cavity ringdown technique.

2.3 PUBLICATION I: A PRECISE HIGH-RESOLUTION NEAR INFRARED CONTINUOUS WAVE CAVITY RINGDOWN SPECTROMETER USING A FOURIER TRANSFORM BASED WAVELENGTH CALIBRATION

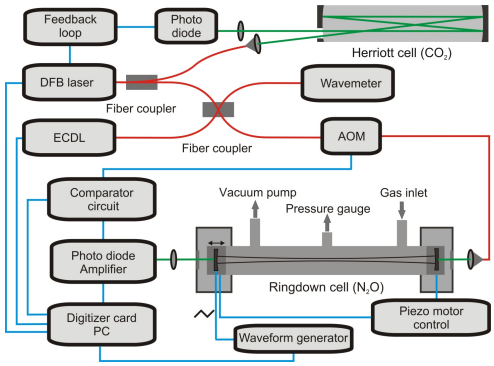

Own contributions to the paper:

- General concept of coupling ultra-sensitive *cw* cavity ringdown spectroscopy and FFT based difference frequency measurement for accurate wavelength determination.
- Planning and design of detection cell, vacuum system, electronics, and single mode fiber coupled laser system.
- Experimental setup of the *cw* cavity ringdown spectrometer and wavelength modulated reference laser system.
- Implementation of the complete instrument control software including a new synchronized, sequential real-time fitting algorithm in LabView.
- Measurements of N_2O test spectra and line strength parameters.
- Draft of the publication.

Additional work within this project, not presented in the paper:

- Further experimental improvements by introducing a more sensitive Herriott multi-pass cell for wavelength stabilization and design of a coupled temperature stabilization system via three independent feedback loops.

EXCERPT FROM THE PUBLICATION "A PRECISE HIGH-RESOLUTION NEAR INFRARED CONTINUOUS WAVE CAVITY RINGDOWN SPECTROMETER USING A FOURIER TRANSFORM BASED WAVELENGTH CALIBRATION"

Carsten Fehling and Gernot Friedrichs*[1]

Institut für Physikalische Chemie, Christian-Albrechts-Universität zu Kiel, Olshausenstr. 40, 24098 Kiel, Germany

ABSTRACT

A wavelength calibration technique is described, which is based on a combination of a Fourier transform wavelength meter and a distributed feedback laser locked to a molecular transition as a frequency marker in the spectrum. The technique provides a reliable wavelength scale to be used in high resolution continuous wave cavity ringdown spectroscopy without need for stabilization of the probe laser and accurately known molecular transitions in the scanned wavelength range. Due to a continuous reference measurement, ambient influences on the laser sources are effectively suppressed. As an example, we measured highly resolved cavity ringdown spectra of N_2O isotopomers and determined the line strength of several absorption lines at a wavelength around 1687 nm. A near infrared wavelength precision of 6×10^{-8} and an absolute accuracy on the order of 1×10^{-7} was readily achieved. The general concept is easy to implement and can be further refined by using additional reference lasers, thus holding the potential of even higher wavelength accuracy.

Full article available online:
URL: http://link.aip.org/link/doi/10.1063/1.3422254

1 Electronic mail: friedrichs@phc.uni-kiel.de

EXPERIMENTAL APPARATUS (EXCERPT FROM THE PUBLICATION)

The experimental setup is depicted in Figure E-1. In the following, the three main parts of the spectrometer consisting of wavelength calibration unit, cavity ringdown cell, and signal processing section will be described separately.

Wavelength Calibration Unit

The output of a fiber coupled distributed feedback laser system (Toptica DC 110, 1600.3 nm, 15 mW output power) was asymmetrically split by a 1×2 fiber coupler. Approximately 90% of the overall laser power was collimated and the free space beam, after passing a gas cell ($l = 50$ cm, $p(CO_2) = 80$ mbar) three times, was detected by an InGaAs photo detector (Thorlabs PDA10CF). Wavelength modulation of the diode laser (200 kHz modulation frequency, 200 MHz amplitude) and demodulation of the detector signal was used for top-of-fringe-locking of the laser output using feedback loop electronics (Toptica, Digilock 110). Modulation frequency was chosen with respect to the line width of the absorption line to achieve an undisturbed first derivative signal and was optimized according to the response function of the detection system when using the BIAS T circuit of the DFB diode for direct current modulation. The generated error signal was optimized by visual inspection of the signal when adjusting the modulation amplitude. According to the RMS error and the corresponding slope of the signal the frequency stability of the locked laser was determined to be on the order of 3×10^{-8}. In comparison with the stated absolute accuracy of the built-in HeNe laser (5×10^{-7}) this is more than one order of magnitude better. Note that the modulation frequency is high compared to the recording time of the interferogram such that the modulation, next to an insignificant line broadening, did not interfere with the reference wave number determination.
The R(28) line of the 30013e←00001e transition of CO_2 was chosen as reference line ($\tilde{\nu} = 6247.456238(40)\,\mathrm{cm}^{-1}$, $\Delta\tilde{\nu} = 0.0195\,\mathrm{cm}^{-1}$). Its line position was recently measured with high precision using laser based and Fourier transform based spectrometers by several authors.[1,2] In order to assure an accurate line center position, a minor collisional shift was taken into account based on the self pressure shift coefficient of $\delta = -0.00758(4)\,\mathrm{cm}^{-1}/\mathrm{atm}$.[3]
The remaining 10% of the DFB diode laser power were combined with the output of a fiber coupled external cavity diode laser (Sacher LION, Littman/Metcalf, 1620 - 1700 nm, 2 mW output power) and split again to 10% and 90% of the total power by a 2×2 fiber coupler.
The more intense beam was directed to a fiber coupled acousto-optic modulator (Neos, 80 MHz, 42 ns rise time). The first order diffracted beam was collimated and aligned to the optical axis of the ringdown cell. Only the output of the external cavity laser could be effectively coupled into the high-finesse cavity as the high frequency modulation of the DFB laser prevented an excitation of the sharp cavity resonances. The less intense laser beam was sent to a commercial multi-wavelength meter (EXFO WA-7100, 200 MHz accuracy). Inside the wavelength meter, the fiber output beam and a He-Ne reference laser beam were sent through a Michelson interferometer. A dichroic beam splitter divided the beams afterwards such that both beams were detected separately. The signal of the He-Ne laser provided an accurate means to

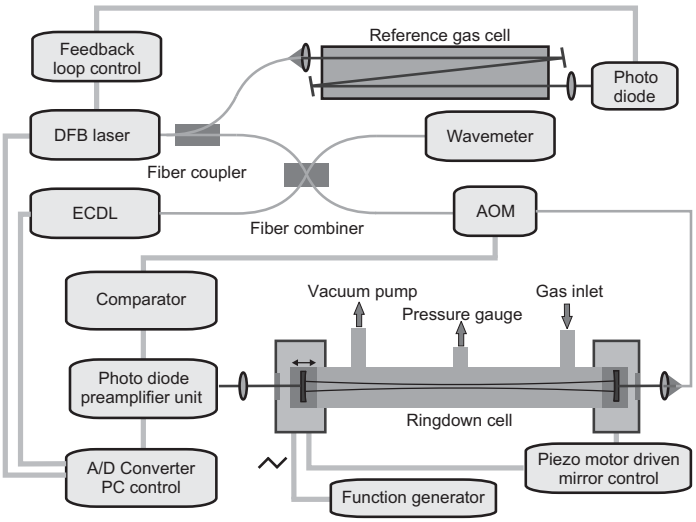

Figure E-1: Experimental setup. Light and dark gray thin lines represent fiber coupled and free-space beam lines, respectively, whereas thick lines indicate the electronic signal lines. DFB: distributed feedback laser, ECDL: external cavity diode laser, AOM: acousto-optic modulator, A/D Converter: analog-to-digital-converter.

determine the mirror displacement, and a fast Fourier transformation algorithm yielded the spectrum of the two incident laser beams. Figure E-2 displays a typical FT spectrum in logarithmic scale revealing that a high signal to noise ratio was observed for the two different laser wave numbers. Finally, the wave number of the ECDL as probe laser $\tilde{\nu}_{\mathrm{ECDL}}$, was calculated from the difference of the measured wave numbers of the two beams, $\Delta\tilde{\nu}$, according to

$$\tilde{\nu}_{\mathrm{ECDL}} = \tilde{\nu}_{\mathrm{Ref}} + \Delta\tilde{\nu} \tag{E-2}$$

where $\tilde{\nu}_{\mathrm{Ref}}$ corresponds to the wave number of the reference CO_2 absorption line.

Cavity Ringdown Cell

The ringdown cell consisted of two solid aluminum housings connected by a PTFE tube forming a flow cell. The whole system could be evacuated down to pressures of 10^{-2} mbar. In each housing a highly reflective mirror (Los Gatos Research, $R = 99.99\%$ at 1600 nm) was held in a vacuum compatible piezo motor driven mount, which permitted an external alignment of the mirror. The two concave mirrors ($r = 6$ m) formed a stable optical cavity with a mirror distance of 50 cm. One mirror was additionally mounted on a piezo ring actor (Piezomechanics) that moved the mirror along the optical axis. During the measurements, an applied triangle voltage (50 Hz) was used to shift the sharp resonance frequency of the cavity slightly more than one free spectral range. The pressure inside the cell was measured by two calibrated capacitance pressure sensors (MKS Baratron, 10 mbar and 1000 mbar). In order to prevent adsorption effects of the analyzed gases, the whole cavity was heated during the measurements to a temperature of approximately 333 K as measured by a

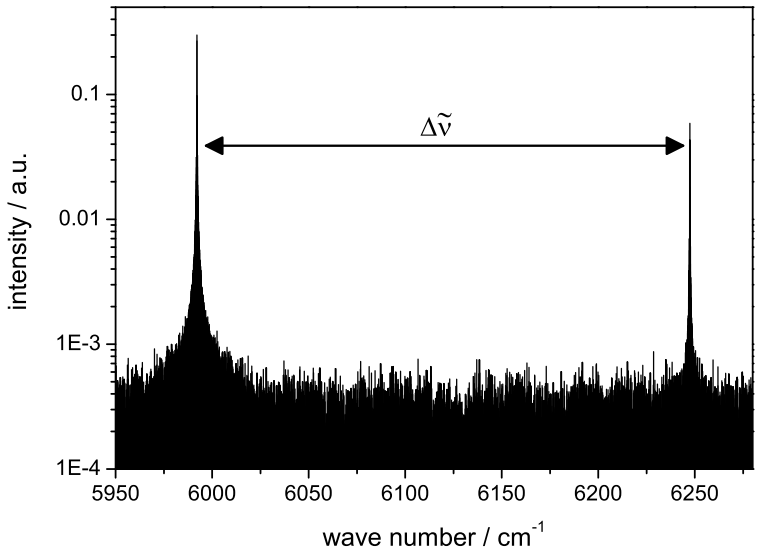

Figure E-2: Fourier transform spectrum resulting from the interferogram of the external cavity diode laser used for the cavity ringdown experiment ($\sim 6000\,\mathrm{cm}^{-1}$) and the frequency stabilized DFB laser ($\sim 6250\,\mathrm{cm}^{-1}$) used as frequency marker.

platinum resistance placed inside the cavity. The used gases were commercial grade carbon dioxide (CO_2, 99.995%) and nitrous oxide (N_2O, 99.999%).

Signal Processing

The laser beam was detected by a thermoelectrically cooled extended InGaAs photo diode (Judson, 10 MHz) and the corresponding photo current was amplified by a variable gain transimpedance amplifier (FEMTO DHPCA-100, 14 MHz, 10^4 V/A). The signal passed a comparator circuit which generated a TTL signal to switch off the acousto-optic modulator driver after a threshold for the intensity build-up was reached. The low-pass filtered (10 MHz) signal was digitized using a fast digitizer card (ZTEC, 14 bit, 200 MHz) and a home-written program (LabVIEW, NI, Version 8.51) was used for data processing.
The single exponential decays were analyzed in-situ as described by Lehmann and Huang.[4] Briefly, after subtraction of an approximated baseline, the logarithm of each decay was fitted using a weighted linear fit in order to obtain an estimate of the amplitude and the decay time. These parameters served as a set of input parameters for an iterative nonlinear Levenberg-Marquardt fit, which converged fast due to the reliable input parameters. Spectra were measured at wavelengths of 1670 - 1690 nm, which differed from the center wavelength of the used mirrors such that rather low ringdown times of approximately 15 µs were obtained. Usually, 50 decays were analyzed for each frequency step. Having checked for outliners, which rarely occurred, these values were averaged resulting in a standard deviation of the obtained decay constant on the order of 0.2%. This data acquisition and fitting procedure took approximately 2 s per data point, while the simultaneous wavelength determination was finished after 1.5 s. The wave number of the spectrum was finally corrected in order to take the constant frequency shift of the acousto-optic modulator into account.

Unfortunately, the baseline of the obtained spectra showed a reproducible oscillation. These baseline oscillations could be fitted to an Airy function with a corresponding optical path length that equaled the thickness of the mirrors. These effects have been reported by several authors[5,6] and were attributed to interference effects due to a missing anti reflection coating of the mirror backside. For further analysis the spectra had to be baseline corrected thus reducing the accuracy of the line position and line strength determination outlined below. In order to estimate a potential error resulting from the baseline correction, the determined line positions were compared to the zero crossings of uncorrected first derivative spectra. Within the resolution of the derivate spectra, no systematic differences in the extracted line positions could be found showing that the baseline correction procedure was reliable. For fitting the observed spectra, Galatry[7] line profiles were used. A fitting routine based on the Galatry line profile algorithm given by Ouyang and Varghese[8] was implemented in MATLAB software (MathWorks, Version 7.8.0.347).

ADDITIONAL REFERENCES (EXCERPT)

[1] Perevalov, B.; Kassi, S.; Perevalov, V.; Tashkun, S.; Campargue, A. *J. Mol. Spectrosc.* **2008**, *252*, 143 – 159.

[2] Toth, R.; Brown, L.; Miller, C.; Devi, V. M.; Benner, D. *J. Quant. Spectrosc. Radiat. Transfer* **2008**, *109*, 906 – 921.

[3] Devi, V. M.; Benner, D. C.; Brown, L.; Miller, C.; Toth, R. *J. Mol. Spectrosc.* **2007**, *245*, 52 – 80.

[4] Lehmann, K. K.; Huang, H. In *Frontiers of Molecular Spectroscopy*; Laane, J., Ed.; Elsevier Books, Amsterdam, 2008; Chapter 18, pp 623–658.

[5] Romanini, D.; Lehmann, K. K. *J. Chem. Phys.* **1993**, *99*, 6287–6301.

[6] Macko, P.; Romanini, D.; Mikhailenko, S.; Naumenko, O.; Kassi, S.; Jenouvrier, A.; Tyuterev, V.; Campargue, A. *J. Mol. Spectrosc.* **2004**, *227*, 90 – 108.

[7] Galatry, L. *Phys. Rev.* **1961**, *122*, 1218–1223.

[8] Ouyang, X.; Varghese, P. L. *Appl. Opt.* **1989**, *28*, 1538–1545.

2.4 ADDITIONAL INFORMATION

2.4.1 *Frequency stabilization of the reference DFB laser*

Supposing that cavity length modulation is used to achieve resonance of laser light and cavity mode spectrum, the linewidth of the laser determines not only the coupling efficiency but also the overall spectral resolution of the technique. Early Fabry-Perot laser diodes exhibited linewidths of single laser cavity modes, $\Delta\nu_g$, on the order of few hundreds of MHz. Improvements could be achieved by extending the cavity as in an ECDL and/or by introducing additional frequency selectivity inside the diode as in DFB laser systems. Both enable narrow band single mode operation and tuning of the emission wavelength of the laser diode with line widths of less than a few MHz. In the case of external cavity diode lasers running in single mode q, the corresponding emission line width $\Delta\nu_q$ is given by the modified Schawlow-Townes equation[53]

$$\Delta\nu_q = \frac{h\nu_q g n_{SP}(\Delta\nu_g)^2}{I_0}\,\alpha_t(1-\beta^2), \tag{2.13}$$

where g denotes the gain, α_t the loss, β the spectral line width enhancement factor, and $\Delta\nu_g$ the bandwidth of the Fabry-Perot cavity of the laser diode. n_{SP} is the number of spontaneously emitted photons and I_0 the power in the corresponding mode q.
However, mostly environmental effects lead to a drift of the wavelength and blur the fundamental linewidth into an effectively broadened line. In the case of a ECDL, additional mismatches of gain profiles from laser cavity and grating can lead to mode hops during tuning. An approach to circumvent these long term broadening effects is active wavelength stabilization. This requires a suitable error signal indicating the deviation of the transmission or reflection of a frequency selective element such as an etalon, a grating, or an absorption cell. In the latter approach, the laser is stabilized to the wing of an absorption line where the slope of the signal is most pronounced. As outlined in the following, this locking scheme can be further enhanced if modulation techniques are applied.
Wavelength modulation of a monochromatic wave of a single mode laser leads to a time dependent wavelength change described by the modulation frequency Ω and the modulation depth $\Delta\nu$ according to

$$\nu(t) = \nu_0 + \Delta\nu\sin(\Omega t) \tag{2.14}$$

If the modulation depth is small, the signal obtained by a photo detector can be expanded in a Taylor series and approximated by truncation after the first expansion term yielding

$$S(t) = S_0 + S'(v_0)\times\Delta\nu\times\sin(\Omega t) \tag{2.15}$$

In case of lock-in detection the signal is demodulated by mixing this signal with the modulation frequency Ω such that

$$S(t)\times\sin(\Omega t) = S_0\times\sin(\Omega t) + S'(v_0)\times\Delta\nu\times\sin^2(\Omega t) \tag{2.16}$$

$$= \Delta\nu/2\times S'(v_0) + S_0\times\sin(\Omega t) - S'(v_0)\times\Delta\nu\times\cos(2\Omega t). \tag{2.17}$$

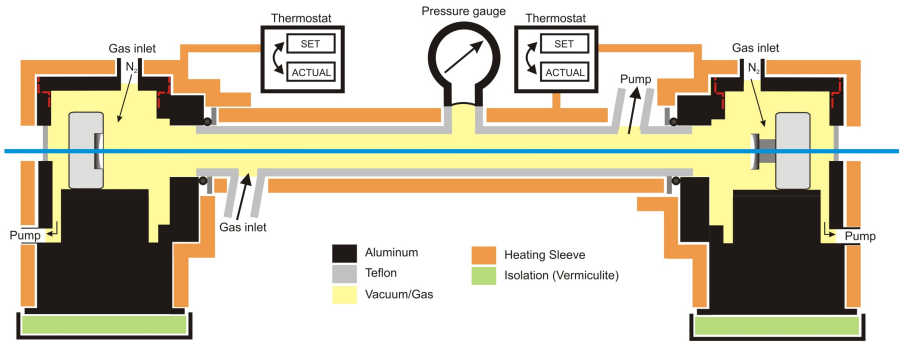

Figure 2.2: Schematic setup of the constructed detection cell and temperature stabilization system used for the cavity ringdown measurements.

Low pass filtering removes the fast time dependent components and the processed lock-in signal is given by

$$S(t) = \Delta\nu/2 \times S'(\nu_0). \tag{2.18}$$

The signal is therefore proportional to the first derivative with respect to the wavelength and the modulation depth. Thus, if an absorption cell is used and the central wavelength is scanned over an absorption line, the derivative spectrum of the corresponding line with zero crossing and maximum slope at the line center position is obtained. This signal is therefore a suitable error signal and can be used to lock the diode laser frequency to the center wavelength. It enables absolute wavelength stabilization on the order of a few hundred kHz. It is noteworthy that such a modulation leads to an effective line broadening such that the coupling efficiency of modulated light into a high finesse cavity becomes low.
The concept followed in this thesis makes use of the outlined stabilization scheme to lock a distributed feedback (DFB) laser with excellent modulation properties in the described manner. Additionally, a free-running ECDL is used as probe laser for CRDS providing the desired narrow bandwidth for efficient coupling into a high-finesse cavity. As the difference frequency measurement (outlined in more detail in the preceding publication section 2.3) enables a relative precision of $\delta\nu \approx 20$ MHz on the 1 s time scale used for averaging, the combination of frequency-locked DFB laser and the ECDL enables highest wavelength accuracy of the CRDS experiment as well.

2.4.2 *Further improvements of the spectrometer setup*

The experimental setup shown in the publication could be further improved by two innovations, which were used for the measurements presented in the following chapters:

- The CO_2 reference absorption cell has been originally used in a three-pass-configuration of the reference DFB laser for wavelength calibration. In the improved setup, it has been exchanged by a Herriott multi-pass cell (Toptica CMP-30, 73 passes). The latter enabled an extension of the effective optical path length from 1.5 m to 30 m. Consequently, the concentration in the gas cell could be decreased from 80 mbar down to 5 mbar without loss of absorption

signal. At such a low pressure, the rovibrational transition of carbon dioxide is almost purely Doppler broadened and, thus, the effects of pressure broadening on the line profile as well as the pressure shift that slightly effected the line position could be significantly minimized.

- In order to enable quantitative line strength measurements, the setup must ensure temperature stability. In early measurements it was empirically found that deviations from line strength parameters are observable at low temperatures ($T < 293\,\mathrm{K}$). Therefore, the setup was temperature stabilized to maintain a constant temperature of 320 K.
  The temperature stabilization system is sketched in Figure 2.2. Basically, the two monolithic mounts containing the highly reflective mirrors were thermally isolated from the optical table to prevent the table to act as a heat sink. Both mounts were heated by identical sleeves, whereas another sleeve was used for the connecting central section. All three sleeves were heated and temperature controlled on the internal side and were isolated towards the environment. Independent feedback loops were used to enable temperature control of each sleeve. Beforehand, temperature measurements inside the detection cell were used to derive stabilization parameters that enable a uniform temperature along the whole reactor. Overall, long term temperature stability and reproducibility was found to be better than $\Delta T = \pm 0.5\,\mathrm{K}$.

3

QUANTITATIVE SPECTROSCOPY OF N_2O ISOTOPOMERS

No effect that requires more than 10 % accuracy
in measurement is worth investigating.

— Walther Nernst (1864 - 1941)

3.1 SCOPE OF THE PROJECT

Accurate analysis techniques to distinguish the single labeled ^{15}N-isotopomers of nitrous oxide, $^{15}N^{14}N^{16}O$ and $^{14}N^{15}N^{16}O$, have been inaccessible for several years. In mass spectrometry, the fundamental problem is the identical mass of the two isotopomers, which prevents the resolution of two molecular ion peaks even with highest resolution. Although the information of the initial ^{15}N position should in principle be recoverable from the fragmentation pattern (i.e., formation of isotopic NO^+), the early study of Friedman and Bigeleisen[56] had shown that the fragmentation reaction of the two isotopomers is rather complex and accompanied by isotopic scrambling. It could be shown, that approximately 8% of the 'wrong' isotopic labeled NO^+ were formed from each of the isotopomers. Simple corrections taking this factor into account were sufficient for tracer experiments, but the error in reproducing experiments on different mass spectrometers remained high.
In 1999, Toyoda and Yoshida[57] presented a novel calibration scheme based on ammonium nitrate as suitable N_2O precursor that should enable the determination of the precise scrambling factor in a isotope ratio mass spectrometer. This procedure minimized the experimental error originating from the characteristics of the mass spectrometer and a precision better than 0.1‰ has been stated for the ratio of the two isotopomers of nitrous oxide. In the following, Kaiser *et al.*[58] presented another method for calibration based on $^{15}N_2O$ addition yielding a similar precision. Unfortunately, the application of both techniques[14,58] to determine the average site preference of tropospheric N_2O revealed a remarkable difference of approximately 30‰. A detailed analysis of this discrepancy preformed by Westley *et al.*[15] pointed out that the scrambling ratio of the two isotopomers is different and therefore assumptions used in the calibration schemes may not be valid.
Due to these difficulties in the mass spectrometric analysis, spectroscopic methods turned out to be a suitable alternative. First, Esler *et al.*[59] utilized high resolution Fourier transform infrared (FTIR) spectroscopy in combination with multi-pass cells to analyze the fundamental asymmetric stretching band ($\approx 2200\,cm^{-1}$) of the isotopomers and fitted the band structure numerically to obtain the individual isotopomer concentrations. Further improvement of the spectrometer enabled Griffith *et al.*[60] to validate the tropospheric site preference value of Yoshida and Toyoda.[14]
Alternatively, narrow band laser based methods have been elaborated. In the near infrared spectral region, sensitive WMS utilizing a multi-pass cell and line center locked diode lasers[61] around $5000\,cm^{-1}$ as well as sensitive CRDS measurements[62] in the third overtone region at $6400 - 6550\,cm^{-1}$ were applied to determine the iso-

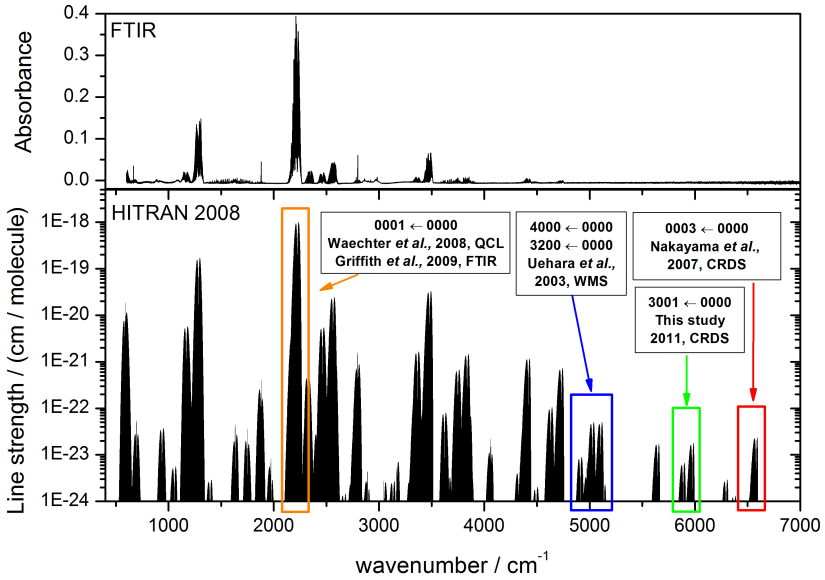

Figure 3.1: Vibrational spectrum and absorption line positions of nitrous oxide. The lower graph shows the line positions and intensities of nitrous oxide on a logarithmic scale as taken from the HITRAN database.[66] Highlighted are branches used for spectroscopic isotopomer measurements. For comparison, the upper graph shows a typical FTIR spectrum of nitrous oxide.

topomers individually. Both approaches suffered from the low line strength of the utilized absorption transitions. More recently, quantum cascade laser (QCL) became available that enabled detection schemes in the mid infrared with a comparatively simple, tunable laser source. A combination of a pulsed QCL with a multipass cell has been presented by Wächter *et al.*[63] revealing a remarkable sensitivity. A precision of 0.5‰ for the isotopomer ratio has been stated. The setup could even be improved by using a narrowband *cw*-QCL and was coupled with a preconcentration unit to detect isotopomer ratios in air.[64] This promising concept has therefore been adopted to develop field-deployable commercial CRDS and cavity enhanced absorption spectroscopy (CEAS) systems.[65]

3.2 PROJECT OBJECTIVES

As apparent from the intensities shown in Figure 3.1, shifting the detection wavelength from the near-infrared towards the mid infrared region should enable several orders of magnitude higher sensitivities. Truly, the already presented sensitivity of FTIR methods or the use of mid infrared tunable QCL systems in compact setups can only be challenged with much more sophisticated systems like CRDS, CEAS or FMS operating in the near infrared. However, beside sensitivity, another relevant aspect is the often neglected species selectivity of the technique.
As depicted by Esler *et al.*,[59] the resolution of the FTIR spectrometer is a key quantity to reveal the isotopomer structure by enabling accurate numerical fitting of the obtained spectra. On the one hand, this limits the application of FTIR spectroscopy to high end systems with long mirror displacements. On the other hand, mid infrared

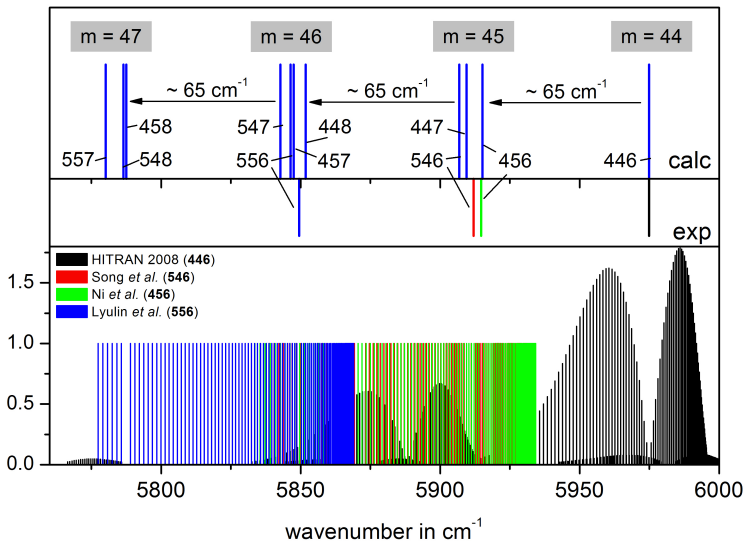

Figure 3.2: Line strength and positions of the 3001←0000 nitrous oxide isotopomer bands. The lower graph presents the recently measured line strength intensities (if available) and positions of nitrous oxide isotopologues. Band center positions are highlighted above.[67–69] The upper graph shows the approximated line center positions determined by shifting the line center of the main isotopologue with increments taken from the fundamental vibrations.

lasers such as a QCL provide the desired high resolution, but are rarely tunable over a broad spectral range. As a consequence, QCL approaches require a close spectral distance between the probed, preferably undisturbed isotopomer absorption lines. Because the line shift of the normal mode fundamental vibrations induced by isotopic substitution is small (but characteristically different for each isotopomer), the corresponding band structure is dense. In general, isotopomer lines of the same vibrational-rotational state have significantly different resonance frequencies. Therefore, isotopomer lines used in QCL experiments are generally not based on the same rotational (in some case vibrational) state. This leads to a distinct, unfavorable temperature dependence of the relative populations of the involved states. Moreover, these lines are often affected by absorption stemming from other broadened lines of the much more abundant main isotopologue.[64] Under atmospheric conditions and natural abundance of the isotopomers, inclusion of additional lines into numerical fitting has been shown to compensate for these cross sensitivities, but the general problem remained unresolved. In the light of selectivity a detection in the near infrared spectral region might be advantageous. Here, isotopomeric absorption lines of a vibrational-rotational state undergo a more pronounced isotopic shift. A disadvantage, however, is the strongly decreasing intensity of the absorption lines. Therefore, previous near infrared studies[61,62] had been focused on sensitivity and temperature issues.

In this study, this concept of a more selective isotopomer detection to determine isotopomer ratios was followed and a suitable NIR band with the desired characteristics (band intensity, temperature independence, and isotopic shift) has been chosen. Taking into account the well characterized spectral shifts of the fundamental transitions upon isotopic substitution,[70] it is possible to approximate isotopomeric shifts of the

rather weak and therefore less accurately known combination bands of nitrous oxide by neglecting the small influence of anharmonicity. Such an approximation of the band center positions is shown in the upper part of Figure 3.2 for the $3001 \leftarrow 0000$ transition of N_2O. This cold band exhibits comparatively high intensity in the near infrared mostly attributed to the contribution of the asymmetric stretching vibration. More interesting, however, the compensating effects of asymmetric and symmetric stretching vibrations yield to shifts that are almost independent of the position of isotopic substitution. Consequently, isotopomers with identical masses[1] are equally shifted by approximately 65 cm^{-1} per mass unit. The calculated shifts are more or less consistent with experimental results for the band center positions of the heavy nitrogen isotopomers as determined in the early measurements of Toth[71] and in the very recent high resolution FTIR and CRDS studies[67–69,72] shown in the lower part of Figure 3.2. The stick spectra of the two isotopomers of interest (shown in red and green colors) clearly overlap, whereas all other isotopologues, except $^{14}N^{14}N^{17}O$, are clearly separated. In the corresponding R branches around 5925 cm^{-1} the densities of the isotopomer lines increases and only very high rotational states of the main isotopomer interfere. This situation provides ideal conditions for isotopomer selective application of laser spectroscopy and therefore this spectral range has been chosen for further investigation.
In the following, high resolution mass spectrometry is used to analyze almost pure isotopomer samples and some light is thrown on the fragmentation problem. In a second step, the choice of suitable absorption lines of the two isotopomers will be further elucidated and the isotopically enriched isotopomer samples were analyzed to determine as accurate as possible absolute line intensities. These can be used for a calibration-free determination of the isotopomer ratio in later measurements. The pros and cons of this approach are discussed in the context of its application to measure the isotopomer ratio of a reference reaction.

3.3 THEORETICAL BACKGROUND

3.3.1 *Isotopomer ratio of nitrous oxide*

A convenient notation for describing isotope effects is derived from IRMS and therefore dimensionless number ratios, R, and Delta values, δ, are often used instead of concentrations.[6] These two quantities are defined by

$$R = \frac{N_{\text{heavy}}}{N_{\text{light}}} \qquad \delta X = 1000 \times \left(\frac{R - R_{\text{STD}}}{R_{\text{STD}}} \right) \tag{3.1}$$

with the definition of N_{heavy} and N_{light} as heavy and light isotope number. Generally, the ratio of a standard material, R_{STD}, is used to determine the Delta values.
In the case of nitrous oxide, 12 stable isotopologues and isotopomers ($^{15}N/^{14}N$, $^{18}O/^{17}O/^{16}O$) exist. Focusing on the most abundant oxygen nucleus, ^{15}N-isotopic substitution is possible in two different positions, central (superscript 1) and terminal

1 Corresponding isotopologues are abbreviated with the second digit of the atomic masses.

(superscript 2). Using Equation 3.1, site specific isotopic ratios can be defined as follows:

$$R^1_{^{15}N} = \frac{|456|}{|446|} \qquad \delta^{15}N^1 = 1000 \times \left(\frac{R^1_{^{15}N} - R_{\mathrm{STD}}}{R_{\mathrm{STD}}} \right) \tag{3.2}$$

$$R^2_{^{15}N} = \frac{|546|}{|446|} \qquad \delta^{15}N^2 = 1000 \times \left(\frac{R^2_{^{15}N} - R_{\mathrm{STD}}}{R_{\mathrm{STD}}} \right) \tag{3.3}$$

Based on the two Delta values, Toyoda and Yoshida[14,57] defined a novel parameter, the site preference, SP, to represent a relative enrichment of one of the two isotopomers:

$$SP = \delta^{15}N^1 - \delta^{15}N^2 \tag{3.4}$$

More generally, the isotopomer ratio, R^{SP}, and the related delta value, δ^{SP}, are the kinetically and thermodynamically more consistent parameters and are defined as[60]

$$R^{SP} = \frac{|456|}{|546|} = \frac{R^1_{^{15}N}}{R^2_{^{15}N}} \qquad \delta^{SP} = \left(R^{SP} - 1 \right) \times 1000. \tag{3.5}$$

The definition of δ^{SP} implicitly assumes that the standard material has an isotopomer ratio equal to 1.
Using the approximation $\delta^{15}N^2 \ll 1000$ follows:

$$\delta^{SP} = \left(\frac{1000 + \delta^{15}N^1}{1000 + \delta^{15}N^2} - 1 \right) \times 1000 = \left(\frac{\delta^{15}N^1 - \delta^{15}N^2}{1000 + \delta^{15}N^2} \right) \times 1000 \approx SP. \tag{3.6}$$

Thus, δ^{SP} equals SP in most cases dealing with nitrous oxide samples with natural isotopic abundance.
Spectroscopically, the isotopomer ratio R^{SP} is accessible from absolute concentration measurements, but for these concentration measurements accurate line strength parameters S are required according to

$$R^{SP} = \frac{[456]}{[546]} = \frac{\int_{456} \alpha(\tilde{\nu})\, d\tilde{\nu} \times S(546)}{\int_{546} \alpha(\tilde{\nu})\, d\tilde{\nu} \times S(456)}. \tag{3.7}$$

3.3.2 *Quantitative absorption measurements*

Basically, quantitative absorption can be explained in terms of the simple two-level-model of Einstein's coefficients of absorption ($B_{\eta'',\eta'}$) and emission ($A_{\eta',\eta''}$,$B_{\eta',\eta''}$) as shown in Figure 3.3.[73] An incident electromagnetic wave with a frequency resonant to the energetic difference of the transition will lead to a population increase of the higher level following a transition probability $B_{\eta'',\eta'}$. The reverse process of emission can either be spontaneous ($A_{\eta',\eta''}$) or induced ($B_{\eta',\eta''}$). It can be shown that the two coefficients, $B_{\eta',\eta''}$ and $B_{\eta'',\eta'}$, are identical and can be related to the absolute square of the transition moment, $|R_{\eta'',\eta'}|^2$, according to

$$B_{\eta'',\eta'} = B_{\eta',\eta''} = \frac{2\pi^2}{3\epsilon_0 h^2} |R_{\eta'',\eta'}|^2 = \frac{2\pi^2}{3\epsilon_0 h^2} \sum_{x,y,z} R^2_{\eta'',\eta',i} \tag{3.8}$$

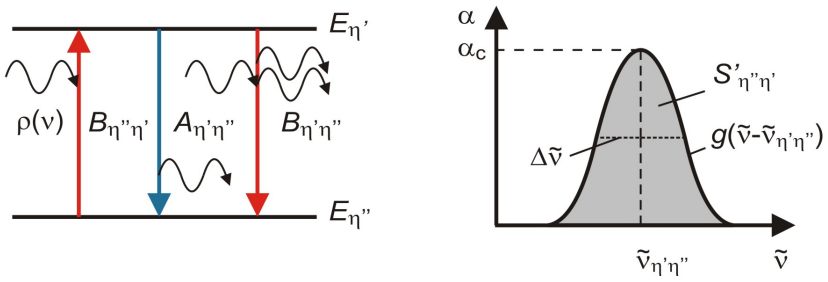

Figure 3.3: Left: Schematic plot of Einstein parameters. Right: Definition of line strength and related parameters of an absorption line.

where $R_{\eta'',\eta',x}$, $R_{\eta'',\eta',y}$, and $R_{\eta'',\eta',z}$ are the transition moments in x, y, and z direction, respectively.
By neglecting spontaneous emission (convenient for near infrared transitions), the net absorption intensity, $S_{\eta'',\eta'}$, depends on the population of the two states, $n_{\eta'}$ and $n_{\eta''}$ and is given by

$$S_{\eta'',\eta'} = h\tilde{\nu}_{\eta'',\eta'} \frac{n_{\eta''}}{N} \left(1 - \frac{g_{\eta''} n_{\eta'}}{g_{\eta'} n_{\eta''}}\right) B_{\eta'',\eta'} = \frac{2\pi^2}{3\epsilon_0 h^2} \tilde{\nu}_{\eta'',\eta'} \frac{n_{\eta''}}{N} \left(1 - \frac{g_{\eta''} n_{\eta'}}{g_{\eta'} n_{\eta''}}\right) |R_{\eta'',\eta'}|^2. \tag{3.9}$$

For a more general picture the degeneracies of the two states, $g_{\eta''}$ and $g_{\eta'}$, are included, but assumed to be equal in the following. If the system is in thermal equilibrium, a Boltzmann distribution can be assumed to replace the expressions for the population by introducing the partition function $Q(T)$ and Equation 3.9 can be rewritten as

$$S_{\eta'',\eta'} = \frac{2\pi^2}{3\epsilon_0 h^2} \tilde{\nu}_{\eta'',\eta'} \frac{g_{\eta''} \exp\left(-E_{\eta''}/kT\right)}{Q(T)} \left(1 - \exp\left(-\tilde{\nu}_{\eta'',\eta'} c_2/T\right)\right) |R_{\eta'',\eta'}|^2 \tag{3.10}$$

where c_2 denotes the second radiation constant. In the case of a gas phase rotational-vibrational transition, $|R_{\eta'',\eta'}|^2$ is proportional to the derivative of the dipole moment with respect to the normal coordinate and is folded with the Hönl-London and the Herman-Wallis factor, to account for the intensity distribution of the rotational branches and the rotational-vibrational coupling, respectively.[74] This net absorption intensity of a vibrational-rotational transition corresponds to Beer's absorption coefficient, $\alpha(\tilde{\nu})$ (as defined in Equation 2.1), integrated over the wavenumber range of the broadened absorption line. Supposing a known line shape function $g(\tilde{\nu} - \tilde{\nu}_0)$ it can be further related to the absorption coefficient at the line center, α_c, and the concentration independent absorption cross section, $\sigma(\tilde{\nu})$, by[75]

$$S_{\eta'',\eta'} = \frac{kT}{p} \int_{\tilde{\nu}_1}^{\tilde{\nu}_2} \alpha(\tilde{\nu})\, d\tilde{\nu} = \frac{kT}{p} \int_{\tilde{\nu}_1}^{\tilde{\nu}_2} \alpha_c\, g(\tilde{\nu} - \tilde{\nu}_0)\, d\tilde{\nu} = \int_{\tilde{\nu}_1}^{\tilde{\nu}_2} \sigma(\tilde{\nu})\, d\tilde{\nu} \tag{3.11}$$

The line intensity of an absorption line is therefore directly proportional to the number density of the absorbing species and, in contrast to the narrow-band absorption coefficient, independent of the underlying broadening mechanism discussed in the following section.

3.3.3 *Line broadening and line shape models*

The fundamental limit of broadening of an absorption line follows from spontaneous emission of the excited state. This natural or lifetime broadening is therefore directly correlated with Einstein's spontaneous emission coefficient, $A_{\eta',\eta''}$, according to

$$\Delta\nu_{\text{nat}} \geq A_{\eta',\eta''} = 8\pi hc \times \tilde{\nu}^3 \times B_{\eta',\eta''}. \tag{3.12}$$

Consequently, natural line broadening becomes more significant at higher frequencies, but compared to other broadening mechanisms it is often negligible. In the near infrared spectral region $\Delta\nu_{\text{nat}}$ is typically in the kHz range.
Another effect that can be directly deduced form the simple Einstein model is saturation or power broadening. In the case of strong electrical fields and high transition dipole moment, saturation as consequence of decreasing population difference of the energy levels sets in and lowers the central absorption leading to an effective broadening.
A significant contribution to the line shape originates from the thermal motion of the molecules, the Doppler broadening. Movement of particles in the same or reversed direction of an interacting wave results in an velocity dependent detuning of the absorption frequency. Based on Maxwell's distribution, the inhomogeneously broadened line shape is a Gaussian distribution with a full width at half maximum (FWHM) of

$$\Delta\tilde{\nu}_{\text{D}} = 2\gamma_{\text{D}} = \left(\frac{2kT\ln 2}{mc^2}\right)^{1/2} \tilde{\nu}_c. \tag{3.13}$$

Finally, the line shape is affected by collisions of the molecules with the environment (walls or buffer gases), called pressure broadening. The consequence is a perturbation during the absorption or emission process causing line broadening and also leads to a shift ($\delta = \delta^0 \times p$) of the line center . The homogeneously broadened line shape function results in a Lorentzian line shape and its full width at half maximum is given by

$$\Delta\tilde{\nu}_{\text{P}} = 2\gamma_L = 2\gamma_L^0 p \tag{3.14}$$

where γ_L^0 is the gas specific pressure broadening coefficient.
The simultaneous effects of different broadening mechanisms, in particular thermal motion and phase changing collisions, have been treated in quite different manners. One of the most commonly used model is the Voigt model,[76] which is based on a convolution of the Lorentzian and Gaussian distribution, such that each spectral component of the Lorentzian broadened line is itself Doppler broadened. The resulting line profile function cannot be solved analytically. It requires numerical evaluation of the Voigt function, which can be written as the Fourier transform of a time correlation function depending on τ as

$$K(x',y) = \frac{1}{\sqrt{\pi}} \int_0^{+\infty} \cos x'\tau \exp\left(-y\tau - \tau^2/4\right) \mathrm{d}\tau \tag{3.15}$$

with the line profile parameters, x' and y, given by

$$x' = (\tilde{\nu} - \tilde{\nu}_0 - \delta^0\ p)\ \frac{\sqrt{\ln 2}}{\gamma_D} \ \wedge\ y = \gamma_L^0\ p\ \frac{\sqrt{\ln 2}}{\gamma_D}. \tag{3.16}$$

Early computer implementations yielded reliable fitting routines such that the Voigt profile became easily accessible and - due to a quite accurate representation of the experimentally obtained line shapes - is the basis for several databases on absorption line parameters.
However, in 1952 Dicke[77] pointed out that an increasing gas density should affect the velocity distribution underlying the Doppler broadening leading to an effective line narrowing. The general concept of this later called 'Dicke narrowing' was adapted by Galatry[78] who considered simultaneous but uncorrelated density based collision effects on Doppler broadening and phase changing collisions resulting in pressure broadening. By assuming that several collisions are necessary to affect the velocity distribution, the model is generally considered as a soft collision model. After a new parametrization and normalization on Doppler width performed by Herbert,[79] the generalized Galatry function is given by

$$G(x', y, z) = \frac{1}{\sqrt{\pi}} \int_0^{+\infty} \exp\left(-ix'\tau - y\tau + \frac{1}{2z^2}(1 - z\tau - \exp(-z\tau))\right) \mathrm{d}\tau. \quad (3.17)$$

Here, the profile parameters x' and y are identical to 3.16 and z is given by

$$z = \beta^0_{\text{Soft}}\ p\ \frac{\sqrt{\ln 2}}{\gamma_D}. \quad (3.18)$$

Here, β^0_{Soft} is the soft collision narrowing parameter (or dynamical friction coefficient), which is related to the 'optical' diffusion coefficient D of the absorber in the gas matrix according to

$$\beta^0_{\text{Soft}} = \frac{k_B T}{2\pi c m D}. \quad (3.19)$$

Noteworthy is that, in the case of pressure broadening surpassing the narrowing effect, the experimental β^0_{Soft} value is generally overestimated. Thus, the 'optical' diffusion coefficient does no longer reflects the real diffusion. In the limiting case of negligible line narrowing, the Galatry profile corresponds to the Voigt line shape model: For $z \to 0$ the third term of the exponential in Equation 3.17 converges in $-\tau^2/4$, thus equivalent to Equation 3.15. An efficent FFT based algorithm to numerically simulate the Galatry line shapes has been presented by Ouyang and Varghese.[80] It has been implemented in MATLAB (see appendix for the source code) and was used throughout this thesis.
An alternative model including line narrowing effects has been suggested by Rautian and Sobel'man.[81] It is based on the assumption of a velocity change for each collision with a buffer gas molecule, it is often termed 'hard' collision model. Similar to the 'soft' Galatry model, the corresponding line narrowing parameter underestimates diffusion, but the 'hard' model turned out to yield more reliable and constant narrowing parameters in the case of heavy buffer gases. Further improvement of the line shape characteristics can be achieved by using speed-dependent models that take into account the specific collisional broadening with respect to the speed of the absorber. These effects become more significant, in the case of pressure broadening exceeding the Doppler width and/or under strong collision conditions.

3.4 RESULTS AND DISCUSSION

Aiming to determine the isotopomer ratio, one needs to know accurate absolute line strength parameters for the two nitrous oxide isotopomers. In the following, the mass spectrometric and spectroscopic characterization of pure isotopomer samples and the choice of appropriate absorption lines is presented. Determined line strengths and line shape parameters of the selected absorption lines are analyzed regarding their consistency with previous measurements. Finally, the technique is applied to determine absolute isotopomer ratios of isotopically enriched nitrous oxide samples.

3.4.1 *FT-ICR-MS characterization of enriched N_2O isotopologues*

The determination of absolute line strength parameters requires chemically and isotopically pure samples for calibration purposes. To this ends, the used isotopomerically enriched samples were characterized by mass spectrometry. Fourier transform-ion cyclotron resonance (FT-ICR) mass spectrometry is a high resolution technique providing mass resolutions up to $m/\Delta m = 10^4$ - 10^6 or better and therefore offers the required sufficient resolution to distinguish single isotopologues.
Full range FT-ICR mass spectra of the two pure isotopomer standards, named IS-456 and IS-546, are shown in Figure 3.4a and Figure 3.4b. As expected, the two mass spectra are almost identical at the molecular ion peak region, but differ in the corresponding fragmentation pattern as discussed below. The rather intense peaks at m/z=28 as well as at m/z=32 in Figure 3.4a stem from an air leak of the gas inlet system of the mass spectrometer. Apart from this, no further impurities could be identified in the samples thus reflecting their high chemical purity.
The corresponding molecular ion peaks are shown in Figure 3.4c and Figure 3.4d. Due to the high resolution, the possible N_2O isotopologues except for the isotopomers could be clearly identified by their exact mass[2]. In a series of measurements almost constant peak height ratios were found. The corresponding isotopologue ratios are listed in Table 3.1. This isotopic composition is basically consistent with IRMS analysis of other research groups using pure isotopomer samples from the same supplier.[15,58] Based on this isotopic analysis above, it can be concluded that the two samples are isotopically pure to at least 98%. More detailed information on the isotopomeric composition can be derived from additional spectroscopic measure-

2 The labeled carbon dioxide peak scales with the air peaks in stoichiometric quantity.

Table 3.1: Isotopic characterization of the enriched pure isotopomer gas standards (IS-456 and IS-546) utilizing high resolution mass spectrometry (FT-ICR-MS). The superscripts, * and $^+$, indicate assignment of the corresponding mass based on supplemental NIR spectra (see Figure 3.6). Peak heights were normalized to add up to 100.

Mass	44	45	46			47	
Assigned	446	$456^*/546^+/447$	556	457/547	448	557	458/548
IS-456	0.51(2)	$98.58(11)^*$	0.29(4)	0	0.45(5)	0	0.16(2)
IS-546	0.90(6)	$98.04(8)^+$	0.74(7)	0	0.14(4)	0	0.17(7)

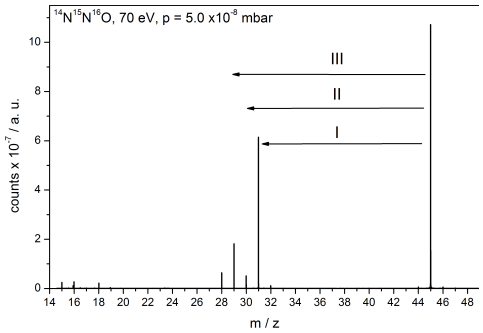

(a) Full FT-ICR mass spectrum of IS-456.

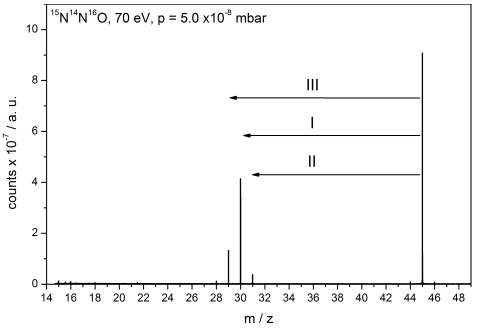

(b) Full FT-ICR mass spectrum of IS-546.

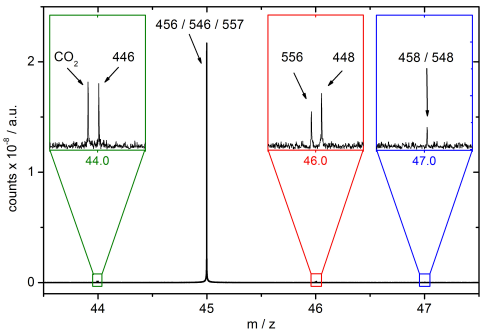

(c) Molecular ion region of N_2O in IS-456.

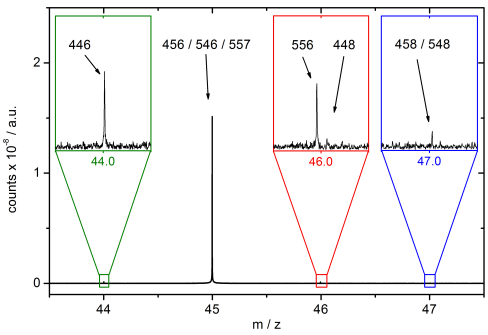

(d) Molecular ion region of N_2O in IS-546.

Figure 3.4: Isotopologue characterization of two isotopomer standards (IS) utilizing FT-ICR-MS. The roman numbers in (a) and (b) indicate fragment formation assigned to different fragmentation pathways (see text).

ments and from the observed fragmentation pattern.

The underlying fragmentation pathways (neglecting the oxygen isotopes) can be summarized as follows:

$$\begin{array}{ccc} {}^{14}N^{15}NO^+ & \xrightarrow{(I)} & {}^{15}NO^+(m/z=31) + {}^{14}N \\ {\scriptstyle (II)}\searrow & & \nearrow{\scriptstyle (II)} \\ & [NON]^+ & \\ {\scriptstyle (II)}\nearrow & & \searrow{\scriptstyle (II)} \\ {}^{15}N^{14}NO^+ & \xrightarrow{(I)} & {}^{14}NO^+(m/z=30) + {}^{15}N \end{array} \tag{3.20}$$

$$^{14}N^{15}NO^+ / {}^{15}N^{14}NO^+ \xrightarrow{(III)} {}^{15}N^{14}N^+(m/z=29) + O \tag{3.21}$$

Here, two quite different processes have been suggested to lead to NO^+ fragment formation in the fragmentation process.[56] On the one hand, it is quite evident that simple N-N bond cleavage (I) will lead to a NO^+ fragment containing the central nitrogen such that the two isotopomers should yield either $^{14}NO^+$ or $^{15}NO^+$. In contrast, N-O bond cleavage (III) yields the same fragment $^{15}N^{14}N^+$ for both isotopomers. On the other hand, justified by the experimental observations of a considerably high ratio of the 'wrong' fragment, a more complex reaction mechanism (II) is considered to occur by sequential decomposition of an so far unidentified but most likely cyclic intermediate $[NON]^+$.

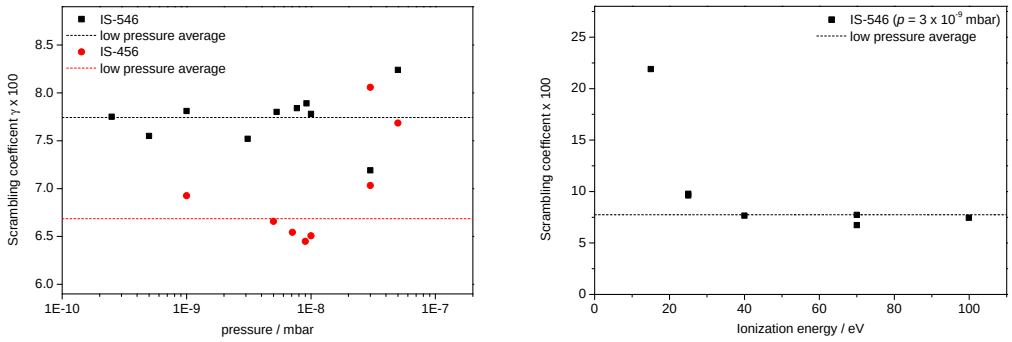

(a) Scrambling coefficient vs. sample pressure.

(b) Scrambling coefficient vs. EI potential.

Figure 3.5: Effects on isotope scrambling of nitrous oxide isotopomers during fragmentation.

The ion scrambling due to simultaneous occurrence of (I) and (II) is clearly observable in both spectra, Figure 3.4a and Figure 3.4b. In order to take this effect into account for site selective isotope measurements, Toyoda and Yoshida[57] determined based on an enriched $^{15}N^{14}N^{16}O$ sample a quite constant scrambling coefficient $\gamma \approx 8.1\%$ corresponding to the fraction of the 'wrong' NO^+ isotope relative to the overall NO^+ yield. Similar scrambling coefficients have been found in this work. With respect to isotopomeric purity of the used samples, these scrambling coefficients are consistent with a sole abundance of one of the isotopomers in each sample.
Due to the general uncertainties of mass spectrometric site preference determinations arising from this ion scrambling, a few additional experiments concerning these scrambling parameters have been reported in the literature. Westley *et al.*[15] showed that the exact ratio of the scrambling coefficients varies with experimental conditions and, moreover, is different for each isotopologue. In particular, the scrambling coefficient of $^{15}N^{14}N^{16}O$ was found to be higher than that of $^{14}N^{15}N^{16}O$. In contrast, Frame and Casciotti[82] found consistent calibration values for their mass spectrometer by assuming the opposite to be true.
Figure 3.5a summarizes the extracted scrambling coefficients for a series of measurements at different pressures as obtained in this work. At low pressures, rather constant but different values of 0.077 and 0.067 for IS-546 and IS-456 have been found, respectively. It may be speculated that the less consistent values at pressures higher than 1×10^{-8} mbar, are due to interfering bimolecular reactions within the ICR cell. However, isolation of the NO^+ fragments within the ICR cell yielded no corresponding products.
Figure 3.5b illustrates the outcome of an experiment with variable ionization energy. Similar to Toyoda and Yoshida,[57] a quite constant low pressure scrambling coefficient was found at high ionization energies. Slightly above the ionization potential, however, significantly higher scrambling ratios were observed, possibly due to a slower fragment formation via a predissociation pathway in contrast to direct dissociation pathways available at higher ionization energies.[83]

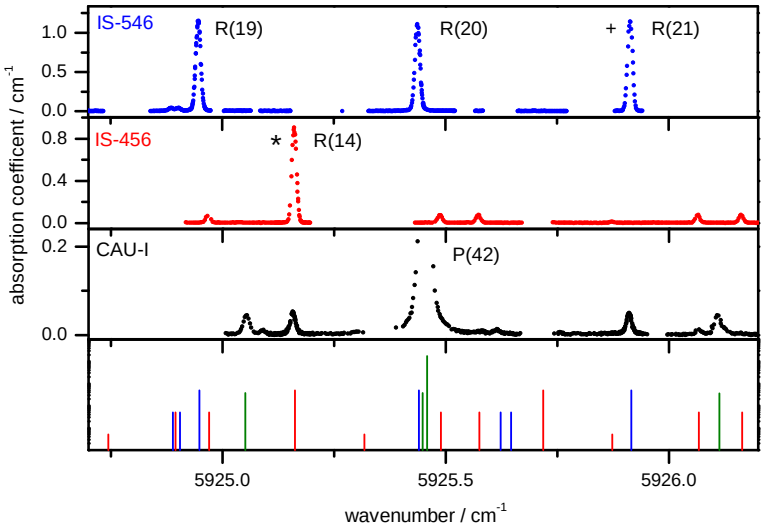

Figure 3.6: Cavity ringdown spectra of the two isotopomer samples (IS-456 and IS-546) and pure nitrous oxide with natural isotopic abundance (CAU-I) in comparison with line positions taken from the HITRAN database and FTIR measurements.[66–68] As no accurate line strength data are available, the intensities of these lines are estimated based on the type of transition and the natural abundance of the underlying isotopologue (logarithmic scale).

3.4.2 *Selection and line strengths of isotopomer absorption lines*

An independent verification of the isotopomer structure can be obtained from near infrared (NIR) cavity ringdown spectra of nitrous oxide as shown in Figure 3.6. Despite the compensating effect of the spectral positions of different vibrations as discussed for Figure 3.2, an isotopic shift of the isotopomer absorption lines can be clearly observed in the spectra. In agreement with the mass spectrometric result, direct comparison of the spectra of the two isotopomer standards, IS-456 and IS-546, reveals that only one isotopomer is present in each sample. Furthermore, the line positions in the enriched samples agree well with a pure nitrous oxide samples with natural abundance and recent high resolution FTIR measurements of nitrous oxide isotopomers reported in the literature.[66–68]

ABSORPTION LINE SELECTION In a first step, in order to enable isotopomer selective detection, it was necessary to identify isotopomeric absorption lines that (*i*) allow for a perturbation free detection and (*ii*) provide a balanced detection of the two isotopomers with respect to line intensity and temperature variation. As illustrated in Figure 3.6, difficulties may arise from several additional absorption lines attributable to hot transitions or weak combination bands. Nevertheless, it was possible to identify two absorption lines that offered comparable line intensities, showed no apparent distortion of the line profile and, according to the band structure of known transitions, revealed no interfering features. For $^{14}N^{15}N^{16}O$ the R(14) line at $\tilde{\nu} = 5925.1572\,\mathrm{cm}^{-1}$ and for $^{15}N^{14}N^{16}O$ the R(21) line at $\tilde{\nu} = 5925.9102\,\mathrm{cm}^{-1}$, both corresponding to the 3001←0000 vibrational transition, have been chosen. A major drawback of this line selection is the different rotational state, which leads to slightly

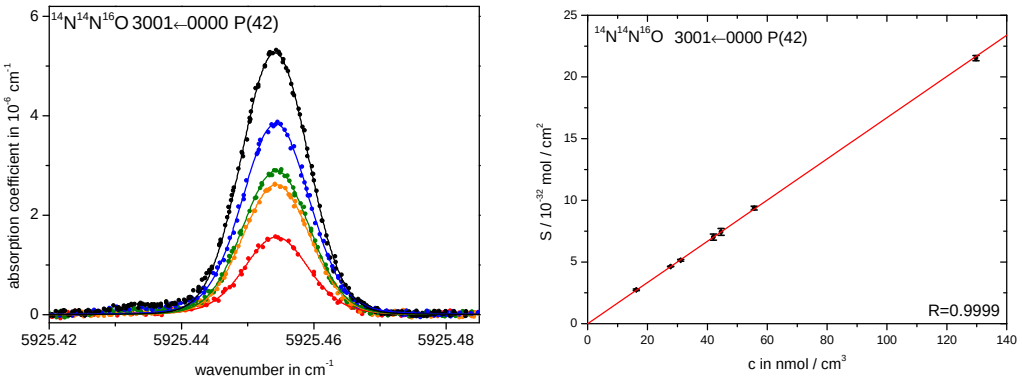

Figure 3.7: Profile and fitted line strength of the main N_2O isotopologue.

different line strengths and, more important, to a different temperature dependence of the population of the underlying states. Thus, temperature stabilization of the cell during the measurement was crucial.

LINE STRENGTH MEASUREMENTS In order to check the suitability of the setup for quantitative measurements, a known absorption line (3001 ← 0000 P(42)) of the main isotopologue of nitrous oxide has been analyzed first. Figure 3.7 shows several line strength measurements at different sample pressures of pure nitrous oxide (CAU-1). Despite an interfering line from a different isotopologue at the left edge, this line could be accurately reproduced with Galatry profile functions in the pressure range $2\,\text{mbar} < p < 5\,\text{mbar}$. The corresponding integrated line strength, which has been corrected for natural isotopic abundance as certified by IRMS, is plotted versus concentration in the second graph. The error bars correspond to the standard deviation of typically 4 measurements. With a regression coefficient of $R = 0.999$ excellent linearity has been observed. The averaged line strength as determined from the slope and corrected to a temperature of $T = 296\,\text{K}$ as described in section 2.3 is given in Table 3.2. The comparison with the corresponding HITRAN value[66] reveals quantitative agreement within error limits. The uncertainty limit of the presented measurement, which is based on the statistically error, is even lower than reported in HITRAN. This underlines the accuracy of the technique and its suitability for line strength measurements.
Similar measurements for the chosen isotopomer lines using the enriched samples IS-456 and IS-546 are shown in Figure 3.8. Here, no interference has been observed and both lines could again be accurately fitted using Galatry functions. The plots of line strength versus concentration again shows high linearity. The observed y-axis offset can be attributed to a slight zero level shift of the pressure sensor used throughout all measurements.
It should be noted that at higher pressures (concentrations $\approx 120\,\text{nmol/cm}^3$), although no changes in the line shapes were discernible, non-linearities in form of a decreasing line strength have been observed. These data have been excluded from the fit and are not shown in Figure 3.8b. At such high concentrations, the corresponding ringdown time at the line center dropped from $\tau_0 = 8\,\mu\text{s}$ to $\tau = 500\,\text{ns}$ and the transmitted intensity decreased significantly. Consequently, it was necessary to increase detector amplifier settings resulting in a lower detection bandwidth and an

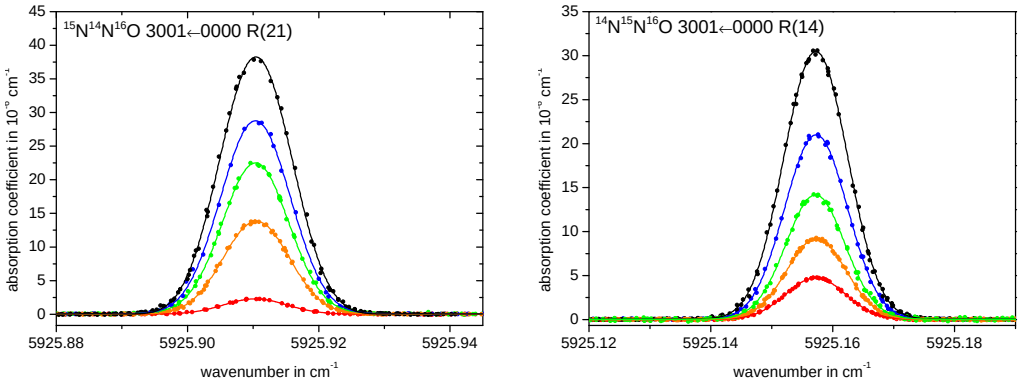

(a) Fitted line profiles of $^{15}N^{14}N^{16}O$ and $^{14}N^{15}N^{16}O$.

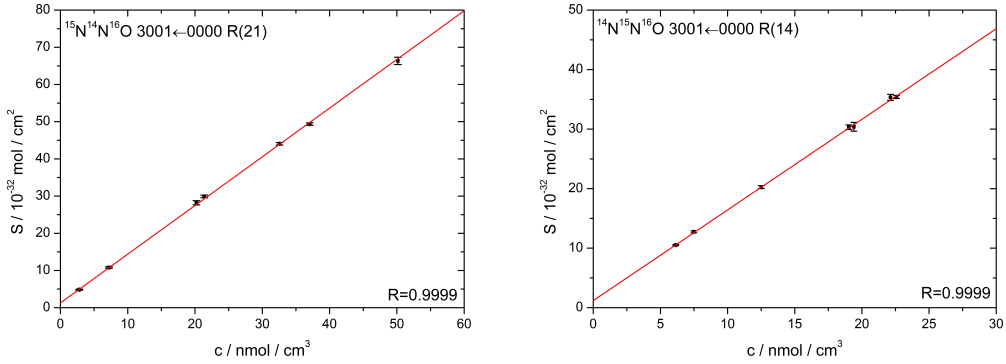

(b) Integrated line strength (vs. concentration) of $^{15}N^{14}N^{16}O$ and $^{14}N^{15}N^{16}O$.

Figure 3.8: Fitted line strength parameters of the two N_2O isotopomers.

overall less accurate ringdown time measurement. Thus, the CRDS technique itself sets an effective upper limit for reasonable sample concentrations.

LINE BROADENING AND OPTIMUM DETECTION CONDITIONS Next to providing accurate line strength data, the line shape fitting procedure also yields reliable line shape parameters. For example, measurements of natural N_2O (CAU-1) at higher pressures as shown in Figure 3.9 yielded the corresponding Galatry line shape parameters summarized together with the line strength parameters in Table 3.2. From experiments with Ar added to the sample gas, it was evident that the pressure broadening parameters of the chosen absorption lines revealed a pronounced effect of the corresponding buffer gas composition. It is noteworthy in this context that Galatry pressure broadening parameters differ from pressure broadening parameters obtained by assuming a Voigt model. The latter neglects line narrowing. The derived (in these experiments only slightly buffer gas dependent) line narrowing parameter $\beta^0_{\text{soft}} \approx 0.044\,\text{cm}^{-1}\,\text{atm}^{-1}$ is basically consistent with typical values found in the literature, e.g., Daumont *et al.*[84] performed FTIR measurements of $^{14}N_2^{16}O$ and derived an experimental narrowing parameter ($\beta^0_{\text{hard},N_2O} = 0.0342(8)\,\text{cm}^{-1}\,\text{atm}^{-1}$) using a hard collision model. They also reported a similar theoretical value ($\beta^0_{\text{diff}} = 0.0374\,\text{cm}^{-1}\,\text{atm}^{-1}$) derived from the diffusion coefficient. Due to the Galatry model assumptions the found β^0_{soft} values generally

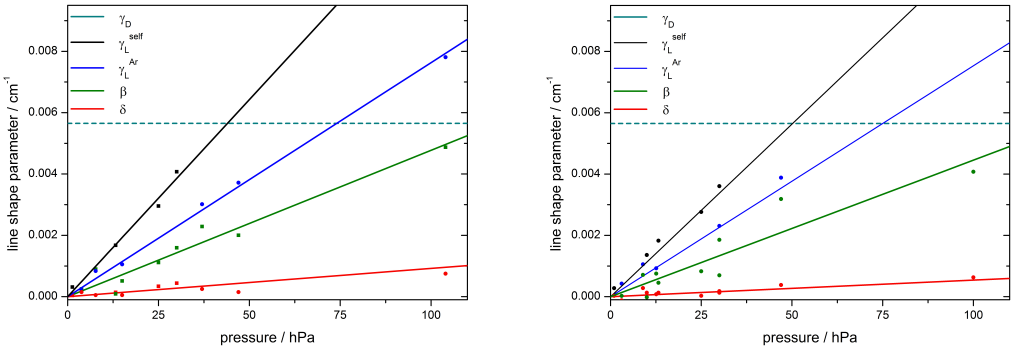

Figure 3.9: Fitted line shape parameters (vs. pressure) of $^{15}N^{14}N^{16}O$ and $^{14}N^{15}N^{16}O$.

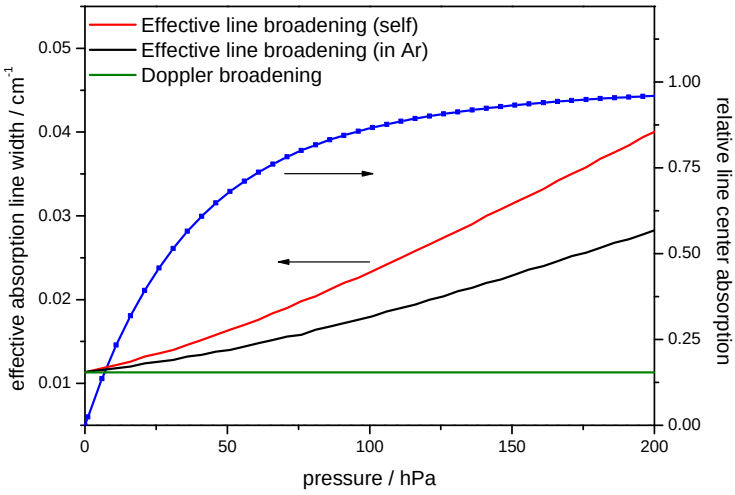

Figure 3.10: Calculated line center absorption and effective line broadening based on determined Galatry parameters versus N_2O pressure for the R(14) line of $^{14}N^{15}N^{16}O$.

Table 3.2: Line strength and line shape parameters of selected isotopologue absorption lines.

Isotopologue	$^{14}N^{14}N^{16}O$	$^{15}N^{14}N^{16}O$	$^{14}N^{15}N^{16}O$
Vibrational Assignment	3001←0000	3001←0000	3001←0000
Rotational Assignment	P(42)e	R(21)e	R(14)e
$\tilde{\nu}_0$ / cm^{-1}	5925.4591(6)	5925.9102(6)	5925.1572(6)
S^{296K} / (10^{-23} cm molecule^{-1})	0.1676(18)	1.3165(80)	1.515(13)
S(Ref)[1] / (10^{-23} cm molecule^{-1})	0.1697(33)	-	-
γ^0_{self} / (cm^{-1} atm^{-1})	-	0.1285(51)	0.1126(21)
γ^0_{Ar} / (cm^{-1} atm^{-1})	-	0.0763(14)	0.0753(13)
β^0_{soft} / (10^{-3} cm^{-1} atm^{-1})	-	47.5(27)	44.5(51)

[1] from HITRAN database[66]

exceed those derived from diffusion coefficients.[85]
Using the determined parameters it is possible to estimate optimal achievable sensitivity, selectivity and suitable measurement conditions. As shown in Figure 3.10, pressure self-broadening leads to a strong increase of the effective line width such that line center absorption reaches saturation at high pressures. For example, at 100 mbar 90% of the maximum line center intensity is reached. At the same time, broadening decreases selectivity because the wings of previously separated lines start to overlap. Moreover, an unfavorable, larger scan range is necessary. Nevertheless, for analysis for N_2O samples with natural abundance of ^{15}N, such high pressures might be necessary. Note that, even at a pressure of 80 mbar the $^{15}N^{14}N^{16}O$ isotopomer concentration is on the order of merely 10 nmol/cm^3. Compared to the enriched isotopomer concentrations used for line strength determination as shown in Figure 3.8b, this is rather low. Consequently, as the precision of the site preference determination relies on precise integral determination, the sensitivity of the detection method is crucial. For example, considering the ringdown time achieved with the mirrors used in this setup, $\tau_0 \approx 20\,\mu s$, and assuming a ringdown time precision of $\Delta\tau/\tau_0 \approx 0.3\%$, a minimum peak absorption of $5 \times 10^{-9}\,cm^{-1}$ can be detected. For comparison, the peak absorptions of the nitrous oxide lines for a concentration of 10 nmol/cm^3 at a pressure of 80 mbar are on the order of 2×10^{-6}, thus 200 times higher than the detection limit. Although sufficient from the perspective of simple gas detection, a factor of 200 under already optimized conditions is not quite sufficent to perform isotopomer ratio measurements with the desired precision on a percent or even better scale. Further experimental improvements are clearly needed to achieve the desired precision for analyzing N_2O samples with an isotopic composition at natural abundance.

3.4.3 *Test and accuracy of site preference determination*

Isotopically enriched samples offer an opportunity to measure at lower pressures circumventing the effect of pressure broadening discussed above. Here, ^{15}N-enriched samples were used (a) to check the consistency of the obtained parameters, (b) to prove the feasibility of spectroscopic measurement of the absolute isotopomer ratios, and (c) to verify the observation of a positive site preference in non-enzymatic N_2O formation.
For this purpose, the nitrite reduction experiments performed by Toyoda *et al.*[19] for site preference determination of a chemical reaction have been repeated with varying parameters. These experiments were based on nitrite reduction utilizing trimethylaminoborane under acidic conditions in aqueous solution and sequential isolation and analysis of the product gases. This reaction has been described in detail by Bell and Kelly[86] to follow the net reaction

$$2\,HNO_2 + (CH_3)_3N \cdot BH_3 \xrightarrow{+H^+} (CH_3)_3N + B(OH)_3 + H_2 + N_2O \qquad (3.22)$$

The suggested underlying mechanism is considered to include the HNO dimerization reaction according to Equation 1.9, which is responsible for the N_2O product formation. The corresponding isotopologue composition of the nitrous oxide product is thus directly correlated with the initial isotopic composition of the used nitrite.

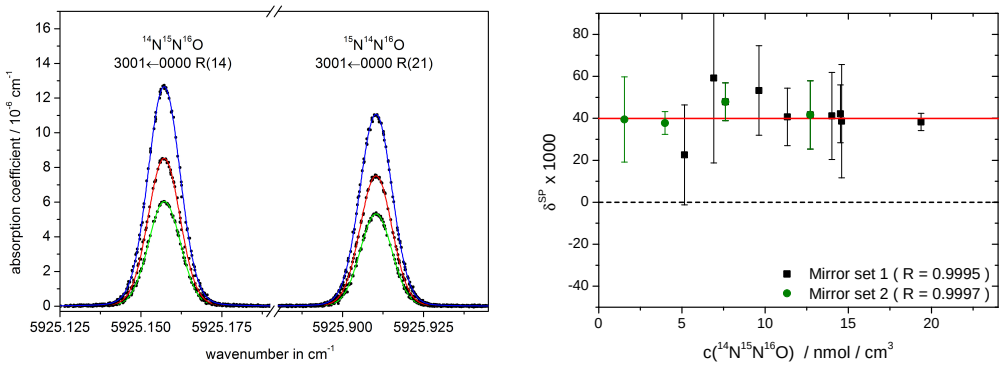

(a) Typical CRD spectra of N_2O samples.

(b) δ^{SP} versus isotopomer concentration.

Figure 3.11: Isotopomer analysis of nitrous oxide samples from nitrite reduction experiments with varying isotopic substrate composition.

This could be verified by FTIR measurements of the product gases revealing a proportional increase of the isotopic bands in the spectral region of the asymmetric and symmetric stretching vibration. In addition to this, within the accuracy of these measurements, approximately equal amounts of the two single ^{15}N-labeled isotopomers were found under all experimental conditions.
In the experiments shown in Figure 3.11, varying fractions of ^{15}N-labeled nitrite were used for nitrite reduction performed at constant temperature. The cavity ringdown spectra of the isolated product gases are shown in Figure 3.11a and confirmed the formation of the two isotopomers. All spectra were basically Doppler resolved without significant contributions of pressure broadening effects. These spectra were analyzed and fitted according to Equation 3.7 to determine the ^{15}N-site preference. The results of four different synthesis with various isotopomer concentrations are shown in Figure 3.11b. For the mirror set 1 (less reflective, less sensitive), the scatter of the determined site preference values decreases with increasing isotopomer concentration. The same average value was obtained at overall lower concentrations with a mirror set with higher reflectivity (set 2). These findings are consistent with the above statement regarding the sensitivity limit. However, the constant ^{15}N site preference value at higher pressures underlines the feasibility of spectroscopic site preference measurements.
Additional nitrite reduction experiments were performed to exclude any effects resulting from the isotopic composition of the substrate and to investigate the influence of the reaction temperature on the isotopomer ratio. All results are listed in Table 3.3. As expected, the experimental outcome verifies that different amounts of isotopic enrichment have no significant effect on the determined site preference. For the different reaction temperatures, within the scatter of the data no significant tendency could not be identified. The statistical error of the reported site preference (standard deviation of 3-4 measurements) does not reflect the actual accuracy of the measurement, but rather illustrates the reproducibility of the measurements at different concentration levels. The general precision of the technique is basically determined by the accuracy of integral determination and the temperature stability of the cell. The temperature affects the determined signal intensity ratio resulting from different rotational states. For the chosen lines, the effect has been calculated

Table 3.3: Experimental results for nitrous oxide formation from HNO dimerization (Nitrite reduction). Site preferences, δ^{SP}, were measured at variable temperature and isotopic composition of the substrate, R^S.

No.	$c(NO_2^-)$ / mol/L	$R^S(NO_2^-)$	$R^P(N_2O)$[2]	pH	T / K	$\delta^{SP} \times 1000$
(I)	0.136	0.179	0.294	0.64	298	33.2(11)
(II)	0.124	0.102	0.183	0.64	298	45.2(38)
(III)	0.126	0.101	0.182	0.66	298	43(11)
(IV)	0.136	0.157	0.265	0.60	298	40.0(80)
(V)	0.142	0.150	0.255	0.58	273	35.6(90)
(VI)	0.161	0.140	0.241	0.62	313	34.2(31)
(VII)	0.129	0.158	0.266	0.58	336	18.9(69)
IRMS[1]	0.05	0.0037	0.0074	1	298	30.6(17)

[1] taken from Toyoda *et al.*[19]

[2] isotopic composition of formed nitrous oxide, $R^P(N_2O)$, calculated from R^S

based on the partition functions to be on the order of 5‰/K. Errors in integral determination are reduced with increasing sample concentration. Typical standard deviations were on the order of 4‰ such that a precise isotopomer ratio could be obtained by averaging a certain number of sample spectra. However, based on Equation 3.7, absolute accuracy of the technique depends on the determined line strength parameters. Taking into account the statistical error of the line strength determination, possible errors are approximately 8‰ for the determined isotopomer ratio.

For the reduction experiment of nitrite, sufficient averaging yielded a precision of the integral determination < 1‰. Assuming a temperature uncertainty of 0.4 K gives an additional uncertainty of 2‰, such that an overall accuracy of 10‰ could be achieved.

In summary, taken together experimental and technical error sources, the average site preference of nitrite reduction derived from the cavity ringdown measurements is given by $\delta^{SP} \approx +40 \pm 10$‰. This value is significantly different from zero and underlines the preferred formation of the $^{14}N^{15}N^{16}O$ isotopomer. Although this value is slightly higher than the value obtained in IRMS measurements, $+30 \pm 2$‰, both results are comparable. Clearly, the IRMS measurement has a somewhat better precision, but, as outlined above, systematic errors in IRMS calibration call into question the accuracy of that technique. Thus, the reason for the remaining slight discrepancy between the CRDS and IRMS measurement remains uncertain at this point.

3.5 CONCLUSION

The FT-ICR mass spectrometric measurements of standard gas samples support the results of Westley *et al.*[15] that the two nitrous oxide isotopomers show a different fragmentation behavior. Moreover, it is dependent on the specific mass spectrometer

used and therefore careful calibration strategies are required when using mass spectrometry for isotopomer ratio determination. In contrast, the spectroscopic approach developed in this work enables the determination of the site preference of nitrous oxide samples by direct and absolute absorption measurements. The presented FT-ICR mass spectrometry measurements in combination with the cavity ringdown (CRD) spectra enabled a consistent assignment of isotopologue and isotopomer mass and absorption peaks in the spectra of the two isotopomer standard samples. Therefore, line strength parameters of selected lines could be determined with highest precision - a prerequisite for absolute isotopomer ratio measurements. Unfortunately, it turned out that pressure broadening effects prevented accurate analysis of samples with natural abundance of the ^{15}N isotope. Consequently, isotopically enriched species have been analyzed.

Recent progress in cavity mirror design, schemes to tightly lock diode lasers to optical cavities to maintain resonance, and the measurement at higher repetition frequency offer ways out to reach the required sensitivity for ambient samples in the near future. Compared to alternative optical techniques, this CRDS based methodology is less error prone with respect to spectral interference from other isotopologue absorption lines and allows for detection of almost purely Doppler broadened absorption lines in the NIR spectral region.

For the reduction of nitrite, which served as a test case, it was shown that N_2O is formed with a site preference of $\delta^{SP} = 40 \pm 10‰$. This independent result is in good agreement with previous IRMS results from Toyoda *et al.*[19] and supports theoretical arguments of Schmidt *et al.*[43] in favor of an isotopic fractionation during N-O bond cleavage. Indeed, the order of magnitude of the effect is basically consistent with a corresponding heavy atom isotope effect. An isotopic fractionation independent of isotopic abundance of the substrate, however, requires the formation and decomposition of a symmetric intermediate in the underlying mechanism. According to the mechanism of Bell and Kelly,[86] it is HNO dimerization (Equation 1.9) that leads to nitrous oxide formation and consequently it has been speculated about HONNOH and $^{-}$ONNO^{-} as potential symmetric intermediates.[19,43]

In the following chapter, the mechanism of HNO dimerization is investigated in more detail by quantum chemical methods to check the feasibility of these speculations.

4

FIRST PRINCIPLE DERIVED MECHANISM OF HNO DIMERIZATION

The most practical solution is a good theory.

— Albert Einstein (1879 - 1955)

4.1 SCOPE OF THE PROJECT

As outlined in the introduction (chapter 1) and the previous chapter (chapter 3), nitroxyl (HNO) has been considered to play a significant role in nitrous oxide formation both in chemical and biochemical formation pathways. Despite the fact that nitroxyl is a rather simple molecule, its chemistry has been controversially discussed recently.
Postulated as early as 1903 by Angeli as intermediate in $Na_2N_2O_3$ (Angeli's salt) decomposition in aqueous solution,[87] first direct detection of HNO in the gas phase by infrared spectroscopy succeeded in 1958.[88] Further pulse radiolysis experiments enabled HNO generation in solution and for the acid base pair HNO/NO^- a first pK_a of 4.7 was determined.[89] Although these results were questioned by some authors,[90] it led to the conclusion that NO^- instead of HNO is the dominant species under physiological conditions and this result found its way into the textbooks. Consequently, most experiments in the following years were interpreted to involve NO^-, till Bartberger *et al.*[91] presented calculations suggesting a considerably higher pK_a value of 7.2 for this equilibrium. This apparent discrepancy lead to a reevaluation of HNO chemistry and especially the role of the previously neglected spin states became part of the discussion. Because the ground state is singlet in the case of HNO and triplet in the case of NO^-, direct deprotonation involves a spin change. From a kinetic analysis of flash photolysis experiments of Angeli's salt, Shafirovich and Lymar[92] found evidence for a pK_a as high as 11.4, which is 7 orders of magnitude different from its textbook value mentioned above. This latter value has been confirmed theoretically[93] and is now the accepted value. These and further results pointed to the rather complex equilibrium according to[94]

$$^1\text{HNO} \rightleftharpoons {}^3\text{NO}^- (\rightleftharpoons {}^3\text{NOH} \rightarrow {}^3\text{HNO} \rightarrow {}^1\text{HNO}) \tag{4.1}$$

$^1NO^-$ has not been included in this scheme because it is calculated to be energetically approximately 80 kJ/mol above $^3NO^-$ and thus does not play a role in equilibration. Likewise, ^{3}NOH has been found to be 90 kJ/mol less stable than ^{1}HNO. In fact, pure existence of ^{3}NOH lacked experimental verification until 1999 when Maier *et al.*[95] were able to show that photo-excitation of ^{1}HNO at 10 K yields ^{3}NOH in a photo-equilibrium. Nonetheless, the isomer ^{3}NOH had initially been considered to be the primary reaction product of HNO forming reactions, but the findings that decomposition of many HNO sources forming a singlet species and nitroxyl is reversible showed that formed ^{1}HNO is the more likely product. All in all, ^{1}HNO has been found to be the dominant species present under physiological conditions.

Once formed, the rapid dimerization of nitroxyl in aqueous solution according to Equation 1.9 is one of the main reasons for the problems in studying nitroxyl chemistry. Most of the numerous experimental studies on HNO dimerization analyzed the corresponding gas phase dimerization reaction[96–99] followed by theoretical approaches to understand the underlying reaction mechanism and reaction kinetics.[100–102] Whereas most of these studies agreed on a bimolecular rate constant on the order of approximately 0.5-1.6 $\times$ 10^6 M^{-1} s^{-1} and assumed a preferred formation of the *trans* dimer in the initial step, the recombination barrier height and, more important, the sequential reaction mechanism leading to the final product nitrous oxide has been a controversial subject. The reaction in solution is even less well understood. The near diffusion limited rate constant, $k \approx 1.8 \times 10^9$ M^{-1} s^{-1}, determined by Bazylinski *et al.*[103] was corrected by Shafirovich and Lymar[92] to a much lower value of $k \approx 8 \times 10^6$ M^{-1} s^{-1}. This is still well above the gas phase rate constant. Although no intermediates could be observed in the sequential mechanism of the reaction, hyponitrous acid (*cis*) has been suggested to be the principal intermediate that decomposes to form nitrous oxide.
The intermediate formation of *cis*-hyponitrous acid and subsequent decomposition into nitrous oxide has also been suggested in the quite similar reaction of hydroxylamine with nitrite (Equation 1.10). Here, Ashcraft *et al.*[38–40] presented a series of publications aiming to reproduce the underlying reaction mechanism and kinetics of this complex reaction sequence in solution based on a simple quantum chemical model making use of continuum solvation models and catalytically acting explicit water. Despite various simplifications, the model reflects main features of the mechanism. The derived reaction pathways were consistent with previous reaction schemes derived from experiments.[35,37,104]

4.2 PROJECT OBJECTIVES

Detailed understanding of the formation mechanism of nitrous oxide via HNO dimerization Equation 1.9 should enable identification of the key intermediates involved in the reaction sequence leading to the observed isotopomer effect. The recent reevaluation of HNO chemistry clearly showed that it is ^{1}HNO that undergoes dimerization under physiological conditions instead of its conjugated base $^3NO^-$. However, so far suggested mechanisms and intermediates turn out to be partly inconsistent with the experimental results and the absence of detectable intermediates made it difficult to exclude certain pathways. Generally, it is suggested that hyponitrous acid is the most probable choice of a key intermediate.
As experiments apparently fail at this point to resolve this matter, quite accurate quantum chemical methods have been developed to determine thermodynamic and kinetic properties in solution. Considering the similarities of HNO dimerization and the comproportionation reaction of hydroxylamine and nitrite (Equation 1.10), a quantum chemical modeling approach based on simple continuum models appears feasible. In this chapter, a comprehensive modeling approach will be outlined that complies with the known kinetic results. Although the work of Raman *et al.*[38] revealed that the absolute accuracy of such a model is rather limited compared to the results of high level *ab inito* methods including more detailed solvation models, the most important features of the reaction system could be sufficiently resolved. By all

means, the advantage of this methodology lies in its computational cost effective description of numerous simultaneous reaction pathways.

4.3 THEORETICAL BACKGROUND

4.3.1 *Quantum chemistry and density functional theory*

According to the stationary Schrödinger equation, the eigenvalues of the Hamiltonian $\hat{H}$ correspond to the energy states of a molecular system described by the wave function ψ_{mol}.

$$\hat{H}\psi_{\text{mol}} = E\psi_{\text{mol}} \tag{4.2}$$

The solution of this equation requires the knowledge of the exact wave functions and the complete Hamiltonian of the overall system including the kinetic and potential energy operators of all nuclei and electrons. In general, the accurate solutions are not easily accessible. Relying on the Born Oppenheimer (BO) approximation it is justified to separate motion of the nuclei and the electrons. Treating the nuclei motion within an effective potential of the electrons and vice versa leads to a splitting of the fundamental equation into

$$\hat{H}_{\text{elec}}\psi_{\text{elec}} = (T_{\text{elec}} + V(R,r))\psi_{\text{elec}}(R,r) = E_{\text{elec}}(R)\psi_{\text{elec}}(R,r) \tag{4.3}$$

$$\hat{H}_{\text{nuc}}\psi_{\text{nuc}} = (T_{\text{nuc}} + E_{\text{elec}}(R))\psi_{\text{nuc}} = E_{\text{mol}}\psi_{\text{nuc}} \tag{4.4}$$

Note that in more general theories this result is no longer valid and cross terms between the two equations appear. However, within the BO approximation the separate solution of the electronic wave function yields the total electronic energy, whereas the energy levels for vibrational and rotational motion are determined by the nuclear wave function for a given electronic potential.
The Schrödinger equation for the electronic energy can be solved numerically, by using a so-called Slater determinant Φ as a trail wave function satisfying the fundamental requirements of asymmetry with respect to electron exchange.[105] As the correct wave function for a given molecule is basically unknown, one takes advantage of the axiom that the correct Slater-determinant yields the minimum energy, i.e., finding solutions of the Schrödinger equation becomes a minimization problem (self-consistent field method). The numerical optimization of a single Slater determinant, containing all electron orbitals ϕ_i, each constructed from a set of suitable parametrized functions, χ_j, (basis set), is the basis for the historically important Hartree-Fock (HF) method.

$$\min(E_{HF}) = \min(<\Phi|H|\Phi>) \text{ with } \Phi = A(\prod_i \phi_i) = A(\prod_i \prod_j \chi_{ij}) \tag{4.5}$$

Although this methodology yields most of the electronic energy $E_{\text{HF}} \approx 99\%\, E_{\text{elec}}$, it has fundamental deficits in describing the physical picture accurately due to the lack of electron correlation. In the HF method, each electron is assumed to interact with an effective field determined by all other electrons. For improved results either empirical corrections (semi-empirical methods) can be used or the electron correlation can be taken into account by using a multi-determinant wave function

set up by linear combinations of many slater determinants describing the electronic ground state and the excited electronic states. The latter approach is the basis for the quite accurate correlation interaction (CI), coupled cluster (CC) and Møller-Plesset methods (MP), which become highly computationally demanding with increasing size of the molecular system under study.
In DFT, the problem to determine the accurate electronic energies is tackled from a different direction. Hohenberg and Kohn[106] proved on the one hand that the ground state energy can be directly correlated with the electron density, but on the other hand left open the question how. Later it was shown that many energy terms of the Hamiltonian can be easily expressed as a functional of electron density, which in turn can be expressed as a sum over squared single electron functions. The latter are called Kohn-Sham orbitals and can be optimized by the self-consistent field method in the same manner as in the HF approach. However, for certain parts of the energy terms (the exchange-correlation functional) the exact dependence on density remains unknown and approximations have to be used. For this purpose, various functionals for correlation, exchange or both (hybrid) such as LYP, TPSS, or the popular B3LYP functional have been developed. The main advantages of DFT are an improved treatment of electron correlation at comparably low computational costs and a better scaling behavior of the calculations with increasing electron number.
The results of these electronic structure calculations can be used to derive thermochemical relevant quantities. Once the electronic energy of the system is known, an additional frequency analysis enables the determination of the partition functions making gas phase molar enthalpy ΔH_{Gas}, entropy S_{Gas}, and Gibbs energy ΔG_{Gas} available, via the relations derived from statistical thermodynamics.

4.3.2 *Solvent models and acid-base equilibria*

In solution, an additional energy term is added to the corresponding Hamiltonian to account for solvation effects according to

$$(\hat{H} + \hat{V}_R)\psi_{\mathrm{mol}} = E_{\mathrm{soln}}\psi_{\mathrm{mol}} \tag{4.6}$$

Consequently, the Gibbs free energy of a reaction in solution, $\Delta_{\mathrm{r}}G^*_{\mathrm{Soln}}$, differs from the gas phase Gibbs free energy. This is outlined in the following scheme for a simple equilibrium between A and B:

$$\begin{array}{ccc} \mathrm{A}_{(g)} & \overset{\Delta_{\mathrm{r}}G^*_{\mathrm{Gas}}}{\rightleftharpoons} & \mathrm{B}_{(g)} \\ \Delta G^*_{\mathrm{Solv}}(\mathrm{A})\downarrow & & \downarrow \Delta G^*_{\mathrm{Solv}}(\mathrm{B}) \\ \mathrm{A}_{(aq)} & \overset{\Delta_{\mathrm{r}}G^*_{\mathrm{Soln}}}{\rightleftharpoons} & \mathrm{B}_{(aq)} \end{array}$$

The free enthalpy in solution, $\Delta_{\mathrm{r}}G^*_{\mathrm{Soln}}$ can be derived from

$$\Delta_{\mathrm{r}}G^*_{\mathrm{Soln}} = \Delta_{\mathrm{r}}G^*_{\mathrm{Gas}} - \Delta G^*_{\mathrm{Solv}}(\mathrm{A}) + \Delta G^*_{\mathrm{Solv}}(\mathrm{B}) \tag{4.7}$$

Accurate quantum-chemical determination of solvation enthalpies, $\Delta G^*_{\mathrm{Solv}}$ is rather difficult. A complete quantum mechanical treatment of all solvent molecules is in most cases computationally too expensive and thus not feasible. Therefore, approximations such as polarization continuum models are generally used to describe

the solvated systems. The general concept behind these models is to determine the individual contributions to the free solvent energy directly from the structure of the molecule. Typically, the solvation energy in polarization continuum models is decomposed into three contributions:[105]

$$\Delta G^*_{\text{Solv}} = \Delta G_{\text{cavity}} + \Delta G_{\text{dispersion}} + \Delta G_{\text{electrostatic}} \tag{4.8}$$

Here, ΔG_{cavity} describes free enthalpy changes stemming from the formation of a cavity in the solvent, $\Delta G_{\text{dispersion}}$ is the solute-solvent interaction energy due to dispersion and, finally, $\Delta G_{\text{electrostatic}}$ describes electrostatic interactions with the polarized medium. These terms are often assumed to be directly proportional to the surface area and/or the electrostatic potential and therefore they can be calculated from the electronic structure of the solute alone. However, it is necessary to choose a suitable representation of the cavity of the molecule. More molecule-like shapes are generally more accurate, but for those models simple assumptions for electrostatic interactions fail such that numerical solutions for the system are needed. A popular implementation of such a model is the polarizable continuum model (PCM) in its various forms such as IEF-PCM, C-PCM, and I-PCM.
A special case of equilibrium in solution is the acid-base reaction

$$\mathrm{AH}_{(aq)} \rightleftharpoons \mathrm{A}^-_{(aq)} + \mathrm{H}^+{}_{(aq)} \tag{4.9}$$

The corresponding $\mathrm{p}K_a$ of the acid is directly related to the free enthalpy of the above reaction according to

$$\mathrm{p}K_\mathrm{a} = \frac{\Delta_\mathrm{r} G^*_{\text{Soln}}}{RT\ln(10)} \tag{4.10}$$

The direct use of Equation 4.10 to determine the $\mathrm{p}K_\mathrm{a}$ is often inaccurate. One reason is that the experimental free solvation enthalpy of the proton is needed which is not known accurately. A second reason is that the products in contrast to the educt are ionic species with high solvation enthalpies such that inaccuracies of the energy derived from the solvent model affects products and the educt quite differently.
One alternative approach is the so-called proton exchange scheme[107] following a thermodynamic cycle according to

$$\begin{array}{ccccc}
\mathrm{HA}_{(g)} & + & \mathrm{Ref}^-{}_{(g)} & \overset{\Delta_\mathrm{r} G^*_{\text{Gas}}}{\rightleftharpoons} & \mathrm{A}^-{}_{(g)} + \mathrm{HRef}_{(g)} \\
\Delta G^*_{\text{Solv}}(\mathrm{HA}) \downarrow & & \Delta G^*_{\text{Solv}}(\mathrm{Ref}^-) \downarrow & & \downarrow \Delta G^*_{\text{Solv}}(\mathrm{A}^-) \quad \downarrow \Delta G^*_{\text{Solv}}(\mathrm{HRef}) \\
\mathrm{HA}_{(aq)} & + & \mathrm{Ref}^-{}_{(aq)} & \overset{\Delta_\mathrm{r} G^*_{\text{Soln}}}{\rightleftharpoons} & \mathrm{A}^-{}_{(aq)} + \mathrm{HRef}_{(aq)}
\end{array}$$

Consequently the $\mathrm{p}K_\mathrm{a}$ is given by

$$\mathrm{p}K_\mathrm{a} = \frac{\Delta_\mathrm{r} G^*_{\text{Soln}}}{RT\ln(10)} + \mathrm{p}K_\mathrm{a}(\mathrm{HRef}) \tag{4.11}$$

The advantage of this procedure is a strong error compensation thus yielding much more reliable $\mathrm{p}K_\mathrm{a}$ values. In cases when the reference acid is similar, $\mathrm{p}K_\mathrm{a}$ can be determined within ± 1 units.[107]

4.4 PUBLICATION II: DIMERIZATION OF HNO IN AQUEOUS SOLUTION: AN INTERPLAY OF SOLVATION EFFECTS, FAST ACID BASE EQUILIBRIA, AND INTRAMOLECULAR HYDROGEN BONDING?

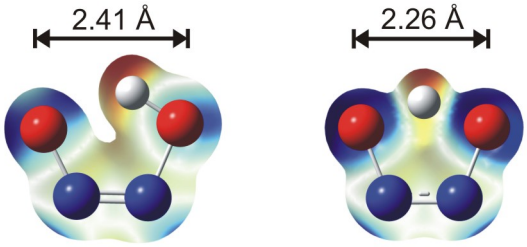

Own contributions in the paper:

- All calculations presented in the publication.
- Postulate of *cis* isomeric preference and its kinetic explanation within a dipole moment approximation.
- Discussion of the thermodynamic and kinetic stability of the isomers.
- Application of a proton exchange scheme to determine pK_a values.
- Assessment of the two presented reaction schemes and deduction of feasible reaction sequences.
- Draft of publication.

Additional work within this project, not presented in the paper:

- Kinetic simulation of the presented acid-base mechanism
- Experimental validation experiments of pH-dependent *trans*-hyponitrite and Piloty's acid decomposition kinetics by UV/Vis spectroscopy

JACS
JOURNAL OF THE AMERICAN CHEMICAL SOCIETY

ARTICLE

pubs.acs.org/JACS

Dimerization of HNO in Aqueous Solution: An Interplay of Solvation Effects, Fast Acid−Base Equilibria, and Intramolecular Hydrogen Bonding?

Carsten Fehling* and Gernot Friedrichs*

Institut für Physikalische Chemie, Christian-Albrechts-Universität zu Kiel, Olshausenstraße 40, 24098 Kiel, Germany

Supporting Information

ABSTRACT: The recent unraveling of the rather complex acid−base equilibrium of nitroxyl (HNO) has stimulated a renewed interest in the significance of HNO for biology and pharmacy. HNO plays an important role in enzymatic mechanisms and is discussed as a potential therapeutic agent against heart failure. A cumbersome property for studying HNO reactions, its fast dimerization leading to the rapid formation of N_2O, is surprisingly far from being well understood. It prevents isolation and limits intermediate concentrations of nitroxyl in solution. In this study, a new mechanism for the HNO dimerization reaction in aqueous solution has been theoretically derived on the basis of DFT calculations. Detailed analysis of the initial reaction step suggests a reversal of the *cis*−*trans* isomer preference in solution compared to the corresponding gas phase reaction. In contrast to a gas phase derived model based on intramolecular rearrangement steps, an acid−base equilibrium model is in agreement with previous experimental findings and, moreover, explains the fundamental differences between the well studied gas phase reaction and the solvent reaction in terms of polarity, *cis*−*trans* isomerizations, and acidities of the intermediates. In the case of *cis*-hyponitrous acid, the calculated pK_a values of the acid−base equilibria were found to be significantly different from the corresponding experimental value of the stable *trans* isomer. Under physiological conditions, N_2O formation is dominated by the decomposition of the unstable monoanion *cis*-$N_2O_2H^-$ rather than that of the commonly stated *cis*-HONNOH.

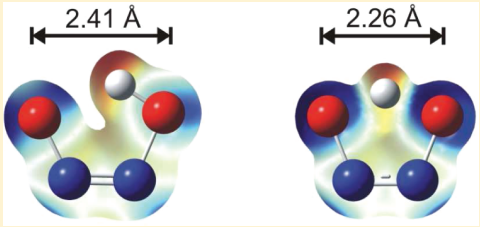

1. INTRODUCTION

The interest in the chemistry of nitroxyl (HNO) in solution has rapidly increased owing to two important findings that have led to a reevaluation of the significance of HNO among the nitrogen species in physiologically and biologically relevant systems.[1] First, the previously reported pK_a value of nitroxyl, pK_a = 4.2, has been redetermined by both experiment and theory and has been corrected to the dramatically different value 11.4.[2,3] The second important issue was the reassessment of the HNO dimerization rate constant in solution, which was found to be on the order of 8×10^6 M^{-1} s^{-1} and thus significantly lower than the previously reported nearly diffusion limited value of 2×10^9 M^{-1} s^{-1}.[2] The much longer lifetime of HNO in aqueous solution and its certain stability under physiologically relevant conditions enables reactions in solution prior to the dimerization reaction itself. Experimental studies revealed a reaction selectivity of HNO that deviates strongly from that of NO. For example, HNO reacts rapidly and selectively with thiols, whereas NO requires activation by species enabling its oxidation, e.g., transition metals.[4] The unique chemistry combined with the low radius of action of freshly generated HNO has led to a discussion about possible site specific biological effects and the use of potential chemical HNO sources as pharmaceutical agents.[1] However, the observation of DNA strand breakage in the presence of HNO, which is more strongly induced under acidic conditions (pH < 6), has been suggested as evidence for a strong oxidative capability.[5] This unfavorable property was later attributed to the formation of OH radicals from a side reaction of HNO dimerization.[6]

Besides this pharmaceutical interest, direct HNO dimerization was postulated as a chemical pathway for nitrous oxide formation from nitrous oxide reductase (NOR) enzymes found in nitrifying and denitrifying bacteria and fungi. Although new insights into the corresponding NOR enzyme mechanism underlined that the N−N bond formation takes place at the active site of the enzyme and is catalyzed by a binuclear iron complex, the role of HNO reactions in several enzyme mechanisms, especially due to its high affinity to transition metal complexes, remains unclear.[7]

Despite its importance and many experimental studies of this reaction,[2,8−10] the detailed mechanism of the HNO dimerization in solution is poorly understood. Because of rapid sequential isomerization steps and proton transfer reactions, often N_2O formation itself is the only accessible experimental indicator for the ongoing reaction sequence.[1] Typically, hyponitrous acid is stated as the crucial intermediate species that decomposes to form nitrous oxide:

$$HNO + HNO \rightarrow [HONNOH] \rightarrow N_2O + H_2O \qquad (1)$$

Received: August 11, 2011
Published: October 17, 2011

Whereas the kinetics of the overall reaction were found to be second order with respect to HNO concentration in pulse radiolysis and flash photolysis studies,[2] to the best of our knowledge neither has the assignment of *cis*-hyponitrous acid as intermediate been experimentally verified nor does a valid mechanism for the overall reaction sequence in solution exist. In the case of Angeli's salt (sodium α-oxohyponitrite), a widely used chemical HNO source, several isotope labeling studies revealed that N-protonation to $O^{15}N(H)^{14}NO_2$ and the subsequent decomposition form isotopically pure $^{15}N^{15}NO$.[11] The initially formed N−N bond of the HNO dimer is therefore generally believed to be preserved in a sequence of unimolecular reactions eventually forming N_2O.

Several experimental and theoretical studies have been performed to clarify the mechanism of the gas phase recombination reaction.[12,13] The temperature dependence of the rate constant indicates a small activation barrier on the order of $E_0 \approx 4-14$ kJ/mol and a low preexponential Arrhenius factor of about 1×10^9 cm^3 mol^{-1} s^{-1}.[12,13] The latter is in accordance with a high entropy of activation and thus a highly ordered transition state.[12] Attempts were made to model the complete scheme of sequential reactions on the basis of *ab initio* calculations assuming *trans*-ON(H)N(H)O as the initial dimer species. In agreement with other quantum chemical models,[14,15] the *trans*-ON(H)N(H)O isomer has been found to be significantly more stable than the *cis*-ON(H)N(H)O isomer. Consequently, the formation and further reactions of the *cis* isomer have been neglected.

Despite these sound schemes and measurements of the reaction in the gas phase, some obscurities remain for the reaction in solution. First of all, the initial reaction is faster in solution (8×10^6 M^{-1} s^{-1})[2] than it is in the gas phase ($0.5-1.6\times 10^6$ M^{-1} s^{-1}).[12] Second, the final decomposition step leading to the formation of nitrous oxide has been assigned to different tautomers and isomers in the literature.[12,14,16] Furthermore, most experimental studies agree on stoichiometric and fast nitrous oxide generation from HNO dimerization in solution,[17,18] whereas theoretical gas phase studies report *trans*-hyponitrous acid formation as an intermediate or byproduct.[12] Of course, the results of gas phase studies cannot be directly compared with the outcome of the reaction in solution. For the gas phase reaction, energy conservation has been assumed for the initial dimer and subsequent intermediates, thus allowing for rapid crossing of the involved reaction barriers.[12,14] In contrast, fast collisional deactivation of the energetically excited initial adduct takes place in solution, resulting in stabilization of the dimer and possibly much different overall kinetics.

The aim of this work is to provide a theoretical backbone to explain the diverging experimental results and mechanistic interpretations in a unified model. Following a more detailed analysis of the initial dimerization reaction, an existing gas phase mechanism relying on intramolecular rearrangement steps has been tested with regard to its applicability on the reaction in solution. In DFT based calculations, solvent effects have been taken implicitly into account by applying polarization continuum models and, in some cases, explicit solvent molecules have been included to allow for solvent based catalysis. Detailed analysis of possible isomerization steps as well as the involvement of ionic species led to the development of a mechanistic model based on fast acid−base equilibria. Theoretically derived pK_a values were used to deduce the most feasible reaction pathways. The predicted product yields and pH dependencies are critically compared with the identified products of previous experimental studies, showing that the proposed mechanism is consistent with the reported, sometimes controversially discussed literature findings.

2. COMPUTATIONAL METHODOLOGY

Quantum chemical calculations were performed utilizing the Gaussian 09 program suite.[19] If not stated otherwise, DFT calculations presented in this study were based on the B3LYP functional using Dunning's correlation consistent aug-cc-pVTZ basis set.[20] Solvation effects were taken into account by the polarization continuum models CPCM and IEFPCM using UFF cavities.[21] After optimization, harmonic frequency analysis revealed minimum and transition state (TS) structures (zero and one imaginary frequency, respectively). TS structures were checked to connect the respective minimum structures by following the intrinsic reaction coordinates.

To derive accurate theoretical pK_a values within Δp$K_a = \pm 1$, the concept of proton exchange was applied.[22] In this scheme, a structurally similar acid (HRef) is used as internal reference such that the error-prone solvation energy of the proton is not required:

$$HX + Ref^- \rightleftharpoons X^- + HRef \tag{2}$$

The pK_a value of the acid of interest is deduced from free enthalpies of solution and the corresponding experimental pK_a value of the reference acid:

$$pK_a = \frac{\Delta G^*_{soln}}{RT\ln(10)} + pK_a(HRef) \tag{3}$$

The free enthalpy of the reaction in solution ΔG^*_{soln}(standard state 1 mol/L) is determined from a valid thermodynamic cycle consisting of the gas phase enthalpy of reaction, ΔG^*_{gas} and contributions of the free enthalpies of solvation compared to the products and educts.

$$\Delta G^*_{soln} = \Delta G^*_{gas} + \sum_{products} \Delta G^*_{solv} - \sum_{educts} \Delta G^*_{solv} \tag{4}$$

trans-Hyponitrous acid was chosen as a suitable reference acid. It is fairly stable in solution such that standard titration experiments could be used to determine $pK_{a,1} = 7.18$ and $pK_{a,2} = 11.54$ for the first and the second deprotonation, respectively.[23]

3. RESULTS AND DISCUSSION

3.1. Initial Dimerization in Solution. The initial dimerization of HNO forming the *trans* or *cis* isomer sets the starting point for the reaction sequence. As will be discussed in more detail below, the initial isomer preference turns out to define the overall product formation pathway. Once formed, *cis*−*trans* isomerization cannot take place due to significant energy barriers. In order to comprehend the isomer preference of the reaction in solution, a few structural considerations are necessary.

Thermodynamic Equilibrium. The DFT calculations show that introducing a solvent cage in terms of the polarization continuum model leads to quite different stabilizations of the involved *cis* and *trans* species (**2**,**3**). Selected free enthalpies of solvation, the dipole moments, and the calculated equilibrium constants are listed in Table 1. Here, the results both of the standard UFF cavity parametrization and of the rather novel SMD model[24] are shown in comparison to emphasize the uncertainties associated with the description of solute parameters in highly dielectric media such as water. For example, the changes of dipole moments and the solvent enthalpies of the highly dipolar species deviate significantly. However, the overall trends

Table 1. Dipole Moments, μ, Free Enthalpies of Solvation, ΔG^*_{solv}, and Free Enthalpies Relative to the Educt HNO in the Gas Phase, ΔG^*_{gas}, and in Solution, ΔG^*_{soln}[a]

				IEFPCM (UFF)			IEFPCM (SMD)	
species		μ_{gas}	ΔG^*_{gas}	μ_{soln}	ΔG^*_{solv}	ΔG^*_{soln}	μ_{soln}	ΔG^*_{solv}
HNO	**1**	1.65		2.07	−9.9		2.29	−10.8
2 × HNO	**1**		0.0		−19.8	0.0		−21.6
cis-ON(H)N(H)O	**2**	5.45	−46.7	7.20	−57.2	−84.5	8.04	−110.9
trans-ON(H)N(H)O	**3**	0.00	−53.3	0.00	−34.2	−68.3	0.00	−61.0
TST *trans*-ON(H)N(H)O	**1** → **3**	0.00	34.8	0.00	−18.5	36.0	0.00	−11.0

[a] Calculations are based on the polarization continuum models IEFPCM(UFF) and IEFPCM(SMD). Units are Debye and kJ/mol.

are similar such that the conclusions drawn from the two different solvent models are identical.

The main contributions for stabilization in solution stem from electrostatic interactions originating from changes of polarity and polarizability of the solute. As already discussed by Glaser et al.,[25] the two dipole moment vector components cancel in the case of the *trans* dimer (**3**), whereas for the *cis* dimer (**2**) the net dipole moment is even larger than the sum of the dipole moments of the two HNO monomers. Due to the structural adjustment of the equilibrium geometry in dielectric media, the magnitude of the net dipole moment is further increased. Thus, dipole−dipole interactions contribute significantly to the *cis* dimer (**2**) stabilization in aqueous solution. In contrast, the stabilization of the *trans* dimer (**3**) compared to the monomer is rather an effect of increased polarizability of the dimer species and increased polarity due to the shift of electron density along the N−O bond toward oxygen. These effects are basically independent of the isomer structure and thus equally contribute to the stabilization of the two isomers. Overall, due to the large difference in free enthalpies of solvation between the *cis* and *trans* dimers, the thermodynamic preference of the *trans* dimer (**3**) in the gas phase is more than compensated such that the *cis* species (**2**) is more stable in solution.

Solvent Effect on Long-Range Interactions. The question arises how the rate constants of the dimer formation are affected by the solvent. In comparison with the gas phase reaction, effects might originate from different contributions of long-range interactions such as hydrogen bonding and dipole−dipole interactions. Peters[26] has shown for the gas phase species that intermolecular hydrogen bonding can stabilize metastable *trans*-like dimer structures by ≈9 kJ/mol at N−N distances around 2.5 Å. In addition, using the dipole moment stated in Table 1, the dipole−dipole interaction energies at this distance and for a parallel orientation can be estimated to be on the order of 2−4 kJ/mol. This interaction is attractive in the case of a *trans* orientation and repulsive in the case of the *cis* orientation. Both types of interaction are thus in favor of *trans* dimer formation in the gas phase. However, comparing these long-range HNO−HNO interaction energies with the calculated solvation enthalpies of two HNO molecules (>20 kJ/mol) reveals that in aqueous solution the solute−solvent dipole−dipole and hydrogen bonding interactions dominate. In other words, the long-range interactions are shielded by solvation shells and thus can be assumed to play no significant role for the reaction in solution.

Solvent Effect on Bond Formation. At shorter N−N distances (<2.0 Å), on the one hand, energetic stabilization takes place due to mutual $n(N') \rightarrow \pi^*(N-O)$ orbital interactions (finally leading to σ- and π-(N−N) bond formation). On the other hand, repulsive interactions originate from the proximity of nitrogen and oxygen lone pairs. In fact, our own DFT calculations revealed a transition state structure for the *trans* species (**3**) formation, but with no significant energy barrier relative to the HNO molecules. This result is contrary to earlier theoretical studies[15,14] reporting an energy barrier up to 45 kJ/mol, but it is in line with the MP4 results of Lin et al.[12] The experimental temperature dependence of the rate constant in the gas phase also suggests a low dimerization barrier for *trans* dimer (**3**) formation of merely 4−14 kJ/mol.[13,27] Furthermore, the low preexponential Arrhenius factor found in the experiments and the calculated free enthalpy differences underline the formation of a free enthalpy barrier. Instead of enthalpy it is the strong decrease of entropy during the reaction that determines the overall rate.

As a result of the strongly exothermic character of the reaction, the rate determining free enthalpy maximum is located at the early bond formation stage. From the DFT gas phase model, a rough estimate of the corresponding N−N distance of 1.7 Å was obtained. Due to the strong stabilization of the products in solution, this maximum can be assumed to shift even further outward. At this early stage of the reaction, only a minor change of polarizability and polarity of the NO bond has taken place. In contrast, as a result of the required relative orientation of the two HNO fragments, the net dipole moment has already vanished for *trans* dimer formation but has increased or at least has been preserved for *cis* dimer formation. Thus, it can be expected that formation of the dipolar *cis* dimer is preferred due to the solvent effect.

Rate Increase in Solution. In the gas phase, overall HNO dimerization reaction rate constants of $0.5-1.6 \times 10^6\ M^{-1}\ s^{-1}$ have been determined and theoretical isomer specific rate constants predict an initial isomer ratio of 3 to 1 in favor of the *trans* adduct (**3**).[12,13] The recently reported aqueous phase rate constant,[2] $8 \times 10^6\ M^{-1}\ s^{-1}$, is significantly higher than the gas phase rate constant, but it is still well below the diffusion limit. Shafirovich and Lymar[2] related this rate enhancement in solution to the free enthalpy of solvation of HNO by implicitly assuming similar free enthalpies of solvation of HNO and the activated complex. However, in light of the distinct dipole moment changes taking place during the reaction, this assumption is questionable. Instead, the overall solvent effect on the rate constant, $\Delta_{solv}\Delta G^{\ddagger}$, has to be dissected into contributions of reactant and transition state free enthalpies of solvation, ΔG^{R}_{solv} and $\Delta G^{\ddagger}_{solv}$, according to[28]

$$\Delta_{solv}\Delta G^{\ddagger} = \Delta G^{\ddagger}_{solv} - \Delta G^{R}_{solv} \quad (5)$$

Considering the loss of dipole moment and with it a relative increase of the transition state barrier in the case of the *trans*

dimer (**3**), it appears unlikely that the observed rate constant enhancement in solution originates from this pathway. In contrast, the better stabilization of the transition state structure of the *cis* dimer (**2**) is expected to considerably change the ratio of the formed isomers.

A quantitative description of solvent effects based on solute−solvent dipole−dipole interactions can be based on the theoretical model given by Kirkwood.[29] Along those lines, by taking into account dipole moment stabilization on the free enthalpy of activation, it is possible to estimate the change of rate constants going from the gas phase to the solution.[28] Assuming that the change of dipole moment is the dominating effect and the additional solvent specific effects such as hydrogen bonding are similar for the two isomers, the change of the isomer ratio of the initial HNO dimerization rate constants can be obtained from the following:

$$\frac{k_{cis,\,\mathrm{soln}}}{k_{trans,\,\mathrm{soln}}} = \frac{k_{cis,\,\mathrm{gas}}}{k_{trans,\,\mathrm{gas}}} \exp\left(\frac{1}{4\pi\varepsilon_0}\frac{1}{k_B T}\left(\frac{\varepsilon_r - 1}{2\varepsilon_r + 1}\right)\left(\frac{(\mu^{\ddagger}_{cis})^2}{{r_{cis}}^3} - \frac{(\mu^{\ddagger}_{trans})^2}{{r_{trans}}^3}\right)\right) \quad (6)$$

Here, ε_r is the dielectric constant of the solvent, $\mu_i^{\ddagger}$ is the transient dipole moment of the molecular structure corresponding to maximum free enthalpy, and r_i is the effective radius of the dimer complex in solution. The expression provides a lower limit for the estimated change of the isomer ratio, since the effects in highly dielectric media such as water are underestimated. With an effective dipole moment of ≈4.5 D, a calculated effective radius of 3.2 Å for the structure corresponding to the maximum free enthalpy of the *cis* dimer complex, and a negligible dipole moment of the *trans* dimer ($\mu^{\ddagger}_{trans} = 0$), the exponential term in eq 6 accounts for a factor of 1500. Combining this number with the reported 3-fold isomer preference in the gas phase, an overall isomer ratio in solution of $k_{cis,\mathrm{soln}}/k_{trans,\mathrm{soln}} = 500$ is predicted, hence strongly in favor of the *cis* isomer. Similarly, using a calculated effective radius of 2.9 Å for the HNO monomer, the equivalent equation for $k_{cis,\mathrm{soln}}/k_{cis,\mathrm{gas}}$ predicts a rate constant increase of approximately 30 for *cis* dimer (**2**) formation in solution. Again, taking into account the stated 3-fold *trans* isomer preference in the gas phase, this yields an approximately 8-fold increase of the overall rate constant—in very good agreement with the experimental 14-fold rate enhancement found in solution.

In summary, due to additional stabilization effects arising from dipole−dipole interactions and in contrast to the gas phase result, the *cis* dimer (**2**) can be considered to be the by far more favorable adduct in solution.

3.2. Impact of Solvation on Sequential N_2O Formation. The change of the initial isomer ratio raises the question if the previously discussed sequential gas phase reaction models[12,14] result in feasible N_2O formation pathways in solution as well. In the simplest case, the sequential gas phase and solvent mechanisms are equivalent and the influence of the solvent on the overall energetics would give a valid explanation of the much more rapid formation of N_2O in solution compared to the gas phase. In this section, the effects of solvation have been treated implicitly and explicitly to investigate this hypothesis.

Implicit Solvent Effect. Starting from the gas phase reaction schemes reported in the literature,[12] the implicit effect of the solvent on the energies of possible intermediates and transition state structures has been determined by applying the IEFPCM-(UFF) solvent model. The resulting reaction path diagram is shown in Figure 1. The corresponding structures and energies are listed in the ESI.

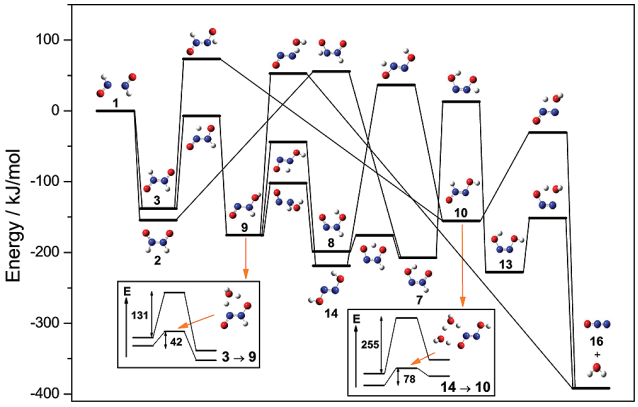

Figure 1. Implicit and explicit (inset) solvation effects on the intermediate species assuming the gas-phase model for HNO dimerization. Shown energy levels represent the electronic energies of the optimized ground state and transition state structures in solution relative to the educt energies. The two insets illustrate transition state structures including catalytically active explicit water molecules resulting in significant decreases of the corresponding activation energies due to hydrogen bonding. As outlined in the text, none of the shown pathways (although thermodynamically feasible) reflect the experimental result of rapid nitrous oxide formation in solution adequately.

It turns out that, except for the initial dimer, in comparison with the gas phase scheme, only small changes of the relative energies arise such that the mechanism remains thermodynamically feasible and the main possible pathways are similar to the gas phase reaction mechanism as discussed by Lin et al.[12] Besides the possible *cis*−*trans* isomerization **9** → **8**, basically 1−3 and 1−2 hydrogen shifts are involved in N_2O formation.

$$\textit{trans}-\mathrm{ON(H)N(H)O}\ (\mathbf{3}) \rightarrow \mathbf{9} \rightarrow \mathbf{8} \rightarrow \mathbf{7} \rightarrow \mathbf{13} \rightarrow \mathbf{16} \qquad E_0^{\max} = 220\ \mathrm{kJ/mol} \quad (7)$$

$$\rightarrow \mathbf{10} \rightarrow \mathbf{16} \qquad E_0^{\max} = 210\ \mathrm{kJ/mol} \quad (8)$$

$$\rightarrow \mathbf{9} \rightarrow \mathbf{16} \qquad E_0^{\max} = 230\ \mathrm{kJ/mol} \quad (9)$$

$$\rightarrow \mathbf{9} \rightarrow \mathbf{14} \rightarrow \mathbf{10} \rightarrow \mathbf{16} \qquad E_0^{\max} = 255\ \mathrm{kJ/mol} \quad (10)$$

$$\textit{cis}-\mathrm{ON(H)N(H)O}\ (\mathbf{2}) \rightarrow \mathbf{7} \rightarrow \mathbf{13} \rightarrow \mathbf{16} \qquad E_0^{\max} = 220\ \mathrm{kJ/mol} \quad (11)$$

Here, $E_0^{\max}$ specifies the highest occurring barrier for each reaction pathway. Note, that the reaction pathways according to eqs 7 and 11 correspond to the commonly cited scheme via *cis*-hyponitrous acid (**13**). In principle, eq 10 could serve as an explanation for the formation of *trans*-hyponitrous acid (**14**) in the reaction sequence, as predicted for the gas phase reaction. With $E_0^{\max} > 200$ kJ/mol for all possible reaction pathways, the reaction barriers are way too high to be consistent with a rapid reaction found in the experiment. A possible reason for this discrepancy might be that the influence of the solvent is not reflected adequately by the simple change of the dielectric constant assumed in the polarization continuum model. Additional stabilization by means of hydrogen bonds is not described by such an implicit modeling approach.

Explicit Solvent Effect. Therefore, in a next step, we explicitly included single solvent molecules in the reactions. A similar approach was recently presented by Ashcraft et al.[30] to determine the rate constants of hydroxylamine oxidation in nitric acid, which is largely comparable to the scheme presented here.

Table 2. Theoretical Solvent Free Energies and Reaction Barriers in kJ/mol and p*K* Values for Isomerization Equilibria Determined Using the IEFPCM(UFF) Model[a]

reaction				equilibrium			TST	
educt		product		$\Delta(\Delta G^*_{solv})$	$\Delta_r G^*_{soln}$	p*K*	$\Delta E^{\ddagger}_{soln}$	$\Delta G^{\ddagger}_{soln}$
trans-ON(H)N(H)O	**3**	*cis*-ON(H)N(H)O	**2**	−23.1	−16.3	−2.85	n.a.	n.a.
trans-ON(H)NO$^-$	**5**	*cis*-ON(H)NO$^-$	**4**	−16.3	−11.3	−1.98	172.0	164.5
trans-HON(H)NO	**9**	*cis*-HON(H)NO	**8**	4.8	−21.3	−3.73	78.0	73.4
trans-HONN(H)O	**10**	*cis*-HONN(H)O	**7**	6.9	−24.2	−4.23	242.0	241.7
trans-ONNO^{2-}	**11**	*cis*-ONNO^{2-}	**6**	−17.8	1.6	0.28	n.a.	n.a.
trans-HONNO$^-$	**15**	*cis*-HONNO$^-$	**12**	8.8	−32.2	−5.71	232.2	226.0
trans-HONNOH	**14**	*cis*-HONNOH	**13**	1.8	−9.2	−1.61	n.a.	n.a.

[a] The label "n.a." indicates that bond dissociation was found to be energetically more favorable. In those cases, relaxed potential energy scans were performed showing that barriers of at least 200 kJ/mol are involved.

In agreement with their results, the reaction barriers for the 1−3 hydrogen shift reactions were found to be significantly lowered when a single water molecule was included. As shown in the left inset of Figure 1, the water molecule forms a six membered ring structure that is geometrically and energetically favorable and catalyzes the hydrogen atom transfer. The corresponding reaction barrier decreases from 131 to 42 kJ/mol. In the case of 1−2 hydrogen shifts, the resulting five membered ring structure is geometrically too demanding, but analogous stabilizations of the transition state barriers were found by allowing for two explicit water molecules instead (e.g., right inset of Figure 1).

In contrast, we were unable to locate similarly stabilized structures for the reactions **9** → **16** and **10** → **16**. In these cases, the proton transfer is coupled with the dissociation and hydrogen bond structures are less stable due to the lower charge at the involved oxygen atom. Consequently, the direct elimination of water from the intermediates (**9**, **10**) remains energetically unfeasible and a major contribution of these pathways to nitrous oxide formation appears unlikely.

Surprisingly, no stabilization was found for the calculated transition state structure of the reaction **7** → **13** as well—in contrast to the analogous reaction of the *trans* isomer **10** → **14**. The corresponding formation of *cis*-hyponitrous acid (**13**) is crucial, however, for N_2O formation both from the *trans* dimer (**3**) according to eq 7 and from the preferred *cis* dimer (**2**) in eq 11. It is interesting to note that this important reaction step has been neglected in recent reaction schemes, although significant barriers are involved.[30,31] Instead, Raman et al.[31] implicitly assumed a fast *cis*−*trans* isomerization from **14** to **13**. As will be discussed below, such an isomerization step is unfeasible.

In summary, in the presented intramolecular reaction scheme, both excluding and including explicit water, at least one elementary step within the N_2O formation reaction sequence involves kinetically unfavorable high energy barriers. Although *cis*-hyponitrous acid (**13**) has been assumed throughout the literature as the principle species decomposing rapidly to form nitrous oxide, neither the simple solution model nor the inclusion of catalytically acting water molecules reveal possible pathways to the formation of the *cis*-hyponitrous acid (**13**) intermediate. Note, however, that the reaction sequence remains energetically downhill and thus is thermodynamically feasible. Moreover, certain intramolecular proton transfer reactions with low barriers (e.g., **8** → **7**) can play a role, and catalytically acting water can lower reaction barriers quite significantly such that reactions such as **3** → **9** become feasible in aqueous solution. Finally, the intramolecular scheme reveals that the often discussed, simple decomposition of the molecular species (**9**, **10**, **13**)[12,14,16] into nitrous oxide is inaccessible or very slow.

3.3. Isomerization and *cis*−*trans* Equilibria. Failure of the straightforward sequential reaction scheme discussed in the previous section calls for alternative reaction models. So-far neglected options are inclusion of possible *cis*−*trans* isomerizations and dissociation into ionic species. In this section, the first option will be discussed in connection with the involved activation barriers and the thermodynamic equilibria of the shown isomers and related ionic species. The isomerization equilibria reflect the impact of the isomer structure on inter- and intramolecular interactions, revealing the differences in dissociation behavior of the isomers.

Isomerization Barriers. Additional interconnecting *cis*−*trans* isomerization pathways could originate from one of the various intermediates shown in Figure 1. Such isomerizations around N−N bonds with more or less double bond character have been discussed to take place in quite similar reaction sequences of hydroxylamine oxidation in nitric acid[32] and decomposition of *trans*-hyponitrous acid.[33] Transition state optimizations and relaxed potential energy scans along the ONNO-dihedral angle have been performed. Calculated equilibria and reaction barriers of the relevant transient species are shown in Table 2. Related deprotonated species are included in the table as well. They become important for the acid-basis scheme discussed in the next section. In some cases (labeled "n.a." in Table 2), bond dissociation was found to be energetically more favorable than isomerization, and hence, no transition state is specified.

All isomerization steps, except HON(H)NO (**9**) → **8**, with a barrier of ΔE_{soln} = 78 kJ/mol, exhibit energy barriers of at least 172 kJ/mol and are, thus, too high to be accessible at room temperature conditions. Moreover, the free enthalpies of reaction clearly point out that the thermodynamics are in favor of the *cis* species. The only exception is the dianion (**6**, **11**), which is slightly more stable in its *trans* form.

Thermodynamic Stability. As already discussed for ON(H)N(H)O (**3**), the electrostatic interaction of the solvent favors the molecules with higher dipole moments. For the N-protonated anion (**5**) and the dianion (**11**), solvation effects shift the thermodynamic equilibrium toward the *cis* isomers, as apparent from the large differences of the free enthalpy of solvation, $\Delta(\Delta G^*_{solv})$. On the contrary, for the O-protonated species with $\Delta(\Delta G^*_{solv}) > 0$, the origin of the isomeric preference changes. Here, intramolecular hydrogen bonding leads to an additional

stabilization of the *cis* isomers in the case of **7**, **8**, and **12**. An exception is *cis*-hyponitrous acid (**13**), for which Zevallos et al.[34] pointed out that the higher thermodynamic stability is related to an electronic effect (favorable LP(N′) → σ^*(N−O) orbital interactions) rather than the weak intramolecular hydrogen bonding. The same interaction, even so less pronounced, is present in the case of the anion (**12**) and the dianion (**6**) and leads to a significant decrease of kinetic stability with respect to dissociation forming N_2O. Due to the increasing N−N bond length and decreasing LP(N′) → σ^*(N−O) overlap, this effect decreases in the order *cis*-hyponitrous acid (**13**), *cis*-hyponitrite monoanion (**12**), and *cis*-hyponitrite dianion (**6**).

The very high stability of the single ionic species *cis*-HONNO$^-$ (**12**) in comparison with that of its *trans* isomer (**15**) turns out to play a key role in the following acid−base equilibria and requires a more detailed discussion. The electrostatic potential of the optimized cyclic structure of **12** (see Figure 2) suggests contributions of intramolecular hydrogen bonding to the stabilization of the cyclic *cis* isomer. Indeed, although better stabilized in solution, the alternative *cis* conformer with an exocyclic hydrogen atom is calculated to be 22.6 kJ/mol more endergonic. In addition to this, the intramolecular proton transfer can be considered to be very fast due to a low free energy of activation in solution of merely 6.4 kJ/mol. The corresponding symmetric structure of the transition state is shown in Figure 2. An important aspect of the illustrated structures is the unusually short distance between the oxygen atoms, often used for classifying hydrogen bonds.[35] The calculated short distances between the oxygen atoms in the anion, 2.41 Å, and in the transition state, 2.26 Å, as well as the equivalent donor−acceptor capabilities and the favorable geometry formally meet the criteria of a so-called low-barrier hydrogen bond (LBHB). Often closely linked to these structures is an increasing difference of the acid-dissociation constants ΔpK_a as known from the acid−base chemistry of maleic acid. A similar influence on the protonation equilibrium of *cis*-hyponitrous acid is expected and will be discussed in more detail below.

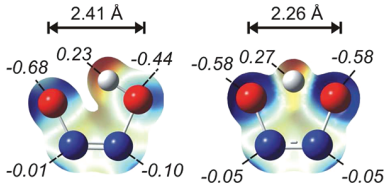

Figure 2. Optimized structures of the *cis*-hyponitrite anion (left) and the transition state (right) corresponding to the intramolecular hydrogen transfer. Highlighted are the electrostatic potentials color coded, the partial charges (in italic letters), and the unusually short O−O distance in the transition state.

To summarize the findings of this section, on the one hand, isomerizations are unlikely to play a role for the overall reaction scheme leading to N_2O formation from HNO dimerization. On the other hand, ionic species show remarkable stabilization effects in solution and therefore could play a so-far overlooked major role.

3.4. Acid−Base Equilibrium Scheme. Stimulated by the results of the preceding section and similar to an approach presented by Dutton et al.[36] for Angeli's salt decomposition, an acid−base equilibrium based reaction scheme for N_2O formation from HNO dimerization has been worked out. Including the ionic species in the reaction mechanism in solution is based on the assumption that acid−base equilibration of the relevant species is fast. The new scheme for the HNO dimerization is shown in Figure 3. The numbers in parentheses refer to calculated pK and pK_a values, and the latter are summarized again in Table 3.

Acid−Base Equilibria. In aqueous solution, for both the *cis* and *trans* pathways, rapid deprotonation of the initial dimer species (**2**, **3**) leads to the formation of the N-protonated ions (**4**, **5**). In the next step, under moderately *acidic* conditions, O-protonation is more favorable than a second deprotonation. Regarding the

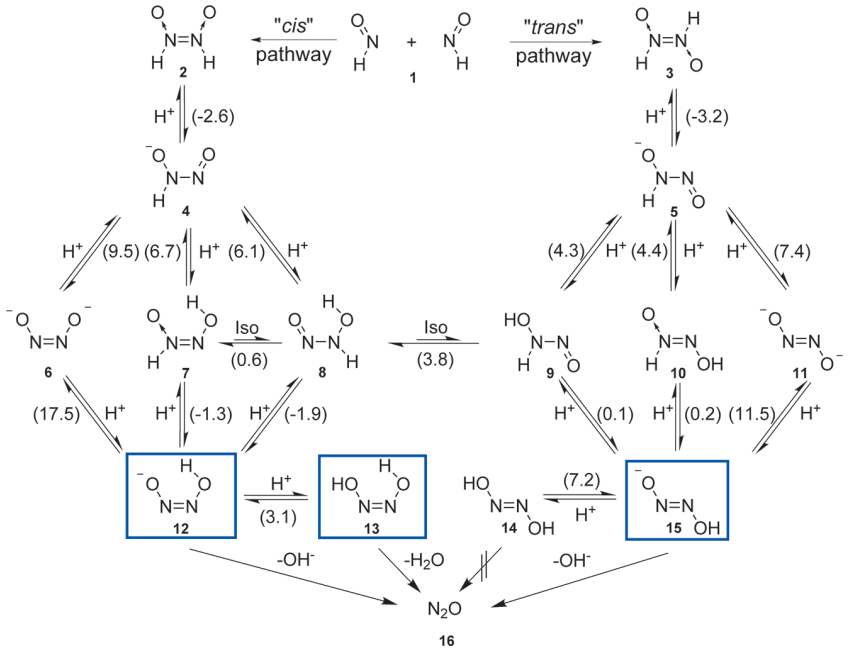

Figure 3. Acid−base equilibria model for the HNO dimerization reaction. The numbers in parentheses represent pK_a values as determined from eq 3 and pK values in the case of isomerization reactions. The species marked with frames are unstable with respect to decomposition yielding nitrous oxide.

Table 3. Theoretically Calculated Free Enthalpies of Reaction ΔG^*_{soln} in Solution (in kJ/mol, T = 298 K) and pK_a Values, Both Referenced to the Stated Acid−Base Equilibria HRef1 and HRef2

equilibrium				IEFPCM(UFF)		CPCM(UFF)	
acid		base		ΔG^*_{soln}	pK_a	ΔG^*_{soln}	pK_a
cis-ON(H)N(H)O	**2**	*cis*-ON(H)NO$^-$	**4**	−56.4	−2.6	−56.7	−2.7
cis-HON(H)NO	**8**	*cis*-ON(H)NO$^-$	**4**	−6.5	6.1	−7.1	5.9
cis-HON(H)NO	**8**	*cis*-HONNO$^-$	**12**	−52.1	−1.9	−52.4	−1.9
cis-HONN(O)H	**7**	*cis*-ON(H)NO$^-$	**4**	−3.0	6.7	−3.4	6.6
cis-HONN(O)H	**7**	*cis*-HONNO$^-$	**12**	−48.6	−1.3	−48.7	−1.3
cis-HONNOH	**13**	*cis*-HONNO$^-$	**12**	−23.4	3.1	−23.6	3.1
trans-ON(H)N(H)O	**3**	*trans*-ON(H)NO$^-$	**5**	−59.7	−3.2	−59.9	−3.3
trans-HON(H)NO	**9**	*trans*-ON(H)NO$^-$	**5**	−16.7	4.3	−16.4	4.3
trans-HON(H)NO	**9**	*trans*-HONNO$^-$	**15**	−40.7	0.1	−40.5	0.1
trans-HONN(O)H	**10**	*trans*-ON(H)NO$^-$	**5**	−16.3	4.4	−16.9	4.2
trans-HONN(O)H	**10**	*trans*-HONNO$^-$	**15**	−40.3	0.2	−40.9	0.1
trans-HONNOH (HRef 1)	**14**	*trans*-HONNO$^-$	**15**	0.0	7.2	0.0	7.2
cis-ON(H)NO$^-$	**4**	*cis*-ONNO^{2-}	**6**	−11.5	9.5	−9.4	9.9
cis-HONNO$^-$	**12**	*cis*-ONNO^{2-}	**6**	34.2	17.5	35.9	17.8
trans-ON(H)NO$^-$	**5**	*trans*-ONNO^{2-}	**11**	−24.0	7.4	−24.0	7.4
trans-HONNO$^-$ (HRef 2)	**15**	*trans*-ONNO^{2-}	**11**	0.0	11.5	0.0	11.5

two possible sites for O-protonation, for *trans*, both intermediates (**9**, **10**) are equally feasible, whereas *cis*-HONN(O)H (**7**) is energetically more favorable than *cis*-HON(H)NO (**8**). In addition, a fast intramolecular hydrogen transfer between the oxygen atoms is possible, resulting in equilibration of the *cis* species (**7** and **8**). A further deprotonation step yields the single protonated hyponitrite (**12**, **15**). Similarly, under moderate *alkaline* conditions, the formation of singly protonated hyponitrite (**12**, **15**) is predicted to proceed through **6** and **11** via sequential deprotonation and protonation. Whereas the *trans*-hyponitrite anion (**15**) will be easily protonated under acidic conditions, single protonated *cis*-hyponitrite (**12**) is the dominant species down to a pH of 3.1 and, due to a high p$K_{a,2}$ value of 17.5, is stable under alkaline conditions with respect to deprotonation as well. Both *cis* species (**12**, **13**) and the *trans*-hyponitrite anion (**15**) are considered to be unstable and decompose to form the final product N_2O with relatively low activation barriers of 42, 73, and 84 kJ/mol, respectively. These calculated barriers are in accordance with the literature values for the *cis* isomers but are somewhat lower than the experimental value of 98 kJ/mol reported for the *trans* isomer decomposition.[30,37,38] Note that *trans*-hyponitrous acid (**14**) is fairly stable in solution due to the absence of a feasible intramolecular elimination channel. In summary, under acidic conditions the following reaction sequences are possible:

$$trans-\mathrm{ON(H)N(H)O}\ (\mathbf{3}) \rightleftharpoons \mathbf{5} \rightleftharpoons \mathbf{9} \rightleftharpoons \mathbf{15} \rightleftharpoons trans-\mathrm{HONNOH}\ (\mathbf{14}) \quad (12)$$

$$\rightleftharpoons \mathbf{5} \rightleftharpoons \mathbf{9} \rightleftharpoons \mathbf{15} \rightarrow \mathrm{N_2O + H_2O}\ (\mathbf{16}) \quad (13)$$

$$\rightleftharpoons \mathbf{5} \rightleftharpoons \mathbf{9} \rightleftharpoons \mathbf{8} \rightleftharpoons \mathbf{12} \rightarrow \mathrm{N_2O + H_2O}\ (\mathbf{16}) \quad (14)$$

$$cis-\mathrm{ON(H)N(H)O}\ (\mathbf{2}) \rightleftharpoons \mathbf{4} \rightleftharpoons \mathbf{7} \rightleftharpoons \mathbf{12} \rightarrow \mathrm{N_2O + H_2O}\ (\mathbf{16}) \quad (15)$$

$$\rightleftharpoons \mathbf{4} \rightleftharpoons \mathbf{7} \rightleftharpoons \mathbf{12} \rightleftharpoons \mathbf{13} \rightarrow \mathrm{N_2O + H_2O}\ (\mathbf{16}) \quad (16)$$

Hence, the formation of N_2O is attributed to the species *cis*-HONNO$^-$ (**12**), *cis*-HONNOH (**13**), and *trans*-HONNO$^-$ (**15**). Due to lower activation barriers and in agreement with the already mentioned destabilizing orbital interactions (see section 3.3), the *cis* species are kinetically more unstable than the *trans*-hyponitrite anion. Decomposition of the *trans* species, in agreement with experiments, is rather slow.

cis and trans Pathways. As in the intramolecular reaction scheme, the *cis* and the *trans* pathway are well isolated. The only possible isomerization that might compete with the fast acid−base equilibria takes place between **8** and **9**. This equilibrium is in favor of the *cis* isomer and, therefore, could enable another pathway toward *cis*-hyponitrite. However, deprotonation of **9** and **10** can be estimated to proceed with a rate constant on the order of 10^{10} s^{-1} (as derived from the pK_a value by assuming a diffusion controlled protonation reaction). This is several orders of magnitude higher than a rough estimate of the isomerization reaction rate constant on the order of 1 s^{-1}, which is based on the free enthalpy of activation given in Table 2. Therefore, it appears unlikely that isomerization contributes significantly, and two well-separated *cis* and *trans* pathways can be assumed. Keeping in mind the strongly favored initial *cis* dimer formation (section 3.1), it becomes clear that the overall reaction is dominated by the *cis* pathway.

On the *cis* pathway, formation of the *cis*-hyponitrite anion (**12**) can be assumed to be rapid. Taking into account the high thermodynamic stability (due to the strong intramolecular hydrogen bonding, section 3.3) and the kinetic destabilization (due to the population of the σ^*(N−O) orbitals, section 3.3), decomposition of the *cis*-hyponitrite anion (**12**) will be preferred over the protonation equilibrium between **12** and **13** and subsequent decomposition of *cis*-hyponitrous acid (**13**). Therefore, N_2O formation from **12** dominates over almost the entire pH range and contributions of the molecular *cis*-hyponitrous acid pathway only become significant at very low pH values.

For the minor *trans* pathway, the model predicts the formation of the moderately stable *trans*-HONNOH (**14**) in the acidic range around pH = 0. With increasing pH, the equilibration with the monoanion (**15**) becomes significant and a slow decomposition sets in. At higher pH, the equilibrium is moved to the side of the

stable dianion and the decomposition rate decreases again. Thus, the rate of the *trans*-decomposition is predicted to be slow and strongly pH dependent following the bell-shaped curve found experimentally by Buchholz and Powell.[38]

In summary, we conclude that the major pathway of nitrous oxide formation from HNO dimerization follows a sequence of rapid heterolytic bond cleavages according to eq 15, which is completed with the decomposition of the *cis*-hyponitrite anion (**12**) to form N_2O.

3.5. Assessment of the Acid−Base Equilibrium Model. The acid−base equilibrium model, in contrast to the formerly discussed intramolecular model, provides a theoretically sound framework for the formation of N_2O from HNO dimerization and *trans*-$HONNO^-$ decomposition. As a further check of its consistency, the model must be capable of explaining previous experimental results. In the following, with a focus on the equilibrium of the intermediate *cis*-hyponitrous acid, (i) experimental results of the HNO dimerization reaction at varying pH values taken from the literature and (ii) spectroscopic measurements concerning the formation of OH radicals are compared with model predictions. Finally, the role of NO^- for dimerization in highly alkaline solutions and the reason for the distinct differences between the acid−base characteristics of the *cis* and *trans* isomers will be addressed.

HNO Dimerization Experiments. Several experimental studies with reactions taking place under acidic, neutral, and moderate alkaline conditions are reported that include HNO dimerization to explain N_2O formation.[1,17,39] In the following, the outcomes of three selected studies performed in different pH ranges are analyzed with respect to the applicability of the acid−base equilibrium model and to support the predicted *cis*-preference of the initial HNO dimerization step:

Under *acidic* conditions (pH = 1), according to Bell and Kelly,[17] selective reduction of sodium nitrite yields nitroxyl. Utilizing trimethylamine borane (TMAB) as hydride donor in water−dioxane (the latter preventing a possible radial chain reaction observed in this pH region[40]), the corresponding HNO forming reaction has been postulated to be

$$H_2NO_2^+ + H^-(\text{from TMAB}) \rightarrow HNO + H_2O \qquad (17)$$

Assuming the validity of our mechanism, under these strongly acidic conditions, HNO dimerization could take place through the pathways given by eqs 12, 15, and 16 with **12**, **13**, and **14** as the intermediate products. As outlined above, at pH = 1 both *cis* species **13** and **12** may contribute to nitrous oxide formation. In contrast, the formed *trans*-hyponitrous acid (**14**) was found to be stable[38] or possibly reacts with available nitrite to yield N_2.[40] In fact, Bell and Kelly reported fast and almost stoichiometric transformation of nitrite into nitrous oxide (1.92:1). From this it follows that only traces of **14** have been formed in the reaction, thus in agreement with our prediction of a preference for the *cis* pathway.

However, a chance of misinterpretation of the reaction sequence remains, because it cannot be completely ruled out that certain amounts of NO are formed from nitrous acid (HONO) disproportionation as byproduct as well. NO reacts rapidly with HNO, and the subsequent chain reaction of the product leads to the formation of *trans*-$N_2O_2H_2$ and NO (at low NO concentrations) or N_2O and nitrite (at high NO concentrations).[2] Such a NO mechanism would be indistinguishable from HNO dimerization.

In *weakly acidic, neutral,* and *moderately alkaline* solutions, thermal decompositions of the widely used HNO donors, Angeli's salt and Piloty's acid (*N*-hydroxybenzenesulfonamide), have been extensively studied.[1] In the second case, the redetermined $pK_a = 11.4$ of the $^1HNO/^3NO^-$ equilibrium sets an upper pH limit for dimerization of HNO due to competing deprotonation.[2] After protonation of Angeli's salt ($pK_a = 9.7$) and deprotonation of Piloty's acid ($pK_a = 9.3$), the decompositions of the two anions follow first-order kinetics with similar rate constants ($6.8 \times 10^{-4}\ s^{-1}$ and $4 \times 10^{-4}\ s^{-1}$)[18,41] over a wide pH range according to

$$ON(H)NO_2^- \rightleftharpoons NO_2^- + HNO \quad (pH = 4-8) \qquad (18)$$

$$PhSO_2NHO^- \rightleftharpoons PhSO_2^- + HNO \quad (pH > 11) \qquad (19)$$

On the basis of the presented acid−base scheme, consecutive reactions according to eqs 13 and 15 (via **6** and **11** under alkaline conditions) will lead to **12** and **15** as possible nitrous oxide producing species. The corresponding *cis* pathway includes the rapid decomposition of **12** and is consistent with the reported pH independent rate constants. In contrast to the *cis* isomer (**12**), which is the dominant species at $3.1 < pH < 17.5$, the *trans* isomer **15** equilibrates with the stable *trans*-species (**11**, **14**). According to the measurements of Buchholz and Powell, the effective decomposition rate constant of **15** decreases from its maximum value, $5 \times 10^{-4}\ s^{-1}$ at pH = 9, to $<1 \times 10^{-5}\ s^{-1}$ at pH = 4 and $3 \times 10^{-5}\ s^{-1}$ at pH = 12.[38] Thus, assuming the *trans* pathway to take place, intermediate *trans*-hyponitrite should accumulate under acidic or alkaline conditions to concentration levels that should have been detectable or should have affected the reported time-resolved UV absorption measurements. The UV spectra of *trans*-hyponitrous acid (**14**, **15**, **11**) exhibit absorption bands that are coincident with those of the reactants used for monitoring the kinetic experiment. Neither in the case of Angeli's salt[41] nor in the case of Piloty's acid[18,39] (at pH < 13) have changes of UV spectra or kinetics related to hyponitrite formation been reported, even though additional experiments designed for this purpose were performed by Seel and Bliefert.[39]

In conclusion, on the basis of kinetic and spectroscopic evidence, a reassessment of the results for all three HNO donor systems in the light of the new acid−base model reveals the absence or presence of very low amounts of *trans*-hyponitrous acid. Reaction sequences based on the *cis* dimer pathway, in agreement with our theoretical predictions, can explain the observed fast formation of nitrous oxide via final decomposition of **12** in all cases. Of course, due to the absence of possible isomerizations, these findings are also in line with the predicted initial preference of *cis* dimer formation.

Synthesis of the cis Isomers. Many early attempts of synthesizing the *cis* isomers of hyponitrous acid or its mere detection as intermediate have failed.[42] A first successful synthesis route yielding almost exclusively *cis*-hyponitrite salt was based on the reduction of NO using sodium in liquid ammonia.[43] This high selectivity with respect to the formation of the *cis* isomer is somewhat similar to the initial dimerization of HNO in water yielding preferentially the *cis*-HNO dimer. Feldmann and Jansen[44] presented another successful gas−solid phase synthesis of the *cis*-hyponitrite dianion (**6**) from N_2O and NaO. They were also able to report the first single crystal structure, which underlines the kinetic stability of *cis*-$N_2O_2^{2-}$ as a solid. However,

solvation attempts revealed that rapid decomposition of the sodium salt takes place in contact with protic solvents as well as carbon dioxide. Note that all these findings are in fact consistent with our prediction of a low acidity of the *cis* monoanion (**12**) ($pK_{a,2}$ = 17.5), which is in-between the acidities of water (15.7) and ammonia (34). Whereas *cis*-$N_2O_2^{2-}$ is stable in ammonia, fast decomposition of the single protonated species (**12**) in water gives an explanation for the former experimental problems of isolating the *cis* species in aqueous environments.

Formation of OH Radicals. It was further suggested[40] that *cis*-hyponitrous acid (**13**) is a source of OH radicals via an azo-like homolytic fission according to

$$HONNOH \rightarrow N_2 + 2OH \qquad (20)$$

Evidence for the OH radical formation has been presented in a series of EPR spin trapping studies performed by Stoyanovsky and co-workers,[6,16] and further verification of OH was found in the product yields from experiments using radical scavengers. In these studies, a pH dependent decomposition of Angeli's salt showed a maximum of OH radical formation around pH = 4. Whereas O-protonation has been shown to lead to NO formation from Angeli's salt instead of HNO at lower pH values,[36] the decrease of OH yield toward higher pH was explained by a shift of a postulated equilibrium between **13** and **8**, followed by decomposition of **8** to form nitrous oxide. Objecting to this interpretation, we find no convincing evidence for such an equilibrium. It is calculated to be thermodynamically unfavorable (pK = 5) and is definitively not pH dependent (see Figure 3). A more reasonable explanation of the results of Stoyanovsky and co-workers is the acid–base equilibrium of *cis*-hyponitrous acid (**13**), which may partly undergo homolytic fission yielding OH, and the single protonated species (**12**), which rapidly decomposes to form N_2O. The predicted pK_a value of the *cis*-hyponitrous acid equilibrium (pK_a = 3.1) fits the observed pH dependence found in the OH scavenging studies[6,16] as well as the occurrence of enhanced DNA strand breakages[5] at pH < 6 quite well.

Whereas the decomposition of the anion can easily be explained by rapid N–O bond breakage, forming N_2O and OH^-, the evaluation of the kinetic stability and the fate of the molecular *cis*-hyponitrous acid (**13**) remains difficult. Due to the significantly higher activation barrier, the intramolecular hydrogen transfer and the subsequent decomposition can be assumed to be much slower than the decomposition of the anion. Hence, the proposed azo-like homolytic fission, according to eq 20, may in fact become important. Even small amounts of generated OH radicals may serve as carriers of a chain reaction cycle forming N_2O. Note, however, that a decomposition step yielding OH most likely starts from the less stable exocyclic conformer of **13**. Therefore, it is difficult to assess the significance of such a radical process with respect to the overall N_2O formation. Furthermore, little is known about a possible O-protonation of the molecular acid (**13**) via intermolecular hydrogen transfer. Such an acid-catalyzed decomposition mechanism, which is reported[42] to be important for the isomeric *trans*-hyponitrous acid (**14**) below pH = 0, can be assumed to become relevant for the decomposition of *cis*-hyponitrous acid at low pH as well.

Dimerization in Highly Alkaline Solution. Another open question that arises from the experiments utilizing Piloty's acid is the influence of the acid–base equilibrium of HNO/NO^- on the overall dimerization process. In highly alkaline solutions, slow deprotonation of the ground state singlet ^1HNO is considered to yield the spin-forbidden triplet ground state base $^3NO^-$ rather than the spin-allowed energetically unfavorable $^1NO^-$.[2] Compared to ^1HNO, $^3NO^-$ is known to react rapidly with oxygen and nitric oxide. In this spirit, the spin-forbidden reaction of $^3NO^-$ with ^1HNO appears unlikely to be rapid in solution. However, in a recent kinetic study on photoinduced release of nitroxyl from Angeli's salt, Lymar and Shafirovich[45] came to the conclusion that this reaction might be fast as well. Attributing an unidentified $^3NO^-$ loss process exclusively to the reaction $^1HNO + {}^3NO^-$, an upper limit for the rate constant (6.6×10^9 M^{-1} s^{-1}) was reported. Moreover, at exceedingly high alkalinity, the spin-allowed dimerization of $^3NO^-$ may become significant as well, but detailed kinetic studies regarding this reaction are not available.

Following similar arguments as put forward for the kinetics of the dimerization of ^1HNO in section 3.1 it is clear that due to the different dipole moment and especially the additional charge of $^3NO^-$, quite different transition states can be expected for these reactions. Consideration of the calculated *cis*–*trans* equilibria of the possible products as given in Table 2 reveals that in the case of the reaction $^1HNO + {}^3NO^-$ a similar *cis* preference is obtained for $ON(H)NO^-$ (**4**, **5**). On the contrary, in the case of the $^3NO^-$ dimerization the *trans*-$N_2O_2^{2-}$ isomer (**11**) is calculated to be slightly more stable than the *cis*-$N_2O_2^{2-}$ isomer (**6**). Thus, it may be speculated that the isomer ratio is changed in favor of the *trans* isomer in the latter case. Indeed, evidence for the *trans*-hyponitrite dianion as a reaction product has been found in Piloty's acid decomposition experiments performed above pH > 13,[18,39] but this has previously been explained to result from a possible isomerization under alkaline conditions.[39] For sure, more experimental and theoretical studies are needed to clarify the dominant dimerization reaction in the case of the simultaneous presence of ^1HNO and $^3NO^-$.

Origin of ΔpK_a Differences. Finally, the predicted quite drastic difference between the $\Delta pK_a = pK_{a,2} - pK_{a,1}$ values of the *cis* and *trans* isomers calls for a more detailed explanation. As presented in the acid–base scheme in Figure 3, for *trans*-hyponitrous acid (**14**, **15**, **11**) ΔpK_a = 4.3 and for *cis*-hyponitrous acid (**13**,**12**,**6**) ΔpK_a = 14.4. The difference is much more pronounced than in the prominent example of maleic acid and fumaric acid, with corresponding values of ΔpK_a = 4.2 and 1.4, respectively. Following Perrin's recent discussion,[46] large ΔpK_a values do not only originate from the energetic stabilization resulting from intramolecular hydrogen bonding but are also an effect of preventing electrostatic "strain" arising from the proximity of the charged heteroatoms in the dianion. Whereas in most organic molecules certain structural adaptions can reduce this effect, in the case of the *cis*-hyponitrite dianion (**6**) the partial double bond character of the N–N bond leads to a fixation of the unfavorable structure. Thus, an evasion into a nonplanar structure as well as a further increase of the N–N distance are energetically demanding. The first protonation will therefore not only enable formation of an energetically favorable hydrogen bond but also remove the electrostatic destabilization and enable relaxation of the "strained" structure. The corresponding high proton affinity of the dianion is in accordance with a pronounced shift of the $pK_{a,2}$ toward a higher value.

The second protonation results in the uncharged *cis*-hyponitrous acid (**13**), which shows no pronounced hydrogen bonding, as evident from the low energy differences of the corresponding *cis*-conformers calculated already by Zevallos et al.[34] for the gas

phase species. This pronounced difference of the intramolecular hydrogen bonding energy compared to the monoanion (**12**) gives an explanation for the shift of the $pK_{a,1}$ toward a lower value.

Taking together the effect of electrostatic "strain" and hydrogen bonding, this gives an explanation of the unique ΔpK_a difference between the *cis* and the *trans* isomers.

4. CONCLUSION

Two different DFT based models for N_2O formation from HNO dimerization were analyzed regarding their potential to explain the quite complex experimental results for N_2O formation in solution. In contrast to the previously recommended intramolecular rearrangement scheme, a fast acid−base equilibria based mechanism is in agreement with experimental findings. According to our mechanism, N_2O formation is dominated by initial formation of the *cis*-HNO dimer, followed by rapid proton transfer reactions and finally decomposition of the *cis*-hyponitrite anion. A minor formation (if any) of the *trans*-HNO dimer leads to the formation of *trans*-hyponitrous acid, which slowly decays via the corresponding anion. Theoretically calculated pK_a values revealed an enhanced stability of the *cis*-hyponitrite anion due to the formation of an intramolecular hydrogen bond and a strictly deviating acid−base chemistry of the *cis* and the *trans* isomers. Under physiological conditions, the decomposition of the *cis*-hyponitrite anion should dominate the formation of nitrous oxide, whereas at low pH (<4) various decomposition mechanisms of the uncharged species may become relevant. Specifically designed experiments are needed to further test our new mechanism. Currently, experiments on isotope selective detection of N_2O are underway that help to differentiate between alternative reaction pathways.

■ ASSOCIATED CONTENT

Supporting Information. All calculated structures and energies. This material is available free of charge via the Internet at http://pubs.acs.org.

■ AUTHOR INFORMATION

Corresponding Author
fehling@phc.uni-kiel.de; friedrichs@phc.uni-kiel.de

■ ACKNOWLEDGMENT

The authors thank Douglas W. R. Wallace for encouraging us to take a closer look at N_2O formation mechanisms and two anonymous reviewers for their detailed comments. Financial support by the German Science Foundation (DFG-EC80) in the framework of the cluster of excellence "The Future Ocean" is gratefully acknowledged.

■ REFERENCES

(1) Miranda, K. M. *Coord. Chem. Rev.* **2005**, *249*, 433–455.
(2) Shafirovich, V.; Lymar, S. V. *Proc. Natl. Acad. Sci. U. S. A.* **2002**, *99*, 7340–7345.
(3) Bartberger, M. D.; Liu, W.; Ford, E.; Miranda, K. M.; Switzer, C.; Fukuto, J. M.; Farmer, P. J.; Wink, D. A.; Houk, K. N. *Proc. Natl. Acad. Sci. U. S. A.* **2002**, *99*, 10958–10963.
(4) Paolocci, N.; Jackson, M. I.; Lopez, B. E.; Miranda, K.; Tocchetti, C. G.; Wink, D. A.; Hobbs, A. J.; Fukuto, J. M. *Pharmacol. Ther.* **2007**, *113*, 442–458.
(5) Ohshima, H.; Gilibert, I.; Bianchini, F. *Free Radical Biol. Med.* **1999**, *26*, 1305–1313.
(6) Ivanova, J.; Salama, G.; Clancy, R. M.; Schor, N. F.; Nylander, K. D.; Stoyanovsky, D. A. *J. Biol. Chem.* **2003**, *278*, 42761–42768.
(7) Sulc, F.; Farmer, P. J. *The smallest biomolecules: diatomics and their interactions with heme proteins*; Elsevier Science: 2008; pp 429−462.
(8) Kohout, F. C.; Lampe, F. W. *J. Am. Chem. Soc.* **1965**, *87*, 5795–5796.
(9) Smith, P. A. S.; Hein, G. E. *J. Am. Chem. Soc.* **1960**, *82*, 5731–5740.
(10) Bazylinski, D. A.; Hollocher, T. C. *J. Am. Chem. Soc.* **1985**, *107*, 7982–7986.
(11) Akhtar, M. J.; Balschi, J. A.; Bonner, F. T. *Inorg. Chem.* **1982**, *21*, 2216–2218.
(12) Lin, M. C.; He, Y.; Melius, C. F. *Int. J. Chem. Kinet.* **1992**, *24*, 489–516.
(13) Bryukov, M.; Kachanov, A.; Timonnen, R.; Seetula, J.; Vandoren, J.; Sarkisov, O. *Chem. Phys. Lett.* **1993**, *208*, 392–398.
(14) Ruud, K.; Helgaker, T.; Uggerud, E. *J. Mol. Struct.* **1997**, *393*, 59–71.
(15) Lüttke, W.; Skancke, P. N.; Traetteberg, M. *Theor. Chem. Acc.* **1994**, *87*, 321–333.
(16) Stoyanovsky, D. A.; Clancy, R.; Cederbaum, A. I. *J. Am. Chem. Soc.* **1999**, *121*, 5093–5094.
(17) Bell, K. E.; Kelly, H. C. *Inorg. Chem.* **1996**, *35*, 7225–7228.
(18) Bonner, F. T.; Ko, Y. *Inorg. Chem.* **1992**, *31*, 2514–2519.
(19) Frisch, M. J.; et al. *Gaussian 09*, Revision A.02; Gaussian Inc.: Wallingford, CT, 2009.
(20) Dunning, T. H. *J. Chem. Phys.* **1989**, *90*, 1007–1023.
(21) Tomasi, J.; Mennucci, B.; Cammi, R. *Chem. Rev.* **2005**, *105*, 2999–3094.
(22) Ho, J.; Coote, M. L. *J. Chem. Theory Comput.* **2009**, *5*, 295–306.
(23) Bonner, F. T.; Hughes, M. N. *Comments Inorg. Chem.* **1988**, *7*, 215–234.
(24) Marenich, A. V.; Cramer, C. J.; Truhlar, D. G. *J. Phys. Chem. B* **2009**, *113*, 6378–6396.
(25) Glaser, R.; Murmann, R. K.; Barnes, C. L. *J. Org. Chem.* **1996**, *61*, 1047–1058.
(26) Peters, N. J. S. *J. Phys. Chem. A* **1998**, *102*, 7001–7005.
(27) Callear, A. B.; Carr, R. W. *J. Chem. Soc., Faraday Trans.* **1975**, *71*, 1603–1609.
(28) Connors, K. *Chemical kinetics: the study of reaction rates in solution*; Wiley-VCH: 1990.
(29) Kirkwood, J. G. *J. Chem. Phys.* **1934**, *2*, 351–361.
(30) Ashcraft, R. W.; Raman, S.; Green, W. H. *J. Phys. Chem. A* **2008**, *112*, 7577–7593.
(31) Raman, S.; Ashcraft, R. W.; Vial, M.; Klasky, M. L. *J. Phys. Chem. A* **2005**, *109*, 8526–8536.
(32) Hussain, M. A.; Stedman, G.; Hughes, M. N. *J. Chem. Soc. B* **1968**, 597–603.
(33) Loechler, E. L.; Schneider, A. M.; Schwartz, D. B.; Hollocher, T. C. *J. Am. Chem. Soc.* **1987**, *109*, 3076–3087.
(34) Zevallos, J.; Toro-Labbé, A.; Mó, O.; Yáñez, M. *Struct. Chem.* **2005**, *16*, 295–303.
(35) Musin, R. N.; Mariam, Y. H. *J. Phys. Org. Chem.* **2006**, *19*, 425–444.
(36) Dutton, A. S.; Fukuto, J. M.; Houk, K. N. *J. Am. Chem. Soc.* **2004**, *126*, 3795–3800.
(37) Hammerl, A. Hochenergetische, stickstoffreiche Verbindungen. Ph.D. Thesis, 2001.
(38) Buchholz, J. R.; Powell, R. E. *J. Am. Chem. Soc.* **1963**, *85*, 509–511.
(39) Seel, F.; Bliefert, C. *Z. Anorg. Allg. Chem.* **1972**, *394*, 187–196.
(40) Buchholz, J. R.; Powell, R. E. *J. Am. Chem. Soc.* **1965**, *87*, 2350–2353.

(41) Hughes, M. N.; Wimbledon, P. E. *J. Chem. Soc., Dalton Trans.* **1976**, 703–707.
(42) Hughes, M. N. *Q. Rev. Chem. Soc.* **1968**, *22*, 1–13.
(43) Goubeau, J.; Laitenberger, K. *Z. Anorg. Allg. Chem.* **1963**, *320*, 78–85.
(44) Feldmann, C.; Jansen, M. *Z. Anorg. Allg. Chem.* **1997**, *623*, 1803–1809.
(45) Lymar, S. V.; Shafirovich, V. *J. Phys. Chem. B* **2007**, *111*, 6861–6867.
(46) Perrin, C. L. *Acc. Chem. Res.* **2010**, *43*, 1550–1557.

4.5 ADDITIONAL INFORMATION

4.5.1 *Kinetic simulation of the acid-base mechanism*

The acid-base mechanism as outlined in the publication has been further analyzed and implemented in a kinetic simulation utilizing CHEMKIN software.[108]
Rate constants were approximated based on the following assumptions:

- The experimentally determined rate constant of the initial dimerization in solution has been dissected into *cis* dimer and *trans* dimer formation, using the approximation of the isomer ratio derived from the Kirkwood model.
- In the case of acid-base equilibria, rate constants for deprotonation have been determined from calculated pK_a values under the assumption of a diffusion controlled back reaction ($k_r = 4 \times 10^{10}\,\mathrm{mol\,L^{-1}\,s^{-1}}$) using

$$k_f = \frac{k_r}{K_a}. \tag{4.12}$$

- For decomposition and isomerization reactions of the hyponitrite species a TST approach excluding tunneling and non-idealities of the solvent has been used to derive suitable rate constants according to

$$k = \frac{k_b T}{h} \exp\left(\frac{-\Delta G^{\ddagger}_{\mathrm{soln}}}{RT}\right). \tag{4.13}$$

The implemented reaction scheme included next to the reactions according to Figure 3 in the preceding publication, further hypothetical buffer reactions in order to set the pH to a fixed value and to treat the self-dissociation of H_2O. Used reaction rate constants are listed in Table 4.1. Here, it should be mentioned that only reactions with H^+ and not OH^- are considered and therefore the implemented scheme is valid under acidic but not fully applicable under alkaline conditions. As starting parameters, an initial HNO concentration of 0.55 mM was assumed for all simulations. Due to the fact that the rate constant of the *cis*-isomer has been suggested to be several orders of magnitude higher than the *trans* isomer, each pathway has been studied separately in order to avoid numerical instability. The numerically simulated concentration-time profiles of selected species are illustrated in Figure 4.1 for different pH values.
First of all, the simulation is consistent with the conclusion of two separated reaction pathways for the two isomers that finally decompose to form nitrous oxide, i.e., *cis-trans* isomerizations in particular those of HON(H)NO do not compete with acid base equilibration on both pathways. Thus, the drawn conclusion that the initial isomer ratio determines the product ratio is confirmed.
On the *cis* pathway, basically no intermediate formation can be observed due to the fast decomposition of the *cis*-hyponitrite anion. A more detailed analysis revealed that, despite the pK_a of 3.1 for the *cis*-hyponitrous acid equilibrium, nitrous oxide is produced between $1 < \mathrm{pH} < 11$ more or less exclusively from the *cis*-hyponitrite anion and not from molecular *cis*-hyponitrous acid. The nitrite reduction experiments at $\mathrm{pH} = 1$ alluded to in section 3.5 of the publication and presented in chapter 3 might

Table 4.1: Estimated rate constants used for the kinetic simulation of the HNO dimerization scheme presented in Figure 3 of the publication.

Reaction			Method[1]	Rate constant[2]
HNO + HNO	→	*cis*-ON(H)N(H)O	exp.	8×10^{6}
HNO + HNO	→	*trans*-ON(H)N(H)O	exp.	1×10^{4}
cis-ON(H)N(H)O	→	*cis*-ON(H)NO^{-} + H^{+}	diff.	3×10^{12}
cis-HON(H)NO	→	*cis*-ON(H)NO^{-} + H^{+}	diff.	8×10^{3}
cis-HON(H)NO	→	*cis*-HONNO^{-} + H^{+}	diff.	8×10^{11}
cis-HONN(O)H	→	*cis*-ON(H)NO^{-} + H^{+}	diff.	3×10^{4}
cis-HONN(O)H	→	*cis*-HONNO^{-} + H^{+}	diff.	3×10^{12}
cis-HONNOH	→	*cis*-HONNO^{-} + H^{+}	diff.	3×10^{7}
trans-ON(H)N(H)O	→	*trans*-ON(H)NO^{-} + H^{+}	diff.	2×10^{13}
trans-HON(H)NO	→	*trans*-ON(H)NO^{-} + H^{+}	diff.	2×10^{6}
trans-HON(H)NO	→	*trans*-HONNO^{-} + H^{+}	diff.	3×10^{10}
trans-HONN(O)H	→	*trans*-ON(H)NO^{-} + H^{+}	diff.	2×10^{6}
trans-HONN(O)H	→	*trans*-HONNO^{-} + H^{+}	diff.	3×10^{10}
trans-HONNOH	→	*trans*-HONNO^{-} + H^{+}	diff.	3×10^{3}
cis-ON(H)NO^{-}	→	*cis*-ONO^{2-} + H^{+}	diff.	1×10^{1}
cis-HONNO^{-}	→	*cis*-ONO^{2-} + H^{+}	diff.	1×10^{-7}
trans-ON(H)NO^{-}	→	*trans*-ONO^{2-} + H^{+}	diff.	2×10^{3}
trans-HONNO^{-}	→	*trans*-ONO^{2-} + H^{+}	diff.	1×10^{-1}
trans-HON(H)NO	→	*cis*-HON(H)NO	TST	1×10^{0}
trans-HONNO^{-}	→	N_2O + OH^{-}	TST	6×10^{-4}
cis-HONNO^{-}	→	N_2O + OH^{-}	TST	8×10^{6}
cis-HONNOH	→	N_2O + H_2O	TST	6×10^{-2}

[1] Method for rate constant estimation: exp.: experimental value, diff.: based on diffusion controlled reaction and equilibrium constant, TST: transition state theory

[2] Units for bimolecular and unimolecular reactions are $M^{-1}\,s^{-1}$ and s^{-1}.

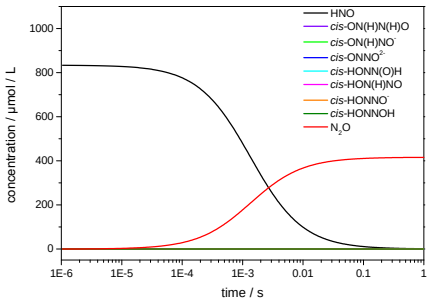

(a) *cis* pathway intermediates (pH = 1)

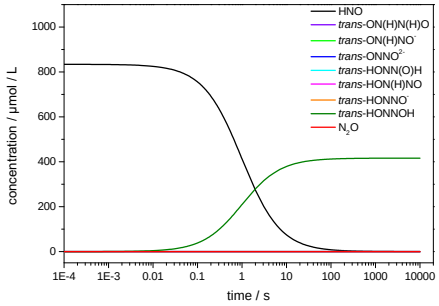

(b) *trans* pathway intermediates (pH = 1)

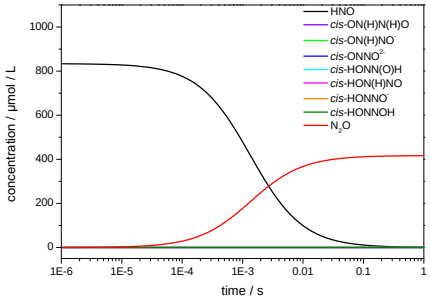

(c) *cis* pathway intermediates (pH = 3)

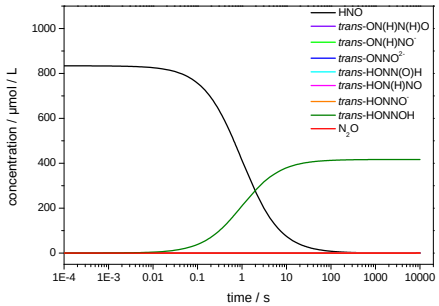

(d) *trans* pathway intermediates (pH = 3)

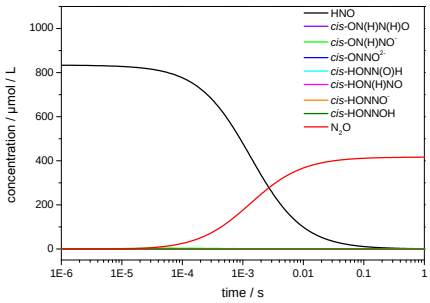

(e) *cis* pathway intermediates (pH = 6)

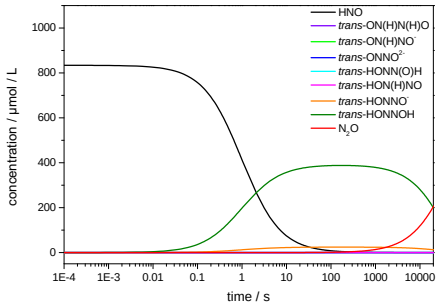

(f) *trans* pathway intermediates (pH = 6)

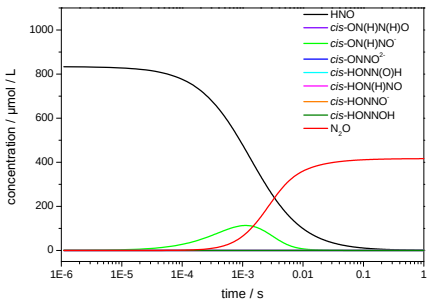

(g) *cis* pathway intermediates (pH = 8)

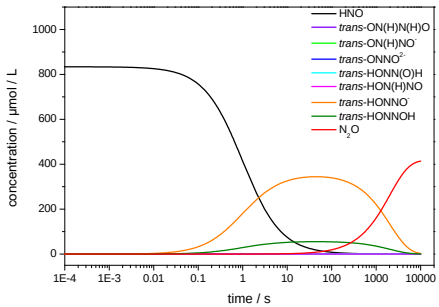

(h) *trans* pathway intermediates (pH = 8)

Figure 4.1: Kinetic modeling results of the HNO dimerization mechanism for the reaction pathways of the *cis* (left) and *trans* (right) isomer in different buffer solutions.

therefore also reflect the decomposition of the anion.
On the *trans* pathway, intermediate formation of *trans*-hyponitrous acid is predicted. It equilibrates at the corresponding pH with the decomposing anion. As expected, at higher pH the equilibrium shifts to the anion and the overall rate of N_2O formation increases significantly.
In summary, the kinetic simulation is fully consistent with the conclusions drawn in the publication. Absence of traceable intermediates points towards the outlined *cis* pathway including final decomposition of the *cis*-hyponitrite anion.

4.5.2 *Validation experiment for HNO dimerization products*

As outlined in section 3.5 of the publication, UV/Vis spectra of HNO donor decomposition experiments have been reported to yield no evidence for *trans*-hyponitrite formation.[90] In the light of the redetermined pK_a of nitroxyl and the suggested mechanism it appeared reasonable to check the validity of the previous measurements with an appropriate experiment aiming to detect the possible intermediate *trans*-hyponitrite. Therefore, the decomposition of Piloty's acid (N-hydroxy-benzenesulfonamide) in *alkaline* aqueous solution was analyzed at pH = 11 (below the pK_a of nitroxyl).
According to the literature,[109] the following reaction sequence is feasible:

$$PhSO_2NHOH \rightleftharpoons PhSO_2NHO^- + H^+ \tag{4.14}$$

$$PhSO_2NHO^- \rightleftharpoons PhSO_2^- + HNO \tag{4.15}$$

$$2 \times HNO \rightarrow N_2O + H_2O \tag{4.16}$$

At pH = 11, the acid base equilibrium Equation 4.14 ($pK_a = 9.3$) is almost completely shifted towards the anion and hence the maximum rate for HNO formation is achieved. Contrariwise, the acid-base equilibrium of possible *trans*-hyponitrous acid is partly shifted towards the stable dianion, $N_2O_2^{2-}$, and hence its decomposition rate is decreased. Fast formation of HNO and slow decomposition of *trans*-hyponitrous acid should provide for maximum intermediate concentrations of *trans*-hyponitrite.
For comparison, UV/Vis spectra of the unimolecular decomposition of synthesized *trans*-hyponitrite samples in aqueous solution at pH = 11 have been measured and are shown in Figure 4.2. The same measurements were performed at pH = 9 and pH = 10 and revealed a decrease of the extracted effective rate constants from 13 to $6 \times 10^{-4}\,s^{-1}$ with increasing pH reflecting the shift of the acid-base equilibrium towards the dianion. These values are slightly higher than those reported by Loechler *et al.*[110] possibly due to rate increase observed for catalysis of carbonate impurities.
UV/Vis spectra of the decomposition reaction of Piloty's acid are shown in Figure 4.3 and were analyzed at 3 different wavelengths ($\lambda_1 = 240\,nm$, $\lambda_2 = 250\,nm$, $\lambda_3 = 260\,nm$). Note that *trans*-hyponitrous acid exhibits an absorption band at 237 nm with an absorption coefficient approximately seven times higher than the absorption coefficient of $PhSO_2NHO^-$ at the same wavelength, and 20 times higher than that of $PhSO_2^-$.[109] Thus, traceable amounts of *trans*-hyponitrite should be observable. Since it can be assumed that the equilibrium of Equation 4.15 is rate determining, an analysis according to an overall first order reaction was performed. Using the Guggenheim[111] and Swinbourne[112] methods, the corresponding rate constants have been determined to coincide $k(\lambda_1) = 4.5 \times 10^{-4}\,s^{-1}$, $k(\lambda_2) = 4.5 \times 10^{-4}\,s^{-1}$, and $k(\lambda_3) = 4.5 \times 10^{-4}\,s^{-1}$.

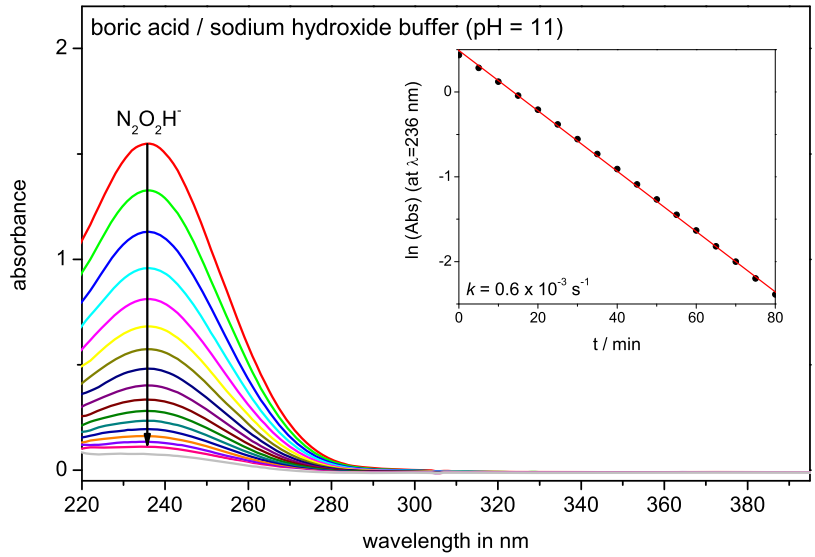

Figure 4.2: UV/Vis spectral changes of *trans*-hyponitrous acid in buffered aqueous solution (pH = 11).

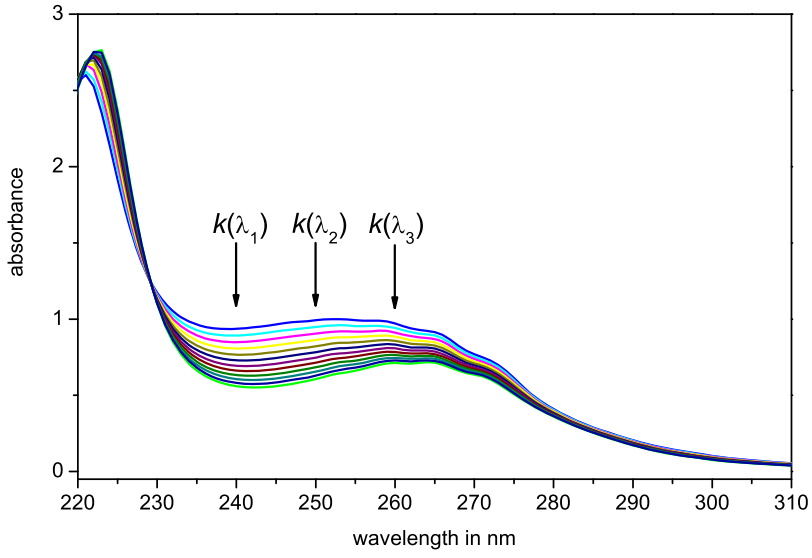

Figure 4.3: UV/Vis spectral changes of N-hydroxy-benzenesulfonamide (Piloty's acid) decomposition in buffered aqueous solution (pH = 11).

This absolute value of the rate constant is in good agreement with prior studies.[90,109] As anticipated above, the determined rate constant for $PhSO_2NHO^-$ decomposition is on the same order of magnitude as the subsequent decomposition reaction of *trans*-hyponitrite. Consequently, if *trans*-hyponitrite would be formed as a major product in the dimerization reaction, inconsistent *k* values would have been expected due to the superimposed *trans*-hyponitrite absorption at 237 nm. Therefore, the three identical rate constant values suggest that *trans*-hyponitrous acid absorption (if any) remains negligible - in agreement with our prediction of a predominant *cis*-pathway.

5

ISOTOPOMERIC SIGNATURE AND FORMATION MECHANISM OF N_2O

Theory guides. Experiment decides.

— Unknown Author

5.1 SCOPE OF THE PROJECT

As outlined in chapter 1, isotopomer preference in nitrous oxide formation has been used as a valuable tool to decipher sources, sinks and fluxes of this important greenhouse gas.[14] In order to apply site preference measurements for source characterization, numerous field and laboratory studies have been undertaken. The reported site preferences of nitrous oxide typically range from -20 up to +50‰, but due to calibration problems of the used mass spectrometric detection schemes the absolute accuracy of these values is partly questionable. Characteristic values have been reported for many biological sources, e.g., for denitrifying bacteria ($SP \approx$ -5‰),[19,21] denitrifying fungi ($SP \approx$ +37‰),[23] arachea ($SP \approx$ +30‰)[113] and nitrifying bacteria ($SP \approx$ +30‰).[22] In the latter case, it was recently argued by Frame and Cascanotti[82] that the corresponding value results from simultaneous nitrification ($SP \approx$ +36‰) and nitrifier-denitrification ($SP \approx$ -10‰). However, most of the studies dealt with site preference measurements focusing on the actual source characterization rather than discussing the molecular isotopomer formation mechanism. Due to lack of detailed understanding of the enzymatic catalysis mechanisms itself as outlined in chapter 1, site preference has often been interpreted as isotopic discrimination in binding kinetics of the involved iron center instead of an intrinsic isotope effect.
For the non-enzymatic reactions, such as the reaction of hydroxylamine with nitrous acid (Equation 1.10), early isotope tracer studies[56,114] showed approximately equimolar amounts of the two isotopomers formed - regardless of the isotope labeling of the educts. This experimental finding suggest the decomposition of a symmetric intermediate. According to the mechanism of Stedman and coworkers[36] this symmetric intermediate is *cis*-hyponitrous acid. Relying on precise IRMS measurements, Toyoda *et al.*[19] presented constant site preferences ($SP \approx$ +30‰) for hydroxylamine oxidation as well as nitrite reduction. Both are considered to include HNO dimerization (Equation 1.9). Already in an earlier publication, Toyoda *et al.*[18] pointed out that this site preference presumably is related to the formation of the symmetric intermediate $^{-}$ONNO^{-} followed by a heavy atom isotope effect in N-O-bond cleavage. By focusing on HONNOH as decomposing intermediate and based on the results of Morgenstern and Schown,[115] Schmidt *et al.*[43] pointed out that different vibrational frequencies must cause an isotope effect that affects the isotopomer ratio. Consequently, Toyoda's result of $SP \approx$ +30‰ is the commonly accepted value for chemical nitrous oxide formation. However, it should be noted that another study of an apparently abiotic mechanism showed a different value ($SP \approx$ 0‰) in presence of iron from dolerite rock.[116] In summary, it can be stated that the quite different

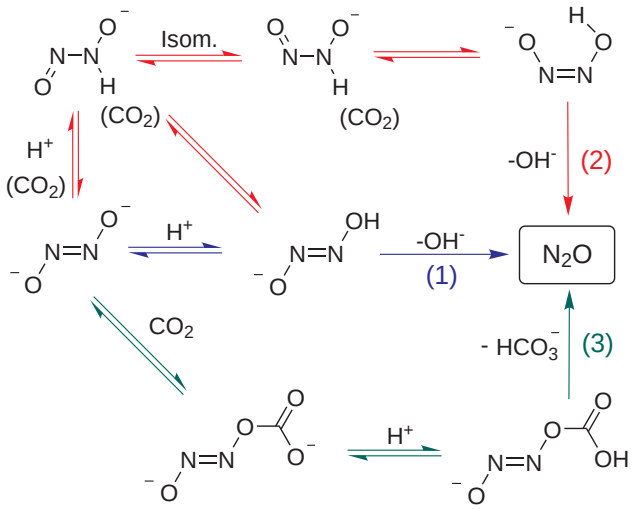

Figure 5.1: Scheme of the two suggested pathways of *trans*-hyponitrite decomposition. (1) Direct pathway (blue), (2) decomposition via isomerization (red) as suggested by Loechler *et al.*[110] for both, direct decomposition and CO_2 catalysis, and (3) alternative pathway for CO_2 catalysis (green).

site preference values observed for natural nitrous oxide sources have mainly been related to isotopic discrimination at the involved enzymatic iron centers affecting the decomposition of a symmetric species such as $^{-}ONNO^{-}$ or HONNOH.
Whereas for the discussed uncatalyzed reactions, (Equation 1.9 and Equation 1.10), all evidence points to the *cis*-isomer as a direct precursor for nitrous oxide, the isomer structure of the enzymatic intermediate has not yet been discussed in terms of isotopomer preference. Here, *cis*- as well as *trans*-hyponitrite structures have been suggested to be relevant. In several cases, it is still unclear whether N-O bond cleavage occurs at the active site of the enzyme or if it is the free species that decomposes.[28] Irrespective of that, arguments have been put forward by Spott *et al.*[42] underlining the existence of so-called codenitrification, a mechanism that combines enzymatic NO^{+} donor activation followed by uncatalyzed decomposition of the free intermediate species. The isomeric structure of this intermediate species has not been identified so far.
Although slow decomposition of the *trans* isomer has been observed as well, Loechler *et al.*[110] have questioned the existence of a direct *trans* isomer decomposition (see Figure 5.1, blue pathway, (1)). They postulated that the instability of the *trans*-hyponitrite monoanion follows from a slow proton transfer or direct N-protonation yielding $ON{-}NHO^{-}$ (red pathway, (2)). This would enable a *cis-trans* isomerization and a subsequent decomposition of the *cis* isomer. This suggestion was derived from the observation that *trans*-hyponitrite monoanion decomposition is catalyzed in presence of carbonyl compounds or carbon dioxide. Here, two alternative mechanisms have been discussed by the authors, (*i*) formation of an N-bonded adduct with hyponitrite enabling the isomerization (red pathway) or (*ii*) initial O-bonded adduct formation yielding an improved leaving group for subsequent decomposition (green pathway, (3)). The decision for the pathway assuming an initial N-bonded adduct was based on the fact that for the carbonyl compounds a linear free enthalpy relationship was inconsistent with the kinetics of the reaction. Consequently, an

analogous scheme for the spontaneous decomposition of the *trans*-hyponitrite anion was suggested. Although this conclusion has so far not been questioned in the literature, the extension of this mechanism to explain spontaneous decomposition as well as carbon dioxide catalysis remained unproven and speculative.

5.2 PROJECT OBJECTIVES

Despite the broad use of the site preference as valuable parameter for source characterization, so far, the mechanisms underlying the isotopomer ratio in nitrous oxide formation are only roughly understood. In the uncatalyzed chemical reaction, the previously assigned intermediates, $^{-}ONNO^{-}$ and HONNOH, leading to the formation of the two isotopomers, $^{15}N^{14}N^{16}O$ and $^{14}N^{15}N^{16}O$, are unlikely to be correct. The mechanism of HNO dimerization as derived in chapter 4 clearly points out that nitrous oxide formation should be dominated by the decomposition of the not yet considered *cis*-hyponitrite anion. Consequently, the corresponding reaction pathway should reproduce the isotopomer preference as determined by Toyoda *et al.*[19] and as it has been reconfirmed in this work in chapter 3. Beside further evidence for the consistency of the presented HNO dimerization mechanism, a deeper understanding of the related isotopomer formation mechanism is necessary to find correlations and deviations from this fundamental unbiased nitrous oxide formation process. This would also be interesting for establishing a still lacking N_2O isotopomer standard, which could be based on an easily reproducible and well-established chemical formation mechanism.
Strongly related to this issue is the so far ambiguous role of the *trans* isomer as it has been suggested[110] that the related decomposition mechanism follows a rate determining isomerization to the *cis* isomer. This would imply that site preference is identical no matter if the reaction involves *cis* or *trans* isomer. Contrariwise, the performed DFT calculations as presented in chapter 4 reveal that a direct decomposition of the *trans* isomer is feasible as well. The calculated barrier is basically consistent with the experimentally measured rate constant. If a direct decomposition pathway exist there should be a different isotopomer preference connected with this mechanism. This would contradict the common assumption of a characteristic signature of chemical N_2O formation. Finally, the *trans* structure is possibly relevant in biochemical formation mechanisms as *trans*-hyponitrite has been assigned to occur as intermediate in many related enzyme structures. As the catalytic effect of carbon dioxide in decomposition of *trans*-hyponitrite has been used as reference case for isomerization of *trans*-hyponitrite, an analysis of this catalysis effect with respect to the related isotopomer ratio should be insightful.
On these grounds, the isotopomer ratio of nitrous oxide from the decomposition of *trans*-hyponitrous acid will be investigated first in this chapter. By making use of calculated structures of both *cis*- and *trans*-hyponitrite, isotopomer preference are theoretically accessible. Once isotopomer effects of rate determining steps are known, a kinetic scheme of the feasible decomposition pathway allows for reproducing the overall isotopomer preference of the mechanism. Finally, a comparison of the theoretically derived site preference values with the results of various nitrous oxide sources will be drawn and possible parallels in the related mechanisms will be discussed.

5.3 THEORETICAL BACKGROUND

5.3.1 *Isotope effects on equilibria and reaction rates*

An important consequence of the Born-Oppenheimer separation (Equation 4.4) is that isotopic exchange does not change the electronic potential energy surface. It is therefore the difference in total energy, E_i, of the translational, rotational, and vibrational motion of the molecule that is responsible for most isotope effects.[6]

$$E_i = E_{\text{trans}} + E_{\text{rot}} + \sum_i E_{\text{vib}}(i) \tag{5.1}$$

The corresponding product of partition functions is given by

$$q = q_{\text{trans}} q_{\text{rot}} \prod_i q_{\text{vib}}(\nu_i). \tag{5.2}$$

For a typical isotope exchange reaction between A and B

$$\mathrm{A} + \mathrm{B}^* \rightleftharpoons \mathrm{A}^* + \mathrm{B} \tag{5.3}$$

it can be derived from statistical thermodynamics that the equilibrium constant depends on the ratio of the partition functions. According to Equation 5.2, the partition functions can be further dissected into the different contributions of nuclear motion, which can be calculated based on mass, M_i, moment of inertia, I_i, and the vibrational frequencies, $\tilde{\nu}_i$ of the molecule. If further the Teller-Redlich product rule is applied to exchange the moments of inertia with the corresponding expressions for the vibrational frequencies, the equilibrium constant and consequently the equilibrium isotope effect is given by the relation

$$K = \frac{q_{\mathrm{A}^*}/q_{\mathrm{A}}}{q_{\mathrm{B}^*}/q_{\mathrm{B}}} \tag{5.4}$$

$$= (SF)\frac{(s_2/s_1) f_{[A^*/A]}}{(s_2/s_1) f_{[B^*/B]}} = \mathrm{EIE} \tag{5.5}$$

in which (SF) is the symmetry number factor containing the symmetry numbers s_i and f is the reduced isotopic partition function as defined by Bigeleisen-Mayer.[117]

$$(s_2/s_1) f_{[2/1]} = \prod_i \frac{u_{2,i}}{u_{1,i}} \left(\frac{1 - \exp(-u_{1,i})}{1 - \exp(-u_{2,i})} \right) \exp\left((u_{1,i} - u_{2,i})/2\right) \tag{5.6}$$

$$= (\mathrm{PF})(\mathrm{EXC})(\mathrm{ZPE}) \tag{5.7}$$

with the abbreviation $u_i = hc\tilde{\nu}_i/kT$.
The three terms in Equation 5.7 contributing to the equilibrium isotope effect (EIE) are termed as product factor (PF), excitation factor (EXC), and zero point energy factor (ZPE). At high temperatures, (PF) and (EXC) cancel each other and (ZPE) converges to unity such that the net EIE becomes unity as well.
In order to quantify the effect of isotopic exchange on the rate constant, the transition state theory can be utilized to derive an expression in a similar manner.
Considering a simple chemical reaction such as

$$\mathrm{A} + \mathrm{B} \rightleftharpoons \mathrm{AB}^{\ddagger} \rightarrow \mathrm{P} \tag{5.8}$$

the ratio of the rate constants of the heavy and the light isotopologue of A is given by

$$\frac{k_1}{k_2} = \frac{K_1'^{\ddagger}}{K_2'^{\ddagger}} = \frac{q_{A^*}/q_A}{q'_{A^*B^{\ddagger}}/q'_{AB^{\ddagger}}} \tag{5.9}$$

with the equilibrium constants, $K_1'^{\ddagger}$ and $K_2'^{\ddagger}$, and partition functions, $q'_{A^*B^{\ddagger}}$ and $q'_{AB^{\ddagger}}$ of the heavy and light isotopologue in the transition state. As usual, the imaginary vibration corresponding to the reaction coordinate is excluded. Again, with $u_i = hc\tilde{\nu}_i/kT$ and by applying the Teller-Redlich product rule, an expression for the kinetic isotope effect (KIE) can be derived:

$$\begin{aligned} KIE = \frac{k_1}{k_2}(SF)^{-1} = \frac{\nu^{\ddagger}_{RC,1}}{\nu^{\ddagger}_{RC,2}} &\times \prod_i^{3N^{\ddagger}-7} \frac{u^{\ddagger}_{i,1}}{u^{\ddagger}_{i,2}} \prod_i^{3N-6} \frac{u_{i,2}}{u_{i,1}} \\ &\times \prod_i^{3N^{\ddagger}-7} \frac{1-\exp(-u^{\ddagger}_{i,2})}{1-\exp(-u^{\ddagger}_{i,1})} \prod_i^{3N-6} \frac{1-\exp(-u_{i,1})}{1-\exp(-u_{i,2})} \\ &\times \prod_i^{3N^{\ddagger}-7} \frac{\exp(u^{\ddagger}_{i,2}/2)}{\exp(u^{\ddagger}_{i,1}/2)} \prod_i^{3N-6} \frac{\exp(u_{i,1}/2)}{\exp(u_{i,2}/2)} \qquad (5.10) \\ = \frac{\nu^{\ddagger}_{RC,1}}{\nu^{\ddagger}_{RC,2}} &\times (\mathrm{PDT}) \times (\mathrm{EXC}) \times (\mathrm{ZPE}) \qquad (5.11) \end{aligned}$$

The KIE can be dissected into the product term (PDT), the excitation factor (EXC), the zero point energy factor (ZPE) and the ratio of the imaginary frequencies reflecting the reaction coordinate (RC). The latter term is the high temperature limit value, because all remaining terms cancel to give unity.

5.4 MATERIALS AND METHODS

5.4.1 *Computational methodology*

Quantum chemical calculations were performed utilizing the Gaussian 09 program suite.[118] If not stated otherwise, DFT calculations presented in this study were based on the B3LYP functional using Dunning's correlation consistent aug-cc-pVTZ basis set. Solvation was taken into account by application of the polarization continuum models, CPCM and IEFPCM, using the UFF cavities. After optimization, harmonic frequency analysis revealed minimum and transition state structures (zero and one negative frequency, respectively) and, by following the intrinsic reaction coordinate, TS structures were checked regarding their correct assignment to connect the respective minimum structures.

Kinetic and equilibrium ^{15}N-isotope effects were quantified by application of the Bigeleisen equation according to Equation 5.11. The required frequencies of the optimized educt and transition state structures were scaled by a factor of 0.9787 as suggested by Irikura *et al.*[119] The program ISOEFF08 from the Paneth group[120] was used for all calculations.

5.4.2 *Sample preparation*

5.4.2.1 *HNO dimerization: Acid-Catalyzed Amine-Borane Reduction of Nitrite*

$$H^{14}NO_2 + H^{15}NO_2 \xrightarrow[-(CH_3)_3N,\ B(OH)_3,\ H_2O]{(CH_3)_3N\cdot BH_3,\ H^+} H_2 + {}^{14,15}N_2O$$

Isotopomerically enriched $^{14,15}N_2O$ from nitroxyl dimerization was prepared by selective reduction of isotopically enriched sodium nitrite ($Na^{15}NO_2$, 98%, EURISOTOP; $Na^{14}NO_2$, 98%, Aldrich) using stoichiometric amounts of trimethylaminoborane (98%, Aldrich) in an acidic (pH = 0.7) 10% dioxane/water mixture as described by Bell and Kelly.[86] The produced gas was stripped from the reaction solution in a continuous helium flow. After passing a dry ice/isopropanol cooled trap to remove water, formed N_2O was condensed in a liq. nitrogen cooled trap for further use.

5.4.2.2 *Synthesis and decomposition of trans-hyponitrite*

$$Na^{14}NO_2 + Na^{15}NO_2 \xrightarrow[-4OH^-]{NaHg,+2H_2O} Na_2^{14,15}N_2O_2 + H_2O$$

Enriched single isotope labeled $Na_2^{14,15}N_2O_2$ was prepared as described by Addison *et al.*[121] Briefly, isotopically enriched sodium nitrite was reduced using sodium mercury alloy (10% Na, 99%, Aldrich) in a rapidly stirred isopropanol/dry ice cooled aqueous solution under a nitrogen inert gas atmosphere. After separating the formed mercury, the reaction solution was transfered into ice chilled ethanol and a fine precipitate was filtered after 4 h at 253 K. An alkaline solution (pH = 12) of the formed $Na_2^{14,15}N_2O_2$ showed a characteristic absorption band in the UV/VIS spectrum at $\lambda = 248$ nm. This band shifted towards $\lambda = 233$ nm upon neutralization and the absorption decayed with first order kinetics corresponding to an equilibrium shift towards *trans*-$HONNO^-$. In good agreement with Loechler *et al.*,[110] changes of pH and the use of carbonate buffers verified the reported dependencies of the rate induced by shifting protonation equilibria and buffer catalysis. The rate constants determined from first order decay of the absorption line at $\lambda = 233$ nm were comparable with the results given by Loechler *et al.*[110] and verified that the synthesized samples were basically free of carbonate impurities. Thus, the observed decomposition mechanism can essentially be attributed to the spontaneous decay of *trans*-$HONNO^-$.

$$Na_2N_2O_2 + H^+ \rightarrow N_2O + NaOH + Na^+$$

In order to generate N_2O from *trans*-$HONNO^-$ decomposition, isolated $Na_2^{14,15}N_2O_2$ was dissolved in a phosphate buffered solution (pH = 9) under a helium inert gas atmosphere and the formed nitrous oxide was stripped in a He flow and trapped as described above.

After synthesis, the gas samples were characterized by FTIR spectroscopy. Absorption bands at 1285, 2224 and 3480 cm^{-1} proved formation of nitrous oxide isotopomers in an expected binomial distribution depending on the used isotopic enrichment of initial nitrite. This is in accordance with the results of Bonner and Ravid.[122]

5.5 RESULTS AND DISCUSSION

In order to study a possible influence of the isomer structure on the site preference of the formed nitrous oxide, additional experiments using synthesized ^{15}N-isotope enriched *trans*-hyponitrite samples were designed. After decomposition, the isotopomer enriched samples were analyzed using the same method as outlined in chapter 3. The interpretation of the results was assisted by detailed DFT calculations of the decomposition mechanisms and then used to gain an understanding of the kinetics of HNO dimerization and *trans*-hyponitrite decomposition leading to the site preference of nitrous oxide.

5.5.1 *Site preference measurements of experimental trans-hyponitrite decomposition*

The efficient generation of isotopomer enriched samples of nitrous oxide from *trans*-hyponitrite requires the single ^{15}N-labeled isotopologue which is not commercially available. However, a well known and widely used synthesis route yielding *trans*-hyponitrite is the reduction of nitrite using sodium amalgam in alkaline solution. This synthesis enabled isotopologue enrichment by proper choice of isotope labeled nitrite, following the stoichiometry

$$\mathrm{Na}^{14}\mathrm{NO}_2 + \mathrm{Na}^{15}\mathrm{NO}_2 \xrightarrow[-4\mathrm{OH}]{\mathrm{NaHg},+2\mathrm{H}_2\mathrm{O}} \mathrm{Na}_2^{14,15}\mathrm{N}_2\mathrm{O}_2. \tag{5.12}$$

A drawback of this synthesis approach is the highly alkaline reaction environment, which requires inert gas atmosphere to prevent absorption of carbon dioxide as will be discussed below. The prepared samples of $Na_2N_2O_2$ were decomposed in aqueous buffered solution at a pH shifting the equilibrium towards the unstable $N_2O_2H^-$ yielding nitrous oxide. The latter was stripped from solution, isolated and then analyzed by CRD spectroscopy. A typically obtained CRD spectrum is shown in Figure 5.2 in comparison with a spectrum of a N_2O sample resulting from a HNO dimerization experiment. Matching the $^{14}N^{15}N^{16}O$ peaks and than scaling the $^{14}N^{15}N^{16}O$ profile using the same scaling factor reveals a significant change of the isotopomer ratio already by visual inspection.

Table 5.1: Experimental results for nitrous oxide isotopomer formation from *trans*-hyponitrite decomposition.

	Isotopic composition		Reaction conditions		
No.	R^S(Precurser)[1]	$R^P(N_2O)$[2]	pH	T / K	$\delta^{SP} \times 1000$
(I)	0.16	0.26	11	293	-15(17)
(II)	0.25	0.37	9	293	-10(19)
(III)	0.25	0.37	9	293	-18.3(34)
Avg.					-14(8)

[1] isotopic composition of the nitrite substrate, R^S.
[2] isotopic composition of formed nitrous oxide product, R^P, calculated from R^S

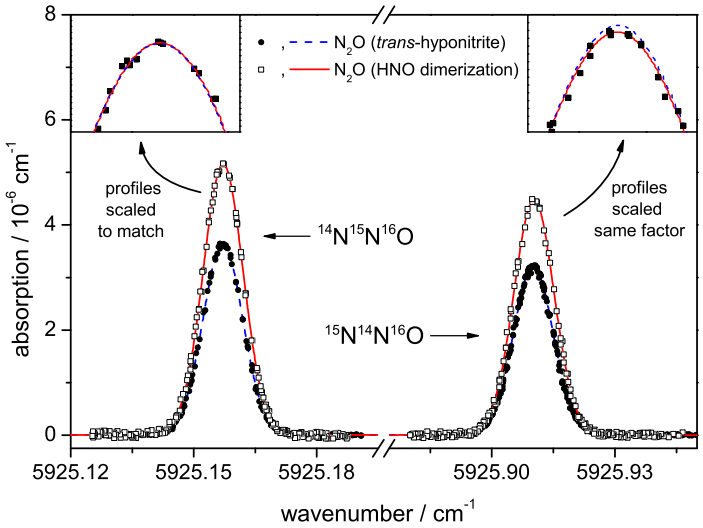

Figure 5.2: Cavity ringdown spectra of nitrous oxide samples from HNO dimerization and *trans*-hyponitrite decomposition. The two insets illustrate the difference of the isotopomer ratio by directly comparing the absorption of the two lines.

A corresponding analysis of the spectra using the methodology outlined in chapter 3 enabled determination of the site preference. The results of three different decomposition experiments are summarized in Table 5.1. Here, the large error margins of the stated site preference indicate statistical standard deviations, which are based on two concentration measurements each. Variations of the experimental parameters such as isotopic composition or pH value showed no significant change within the error limits and are therefore considered constant in analogy to the HNO dimerization experiments. Due to the higher statistical variation of the average value, the calculated overall error of the determined site preference connected with this reaction is significantly higher and has been determined to $\pm 15‰$.
The comparison of the obtained averaged value of $\delta^{SP} = -14 \pm 15‰$ with the results from HNO dimerization ($\delta^{SP} \approx +40 \pm 10‰$) underlines that the site preference is significantly different, i.e., in favor of the $^{15}N^{14}N^{16}O$ isotopomer. Judging from the design of the experiment (enriched isotopomer samples ($5\,nmol/cm^3$), no spectral interferences, identical setup) and the extent of the effect, it is unlikely that the difference of $\Delta\delta^{SP} = 54‰$ may arise from potential inaccuracies of the technique. Consequently, the measured isotopomer ratio of *trans*-hyponitrite supports the previous conclusion that HNO dimerization does not involve decomposition of the *trans*-hyponitrite anion (or only to a very minor extent). The other way around assigning the *cis*-hyponitrite anion as the N_2O forming species in HNO dimerization, the result suggests that *trans* decomposition takes place independently. This is consistent with the direct decomposition mechanism shown in blue color in Figure 5.1, but inconsistent with the assumption of an indirect decomposition via isomerization to the *cis* isomer as put forward by Loechler *et al.*[110] (red pathway in Figure 5.1).

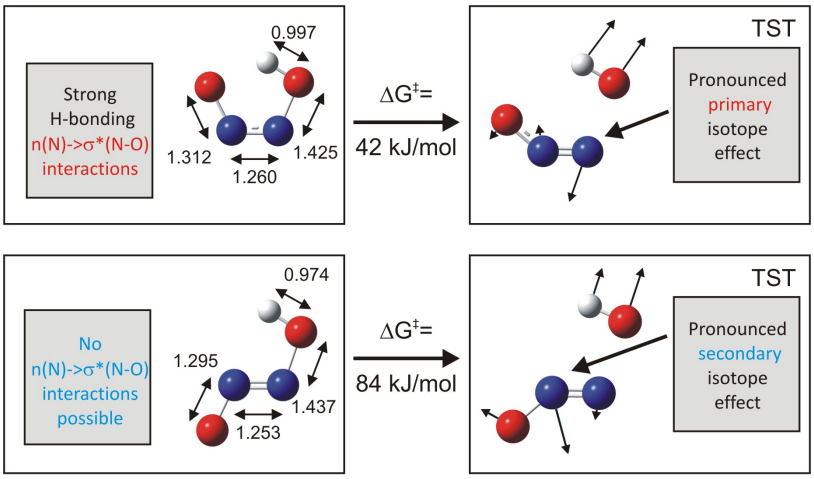

Figure 5.3: Comparison of the electronic structure of the two hyponitrite isomers. Left: Optimized ground state structures (bond lengths in Å). Right: Transition state structures with arrows indicating the motion along the reaction coordinate.

5.5.2 *Structure related isotope effect of hyponitrite isomers*

The different site preference values for N_2O formation resulting from HNO dimerization and the decomposition of *trans*-hyponitrous acid have to be attributed to differences in the decomposition mechanism of the two single protonated hyponitrite species. In order to shed light on this rarely discussed effect, it is reasonable to analyze the structure of the corresponding *cis* and *trans* species by quantum mechanical methods. Figure 5.3 shows the optimized ground state structures of the two isomers as well as the transition state structures associated with the direct decomposition pathways.

Regarding the ground state structures, two key differences between the two isomers are apparent. The first is the strong hydrogen bonding of the *cis* isomer (see also in chapter 4) that stabilizes this structure. The second is the n(N)→ σ^*(N-O) orbital interaction, which is only possible for the *cis* isomer as well. It has been described by Zevallos *et al.*[123] for the molecular *cis*-hyponitrous acid in more detail. The interaction of these two opposing effects has a major influence on the electronic structure of the *cis* isomer and can best be illustrated by defining an overall linearization angle of the planar structure as the sum of the two sharp angles formed from the two extrapolated N-O bonds intersecting with the in-plane orthogonal of the N-N bond each. In the case of *cis* and *trans* isomers, these angles are calculated to be quite similar about 50° and 45°, respectively. Whereas for the *trans* isomer this value fits into the row of the other *trans* isomers (40° for the molecular acid and 50° for the dianion), the *cis* isomer provides the smallest angle among the other *cis* isomers (52° for the molecular acid and 60° for the dianion). Likewise, the orbital overlap of the n(N)→ σ^*(N-O) interaction, which stabilizes the structure energetically, is lowest in case of the monoanion. The reason for this structural difference is the energetically compensating effect of the strong hydrogen bonding that increases with smaller angles. Consequently, the *cis* isomer can be considered as a strained structure. Once hydrogen bonding decreases, the structure will relax by increasing the linearization

Table 5.2: Calculated vibrational frequencies of the isotopically most abundant *trans*- and the *cis*-hyponitrite anion in the ground and the dissociative transition state based on B3LYP/aug-cc-pVTZ/IEFPCM. For comparison, the frequencies resulting from a G4 calculation are shown in brackets as well.

	trans-hyponitrite anion		*cis*-hyponitrite anion	
Vibration	$\tilde{\nu}$ / cm^{-1}	$\tilde{\nu}_{TST}$ / cm^{-1}	$\tilde{\nu}$ / cm^{-1}	$\tilde{\nu}_{TST}$ / cm^{-1}
ν(O-H) stretch	3616 (3602)	3765 (3775)	3209 (3007)	3778 (3770)
$(\nu$(N-N)(+δ(OH))$_s$	1429 (1424)	1759 (1838)	1430 (1497)	1823 (1888)
$(\nu$(N-N)(+δ(OH))$_{as}$	1302 (1265)	853 (854)	1330 (1348)	748 (766)
ν(N-O) stretch	1210 (1344)	1055 (1108)	1122 (1172)	1146 (1183)
ν(N'-O)(+δ(NNO))$_{as}$	915 (942)	648 (613)	765 (828)	648 (632)
ν(N'-O)(+δ(NNO))$_s$	652 (669)		953 (1008)	
δ(O-NN-OH)	417 (420)	269 (263)	393 (423)	237 (205)
γ(ON-N-O-H)	407 (475)	153 (193)	738 (800)	282 (165)
γ(O-NN-OH)	349 (360)	356 (379)	633 (642)	574 (550)
$\nu^{\ddagger}$ (RC)		502i (401i)		330i (269i)

angle. Such an effect cannot be expected for the *trans* isomer.
The energetically different transition states of the two isomers are a consequence of these electronic effects. On the one hand, the decomposition mechanism requires energy for N-O bond dissociation. On the other hand, reorganization of the NNO fragment from the bent to the linear structure is energetically demanding as well. Along the reaction coordinate of the *cis* isomer, the hydrogen bonding vanishes and the energetically favorable relaxation of the strained structure sets in. As can be seen from the corresponding TST structure in Figure 5.3, the energy maximum of the *cis* isomer decomposition is predominantly connected with N-O bond dissociation. On the contrary, no such relaxation takes place in case of the *trans* isomer and the energy maximum is related to N-O bond dissociation and the reorganization process of the NNO fragment. Thus, the additional energetic stabilizations in the case of the *cis* isomer result in significantly different barrier heights and a change of the molecular dynamics of the dissociation process.
The significantly different characteristics of the reaction coordinate also has an important consequence for the corresponding isotope effect, which is, according to Wolfsberg,[6] "a probe for the force constant changes at the position of isotopic substitution". With respect to isotopic nitrogen substitution, a qualitative picture is directly provided by the transition state structures illustrated in Figure 5.3. For the *cis* isomer dissociation involves mainly the primary nitrogen atom, whereas for the *trans* isomer reorganization and the connected bond order changes mainly involve the secondary nitrogen atom.
Assuming the hyponitrite species as the symmetric intermediate that directly decomposes to form N_2O as well as validity of the rule of geometric mean, the isotopomer

ratio associated with the decomposition mechanism can be dissected into kinetic isotope effects according to

$$\delta^{SP}_{\text{kin}} = \frac{k\,{}^{14}\text{N}^{15}\text{N}^{16}\text{O}}{k\,{}^{15}\text{N}^{14}\text{N}^{16}\text{O}} - 1 = \frac{k\,{}^{14}\text{N}^{15}\text{N}^{16}\text{O} \times k\,{}^{14}\text{N}^{14}\text{N}^{16}\text{O}}{k\,{}^{14}\text{N}^{14}\text{N}^{16}\text{O} \times k\,{}^{15}\text{N}^{14}\text{N}^{16}\text{O}} - 1 = \frac{KIE_{^{15}\text{N},1}}{KIE_{^{15}\text{N},2}} - 1 \tag{5.13}$$

where $KIE_{^{15}\text{N},1}$ and $KIE_{^{15}\text{N},2}$ specify the kinetic isotope effect regarding a single ^{15}N-exchange of the central and the terminal position in the formed nitrous oxide, respectively. Based on the scaled frequencies listed in Table 5.2, it is possible to quantify the single isotope effects. A pronounced primary kinetic isotope effect can be assigned to the decomposition of *cis*-hyponitrite ($KIE_{^{15}\text{N},1} \approx 1.027$). The ^{15}N-isotopic exchange in α position that characterizes the progress of rearrangement towards the N_2O formation has only a minor effect ($KIE_{^{15}\text{N},2} \approx 0.996$). On the contrary, in the *trans* structure isotopic substitution in the broken N-O bond is less sensitive ($KIE_{^{15}\text{N},1} \approx 1.006$) but the secondary α-isotope effect, which is strongly effected by rearrangement, becomes significant ($KIE_{^{15}\text{N},2} \approx 1.021$). Because the secondary isotope effect is inverse with respect to the definition of the site preference, this is equivalent with a preferred formation of ^{15}N^{14}N^{16}O. Overall, a kinetically based site preference of $SP = +31$‰ for the *cis* isomer and $SP = -15$ ‰ for the *trans* isomer is predicted by theoretical means. Thus, both the theoretical prediction and the experiment support the concept that *cis*- and *trans*-hyponitrous acid decomposition are distinguishable by site preference measurements.

5.5.3 *Isotopomer ratio and mechanism of HNO dimerization*

The kinetic isotope effect derived in the previous section for the single protonated *cis*-hyponitrite species ($\delta^{SP}_{\text{kin}} \approx +31$‰) is in qualitative agreement with the experimentally observed effect in HNO dimerization ($\delta^{SP} \approx +40$‰). However, this isotopomer ratio has been derived under the assumption of a symmetric intermediate, but in contrast to $^{-}$ONNO^{-}, which has been assumed by Toyoda *et al.*[19] to explain the kinetic isotope effect, HONNO^{-} is in fact an asymmetric species. A discernible barrier for hydrogen transfer exists and especially in solution two isotopomers should be distinguishable. Consequently, it is not just the kinetic isotope effect of the N-O bond cleavage alone but the overall kinetics of the mechanism that needs to be taken into account to

Table 5.3: Kinetic and equilibrium isotope effects of *trans*- and the *cis*-hyponitrite anion and resulting site preference for the N_2O decomposition reactions based on the frequencies given in Table 5.2.

	trans-hyponitrite anion		*cis*-hyponitrite anion	
Isotope effect	T=298 K	HT limit	T=298 K	HT limit
EIE_{HONNO^-}	1.0112	1.0000	1.0095	1.0000
$KIE_{^{15}\text{N},1}$	1.0060	1.0018	1.0268	1.0128
$KIE_{^{15}\text{N},2}$	1.0205	1.0142	0.9960	1.0014
$\delta^{SP}_{\text{kin}} \times$ 1000	-14.2	-12.2	30.9	11.4

quantitatively predict the isotopomer ratio of the formed nitrous oxide.
Based on the mechanism presented in chapter 4, the following scheme is appropriate to reflect the isotopomer formation

$$\begin{array}{ccccccc} & & & \overset{k_2}{\downarrow} & & \overset{k_3}{\downarrow} & \\ {}^{15}N^{14}NO & \xleftarrow[-OH]{k_{546}^{cis}} & HO^{15}N^{14}NO^- & \underset{k_{-1}}{\overset{k_1}{\rightleftharpoons}} & {}^-O^{15}N^{14}NOH & \xrightarrow[-OH]{k_{456}^{cis}} & {}^{14}N^{15}NO. \end{array} \tag{5.14}$$

Here, k_2 and k_3 are the not necessarily equal rate constants of $HONNO^-$ isotopomer formation from the N-protonated species as shown in the full mechanism. The intramolecular proton transfer between the two *cis*-hyponitrite anion isotopomers (k_1,k_{-1}) is rapid and exhibits a barrier of merely 15 kJ/mol (see chapter 4). In comparison, the decomposition reactions of the two isotopomers with the rate constants k_{546}^{cis} and k_{456}^{cis} into N_2O exhibit a much higher barrier of 42 kJ/mol and proceed with much slower rates.
By making use of the analytical solution derived in a largely analogous kinetic scheme[124] and assuming a common educt, the product ratio can be written as

$$\frac{[^{14}N^{15}NO]}{[^{15}N^{14}NO]} = \frac{k_{456}^{cis}}{k_{546}^{cis}} \times \left(\frac{k_1}{(k_{456}^{cis} + k_{-1})} \times \frac{k_2}{(k_2 + k_3)} + \frac{(k_1 + k_{546}^{cis})}{k_{-1}} \times \frac{k_3}{(k_2 + k_3)} \right). \tag{5.15}$$

However, approximations of the rate constants by transition state theory yield a 3 orders of magnitude higher rate constant for the proton transfer reaction (k_1, k_{-1}) compared to the decomposition reaction (k_{546}, k_{456}). It is therefore justified to neglect the latter in the sum terms. Combination of Equation 5.13 and Equation 5.15 results in

$$\frac{[^{14}N^{15}N^{16}O]}{[^{15}N^{14}N^{16}O]} = \frac{k_{456}^{cis}}{k_{546}^{cis}} \times \frac{k_1}{k_{-1}} = \frac{KIE_{^{15}N,1}^{cis}}{KIE_{^{15}N,2}^{cis}} \times EIE_{HONNO^-}^{cis} \tag{5.16}$$

where $EIE_{HONNO^-}^{cis}$ corresponds to the equilibrium isotope effect of the proton transfer reaction.
Based on this model, rapid equilibration of the two isotopomers of $HONNO^-$ takes place and this leads to two important consequences. On the one hand, reaction steps prior to the equilibrium does not affect isotopic fractionation with respect to the formed N_2O isotopomers. On the other hand, the equilibrium isotope effect of the proton transfer equilibrium, $EIE_{HONNO^-}^{cis}$, adds to the pure kinetic isotope effect of the decomposition. Using the scaled frequencies given in Table 5.2, $EIE_{HONNO^-}^{cis} = 1.0097$ at $T = 298\,K$ is obtained. Hence, combining the kinetic and equilibrium isotope effect, the theoretical site preference of HNO dimerization is predicted to be

$$\delta_{cis}^{SP} = \frac{[^{14}N^{15}NO]}{[^{15}N^{14}NO]} - 1 = +40.9‰. \tag{5.17}$$

This is in excellent agreement with the experimental result of 40 ± 10‰ obtained by the cavity ringdown spectroscopy technique as presented in chapter 3 and only slightly higher than the result of Toyoda *et al.*[19] based on the IRMS technique ($SP \approx +30‰$).

At very low pH values, it is possible that decomposition of the uncharged *cis*-hyponitrous acid contributes to N_2O formation. Therefore, for the sake of completeness, attempts were undertaken to determine the isotopomer effect connected with this pathway. Assuming that the decomposition of the molecular species proceeds via the intramolecular proton transfer with a comparatively high barrier of 78 kJ/mol, a temperature dependent kinetic isotopomer effect on the order of 23 ‰ at $T = 298$ K has been calculated. In contrast to the monoanion, interconversion of the two isotopomers is only possible by simultaneous or sequential rotation of the O−H bonds with respect to the planar structure. For such a rotation, which would be again subject to isotopic fractionation in favor of the $^{14}N^{15}NO$ isotopomer, a barrier of at least 40 kJ/mol needs to be overcome. Therefore, the relevance of this equilibration is questionable. Taking into consideration the fast equilibrium with the monoanion, it is more likely that the isotopic equilibration of the monoanion is transfered to the molecular species. This would result in an overall site preference of 33 ‰ at $T = 298$ K, hence, a quite similar result as for the monoanion. Thus, it remains speculative but plausible to suggest a positive site preference based on the kinetic isotope effect. Further experimental and theoretical work is needed to confirm these assumptions.

5.5.4 *Mechanism of isotopic trans-hyponitrite decomposition*

For the decomposition of the *trans*-hyponitrite isomer, a different mechanism can be assumed to take place. The *trans*-hyponitrite dianion dominating at highly alkaline conditions is a symmetric species and decomposes after protonation to form the monoanion according to the following scheme

$$\begin{array}{ccccc} {}^{-}O^{14}N^{15}NOH & \underset{H^+}{\overset{K_4}{\rightleftharpoons}} & O^{14}N^{15}NO^{2-} & \underset{K_5}{\overset{H^+}{\rightleftharpoons}} & HO^{14}N^{15}NO^{-} \\ \downarrow k_{546}^{trans},\ -OH^- & & (\text{or } HO^{14}N^{15}NOH) & & \downarrow k_{456}^{trans},\ -OH^- \\ {}^{15}N^{14}NO & & & & {}^{14}N^{15}NO \end{array} \tag{5.18, 5.19}$$

Here, in contrast to the *cis*-hyponitrous acid scheme, direct interconversion of the two $HONNO^-$ isotopomers can not take place and only acid-base equilibration with the symmetric anion or, as indicated, molecular *trans*-hyponitrous acid is possible. Assuming steady state conditions for the $HONNO^-$ isotopomers, the isotopomer ratio of N_2O according to this scheme is given by

$$\frac{[^{14}N^{15}NO]}{[^{15}N^{14}NO]} = \frac{k_{456}^{trans}}{k_{546}^{trans}} \times \left(\frac{k_5 (k_{546}^{trans} + k_{-4})}{k_4 (k_{456}^{trans} + k_{-5})} \right). \tag{5.20}$$

Again, the rate constants k_{546}^{trans} and k_{456}^{trans} are much lower than the rate constants associated with the acid-base equilibration (Table 4.1) and thus can be neglected in the sum terms. This simplification yields

$$\frac{[^{14}N^{15}NO]}{[^{15}N^{14}NO]} = \frac{k_{456}^{trans}}{k_{546}^{trans}} \times \frac{K_5}{K_4} = \frac{KIE_{^{15}N,1}^{trans}}{KIE_{^{15}N,2}^{trans}} \times EIE_{HONNO^-}^{trans}. \tag{5.21}$$

Although the mechanism is quite different for the two hyponitrite isomers, the obtained results for the isotopomer effect are identical. For the *trans* isomer, the

correction of the calculated kinetic isotopomer effect by the equilibrium isotope effect as outlined in Table 4.1 yields the overall isotopomer effect at $T = 298\,\mathrm{K}$:

$$\delta^{SP}_{trans} = \frac{[^{14}N^{15}NO]}{[^{15}N^{14}NO]} - 1 = -3.2‰ \tag{5.22}$$

Taking into account the approximations made, this theoretical estimate is in good agreement with the experimental value of $\delta^{SP}_{trans} = \text{-}14 \pm 15‰$. More important, however, is the direct comparison with the *cis* value, $\delta^{SP}_{cis} = +40.9‰$. The fact that the *trans* value is shifted towards a much lower value is consistent with the qualitative dynamics discussed in subsection 5.5.2 and thus underlines the existence of a direct decomposition pathway of the *trans*-hyponitrite anion. Again, this conclusion is in contrast with the previously suggested[110] decomposition of the *trans* isomer after isomerization as shown in Figure 5.1 (red pathway).

5.5.5 *Influence of carbon dioxide catalysis*

In this new context, it is of interest to reinvestigate the carbon dioxide catalyzed decomposition pathway of the *trans*-hyponitrite anion as well. Due to the fact that carbonate impurities are regularly present in the case of hyponitrite preparation, this pathway may contribute as well. According to Loechler *et al.*,[110] this mechanism is also suggested to proceed via isomerization towards the *cis* isomer (red pathway shown in Figure 5.1). Here, the initial N-adduct formation mechanism has been favored based on kinetic arguments derived from a linear free enthalpy relationships. However, calculations of the Gibbs enthalpies of the N- and O-adduct formation reactions performed in this work ($\Delta_r G_{soln} \approx \text{-}3\,\mathrm{kJ/mol}$ and $\Delta_r G_{soln} \approx \text{-}36\,\mathrm{kJ/mol}$, respectively) are strongly in favor of O-adduct formation. Furthermore, potential energy scans along the reaction coordinate revealed that the latter reaction can be considered to be barrier-less. Hence, a rapid and unidirectional reaction forming the O-adduct can be expected. This result would also be consistent with the observation of Feldman and Jansen[125] that the more reactive solid *cis*-hyponitrite decomposes in a carbon dioxide atmosphere under carbonate formation. Focusing on the formed nitrous oxide isotopomers, the following scheme should be applicable for the observed carbonate catalysis

$$\begin{array}{ccccccc}
 & & {}^{-}O^{15}N^{14}NOCO_2^{-} & \overset{+H^+}{\rightleftharpoons} & {}^{-}O^{15}N^{14}NOCO_2H & \xrightarrow[-HCO_3]{k_{456}} & {}^{14}N^{15}NO \\
 & & k^{O}_{CO_2}\uparrow{+CO_2} & & & & k^{cis}_{456}\uparrow{-OH^-} \\
(trans) & {}^{-}O^{14}N^{15}NO^{-} & \overset{+CO_2}{\rightleftharpoons} & {}^{-}O^{14}N^{15}N(CO_2)O^{-} & \xrightarrow[-CO2]{Iso,+H^+} & HO^{(14,15)}N^{(15,14)}NO^{-} & (cis) \\
 & & k^{O}_{CO_2}\downarrow{+CO_2} & & & & k^{cis}_{546}\downarrow{-OH^-} \\
 & & {}^{-}O^{14}N^{15}NOCO_2^{-} & \overset{+H^+}{\rightleftharpoons} & {}^{-}O^{14}N^{15}NOCO_2H & \xrightarrow[-HCO_3]{k_{546}} & {}^{15}N^{14}NO
\end{array}$$

If carbonate catalysis would proceed through N adduct formation as shown in the center line, the *cis* species would decompose. Putting forward the same arguments as for HNO dimerization, this should result in a highly positive site preference value.

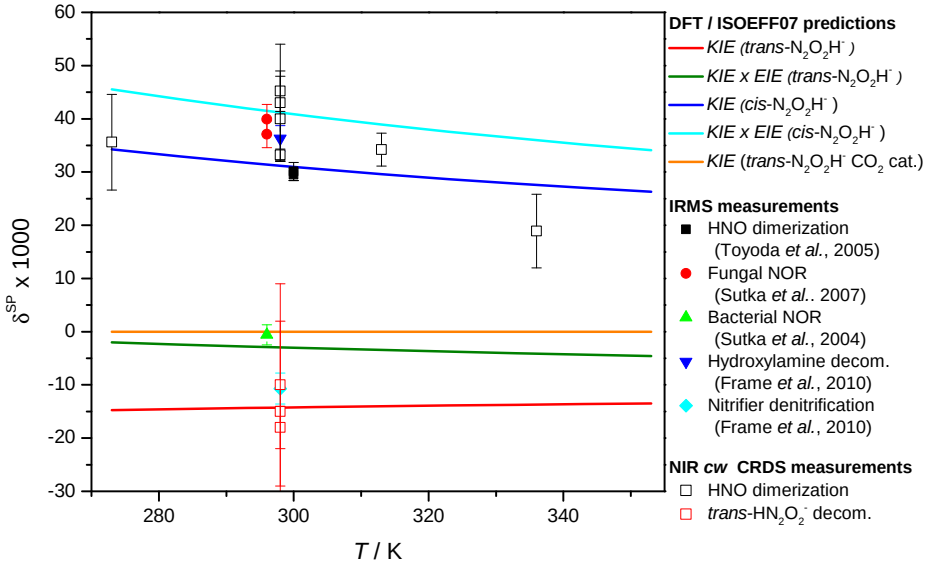

Figure 5.4: Overview of isotopomer ratios from DFT calculations, literature IRMS measurements, and CRDS measurements.

On the contrary, if the O adduct is formed, protonation would yield the unstable $^{-}ONNOCO_2H$ that decomposes with a calculated barrier of 29 kJ/mol to form nitrous oxide. In this case, the isotopomer ratio will be determined by the initial, presumably irreversible step of CO_2-adduct formation. Due to the absence of a barrier, this step is insensitive to the formed isotopomer structure and consequently can be assumed to yield an isotopomer ratio of 0‰. Some additional *trans*-hyponitrite decomposition experiments in presence of carbon dioxide or carbonate have been performed to verify this conclusion. Unfortunately, strongly scattering values in the range from -20 to +20‰ have been observed, nevertheless contradicting a decomposition of the *cis*-hyponitrite anion and in favor of O adduct formation. Based on this experimental and theoretical results, carbonate catalysis in *trans*-hyponitrite decomposition is considered to lead to an isotopomer ratio discernible from both *cis* and *trans* decomposition. Because carbonate is a common impurity in *trans*-hyponitrite synthesis, it cannot be completely ruled out that the measured site preference of *trans*-hyponitrite anion decomposition is somewhat biased, which would result in a slightly to positive site preference value.

5.5.6 *Chemical and biochemical derived isotopomer ratio*

The theoretical expressions outlined in the previous sections enable the calculation of the expected temperature dependence of the isotopomer ratio from HNO dimerization and *trans*-hyponitrite decomposition. These are shown together with the experimental results from CRDS measurements and literature based IRMS measurements of biochemical N_2O sources in Figure 5.4.
As already discussed in subsection 5.5.3 and subsection 5.5.4, the CRDS measurements

of the chemical decomposition pathways fit the theoretical results within error limits. Additional measurements of HNO dimerization at different synthesis temperatures have been performed to reproduce the predicted temperature dependence. However, taking into account the scatter of these data, the theoretically predicted temperature dependence could be neither confirmed nor disproved.

Interestingly, the theoretical and experimental values for decomposition of the *cis*- and *trans*-hyponitrite anion show some parallels with the IRMS measurements of biochemical nitrous oxide formation. In particular, hydroxylamine decomposition in nitrification and fungal denitrification show similar site preference values as *cis*-hyponitrite decomposition, whereas bacterial denitrification and nitrifier denitrification yield similar values as *trans*-hyponitrite decomposition. Following the argument of Spott *et al.*[42] that decomposition of the free species may be relevant in enzyme catalyzed mechanisms as well, gives reason to a speculative interpretation of these coincidences.

(*i*) The decomposition of hydroxylamine is considered to be the main source of nitrous oxide in the nitrification process and the underlying mechanism proceeds basically in absence of enzyme catalysis. Here, oxidation[126,127] and autooxidation[128] pathways have been suggested to yield nitrous oxide via HNO dimerization. The highly positive site preference ($SP \approx +36‰$) in nitrification as found by Frame and Cascanotti[82] would be consistent with this interpretation.

(*ii*) Fungal denitrification involves the P450nor enzyme, in which the active site contains a single heme-iron center. Lehnert *et al.*[31] derived a consistent mechanism based on DFT results explaining the experimental results for selective formation of nitrous oxide. In their and other related studies[129] it was shown that nitrous oxide formation most likely involves the attack of a free nitric oxide on a reduced iron bonded HNOH species. This HNOH species is the only spectroscopically assigned intermediate of the mechanism under low NO conditions. In a very recent QM/MM study preformed by Riplinger and Neese,[32] the mechanism has been revisited and a diradical iron bonded HNOH species has been assigned as intermediate. More importantly in this context is that the calculated decomposition mechanisms revealed a Fe-N bond cleavage upon second NO attack. Thus, decomposition of the free, non-iron-bonded *cis*-hyponitrous acid (anion) within the active site pocket of the enzyme is proposed. Hence, the same final decomposition mechanism as put forward for HNO dimerization should be applicable to explain the almost identical and high site preference of fungal denitrification ($SP \approx +37‰$).[23] Note that such a mechanism would explain the isotopomer preference without assumptions on the isotopic preferences of the involved iron centers. Previous studies[23,44] assumed such a questionable isotopic preference. So far, no experimental evidence for such an isotope effect of the presumably barrierless Fe-NO adduct formation has been reported.

(*iii*) In bacterial denitrification, N-N bond formation takes place in an active site consisting of the bimetallic complexes shown in Figure 1.2. Despite the recently resolved crystal structure,[27] for the underlying mechanism of the reaction three different possible mechanisms have been suggested. Problems in isolating and identifying intermediates complicate a definite identification of the actual mechanisms.[130] However, all mechanisms have in common a hyponitrite species as intermediate. Recently synthesized model complexes mimicking the structure of the active site

of heme/copper oxidase and diiron NOR[131] showed that both metal centers and a protonation step are necessary for the conversion of NO to N_2O. This finding has been interpreted to result from an O-protonation that forms the decomposing hyponitrite monoanion. Moreover, for the enzyme bounded hyponitrite, both a *trans* structure has been suggested by Varotsis *et al.*[29] based on DFT calculations and resonance Raman results as well as a *cis* structure based on a detailed computational analysis of Blomberg et al.[132] In the light of the corresponding site preference of bacterial denitrification ($SP \approx$ -5‰) it would be inconsistent to assume that the free *cis*-hyponitrite anion ($\delta^{SP} \approx$ +40‰) is involved in the final decomposition step. Consequently, an interpretation analogous to fungal NOR or, here, the cis:b_3 mechanism discussed for cNOR can be excluded. However, the reported literature values are similar to the results derived for *trans*-hyponitrite decomposition ($\delta^{SP} \approx$ -3.2‰) and the catalytic decomposition experiment ($\delta^{SP} \approx$ 0‰). Whereas these values are only valid for the decomposition of unbounded species and the O-bonded species, it may be well speculated that these mechanisms are relevant in the corresponding enzyme mechanisms as well.[28] Anyway, the direct decomposition pathway reveals that the counterintuitive preferred formation of $^{15}N^{14}N^{16}O$ is not necessarily related to a preferred isotopic preference of the iron centers. Further insights into the possible coincidences or differences can be expected from high precision site preference measurements to elucidate possible differences between *trans* decomposition and enzymatic decomposition were undertaken.

5.6 CONCLUSION

Isotopomer analysis of N_2O from *trans*-hyponitrite decomposition revealed that the underlying mechanism is accompanied with a site preference of $\delta^{SP} = -15 \pm 15$‰, thus significantly different than the corresponding value obtained from HNO dimerization experiments ($\delta^{SP} = +40 \pm 10$‰). These results underline the previous statement that nitrous oxide formation from HNO dimerization is predominantly related to decomposition of the *cis*-hyponitrite anion. In the case of *trans*-hyponitrous acid in contrast to a previously suggested isomerization pathway as shown in Figure 5.1 a direct decomposition pathway of the corresponding anion is supported. The performed DFT calculations of the reaction dynamics related to the decomposition mechanism basically explained the different nitrous oxide isotopomer ratios of *cis* and *trans* isomer. Furthermore, approximate simple kinetic models yielded a refined and complete picture of both discussed mechanisms. By comparing the site preference results with those of biochemical N_2O formation pathways and their related mechanisms, interesting parallels could be drawn.

6 SUMMARY AND OUTLOOK

A conclusion is simply where you stopped thinking.

— Unknown Author

In this work, different aspects concerning the ^{15}N site preference of nitrous oxide have been investigated. Starting from the fundamental setup of a novel, high resolution *cw* CRD spectrometer its was possible to establish a calibration-free method to determine the isotopomer signature of nitrous oxide. Additionally, detailed DFT calculations enabled the development of a consistent reaction model for the underlying HNO dimerization mechanism which provided a theoretical explanation for the observed site preference. Finally, the observation of an essentially different site preference supported a direct decomposition mechanism of the *trans*-hyponitrite isomer. Taken together the measured and theoretically predicted site preference values, interesting parallels could be drawn with N_2O site preference values found for various biochemical sources.

HIGH RESOLUTION ABSORPTION MEASUREMENTS USING CRDS Cavity ringdown spectroscopy is one of the most sensitive techniques to determine quantitatively sample concentrations based on absorption measurements. The use of narrow-band *cw* diode laser systems significantly improves the attainable sensitivity and spectral resolution enabling low trace gas concentration or very weak absorption measurements. Design and experimental realization of such a setup faces problems associated with (*i*) matching frequency of laser and cavity, (*ii*) maintaining detectable transmission through a high finesse cavity, (*iii*) tuning cavity resonances such that high repetition and single-mode excitation is obtained, and (*iv*) enabling a uniform temperature throughout the cavity. In addition to this, data acquisition and analysis requires electronics optimized for unbiased and rapid signal transmission as well as implementation of fast fitting routines to compress initial raw data (ringdown signal) to its basic information content (decay time). In the here presented setup, these well known challenges for applying *cw* lasers in cavity ringdown spectroscopy have been addressed accordingly.

A more general problem in high resolution laser spectroscopy is the accurate wavelength determination of the probe laser needed for reproducible and comparable spectra as well as single wavelength measurements. In this work, a novel concept using a second wavelength stabilized laser as a permanent internal reference in the FT spectrum of combined lasers after passing an interferometer has been implemented. This rather simple scheme provided a remarkable good reliability, precision (6×10^{-8}) and accuracy (1×10^{-7}), which is comparable to state-of-the-art high end wavemeter technology. Although sufficient for the measurements presented in this thesis, there is still room for improvement of this concept. For example, the frequency difference between the two lasers could be referenced to the stabilized NIR laser instead of the HeNe laser and/or additional stabilized lasers could be used to recalibrate the wavelength axis more accurately.

POTENTIAL OF CRDS FOR ISOTOPOMER RATIO MEASUREMENT In recent years, spectroscopic techniques have been proven to be an powerful alternative to conventional MS techniques in environmental isotope sciences. For example, applications of optical spectrometers were often found less prone to ambient condition changes. The intramolecular distribution of the ^{15}N-isotope in nitrous oxide is one issue that has recently lead to detailed discussions regarding its use to describe nitrous oxide transformation pathways. Here, the principle problem of mass spectrometry based methods is the mass equivalence of the isotopomers and, hence, the need for fragmentation analysis. The apparently different fragmentation behavior of the two isotopomers requires considerable calibration effort and prevents the usually possible high accuracy IRMS measurements. Although several previous attempts to determine the isotopomer ratio of N_2O spectroscopically exist, the general concept followed in this thesis is basically different. Rather weak but isolated absorption lines have been measured with a highly sensitive technique instead of using absorption lines with higher line strength but possible interferences resulting from nearby other absorption lines.

By making use of high resolution mass spectrometry and precise cavity ringdown measurements of highly enriched isotopomer samples, it was possible to characterize chosen absorption lines with an accuracy sufficient for using these parameters to determine the isotopomer ratio. The selective reduction of nitrite has been chosen as a test system involving a HNO dimerization step. Independent of the inital isotopic composition of the source, a significant, constant ^{15}N-site preference of $\delta^{SP} = 40 \pm 10‰$ was determined when using isotopically enriched nitrite. This result is basically consistent with previous IRMS measurements of Toyoda *et al.*[19] and underlines the existence of a heavy atom isotope effect in the corresponding reaction mechanism favoring the $^{14}N^{15}N^{16}O$ isotopomer.

However, taken together the abundance of the two isotopomers in natural samples and the maximum peak absorption calculated from line broadening parameters it became clear that the obtained sensitivity of the used setup is not sufficient for high precision measurements of pure nitrous oxide samples without isotopic enrichment. Further improvement of sensitivity will therefore be necessary to apply this technique to a more generalized isotopomer ratio measurement. Self-evident options are changes of the used mirrors toward higher reflectivity accompanied by better transmittance of these mirrors and/or by a lower detection limit of the detections system and/or by using a laser system with higher output power. Alternatively, techniques that actively lock cavity and laser output frequency provide opportunities of much faster averaging and more precise decay time determination. Compared to the current setup, such locking techniques require additional modulation equipment to set up a Pound-Drever-Hall-locking scheme. Finally, the use of IR quantum cascade or comparable laser systems remains another possibility. Detecting N_2O on fundamental vibrational modes provides higher sensitivities but is less selective due to spectral overlap with other isotopologues.

DIMERIZATION OF HNO IN AQUEOUS SOLUTION The observation of a ^{15}N-site preference in nitrous oxide samples formed by inorganic nitrite reduction has raised the question of the mechanism underlying this isotopomer effect. Elucidating the mechanistic details is of interest for comparison with the dominating biochemical

N_2O sources and to develop a still missing, well characterized reference standard for N_2O site preference. As in many other N_2O forming reactions, dimerization of nitroxyl (HNO) has been suggested as the key reaction sequence. Recent drastic changes in the evaluation of HNO chemistry including the relevant spin states and the deprotonation equilibrium as well as a reassessment of the overall rate constant of dimerization pointed to a previously underestimated relevance in biochemistry. However, numerous experimental observations remained inconsistent with the theoretically derived and experimentally suggested mechanisms.

In order to resolve discrepancies of the known HNO dimerization mechanism in aqueous solution, a complete reassessment based on DFT calculations was undertaken in this work. Compared to the previously reported gas phase mechanisms, energetic contributions from dipole moment stabilization lead to a reversal of the *cis*-*trans* ratio of the initially formed HNO dimer. This assignment of the *cis*-dimer is also able to explain the experimentally observed rate increase in solution. For the sequential mechanism, a scheme of acid-base equilibration reactions has been worked out based on the proton exchange method. The alternative intramolecular rearrangement model taking solvation both implicitly and explicitly into account turned out to be inconsistent. Analysis of the possible unstable intermediates and equilibria showed that the previously neglected *cis*-hyponitrite anion is the principle source of N_2O. Despite high thermodynamic stability it is highly unstable towards decomposition into nitrous oxide. An interesting aspect in this context is the calculated acid-base equilibrium of the *cis*-hyponitrite isomer. It has been analyzed for the first time and revealed striking differences in comparison with the corresponding well characterized *trans* isomer. Finally, theoretically derived rate constants verified that the proposed mechanism is kinetically feasible and additional HNO dimerization experiments were consistent with the outlined interpretation.

Overall, the results provided a reasonable and reliable explanation for the reaction mechanism underlying HNO dimerization. The mechanism is able to reflect various experimental observations, in particular, the increase of the initial dimerization rate constant in solution, the absence of traceable intermediates, the problems concerning isolation of *cis*-hyponitrite, and the related isotope studies. The outcome of this study emphasizes the uncertainties still present in nitrogen related chemistry in solution. However, for an improved quantitative understanding, it is necessary to apply higher level of theory calculations overcoming the approximations implicitly contained in the applied DFT and PCM models. Progress may be expected from the future application of QM/MM models.

SITE PREFERENCE IN INORGANIC NITROUS OXIDE FORMATION As the use of the ^{15}N-site preference of nitrous oxide has extended to characterize nitrogen cycles in facilities as different as waste water or biogas plants, the origin of ^{15}N-site preference in source characterization remained a controversial issue discussed by many authors. The variety of values of this parameter found in different pure bacteria and fungal cultures was often interpreted to depend on the culture or on the enzyme involved. An explanation given by Toyoda *et al.*[19] relied on the involvement of the iron centers to explain isotopic preference in enzyme catalysis and on a heavy atom isotope effect in the symmetric $^{-}O^{14}N^{15}NO^{-}$ to explain the inorganic mechanism. In the light of the verified isotopomer effect and the quantum chemically derived HNO

dimerization mechanism put forward in this work, some aspects of this interpretation appeared questionable. Moreover, the role of the *cis-trans* isomer structure of the intermediates had not been addressed so far. In fact, the pure existence of a *trans*-hyponitrite anion decomposition mechanism has been controversially discussed and it has been suggested to originate from slow isomerization toward the *cis* isomer.
In this work, spectroscopic analysis of ^{15}N-isotopically enriched nitrous oxide samples from synthesized *trans*-hyponitrite decomposition revealed a significantly different ^{15}N-site preference of $\delta^{SP} = -14 \pm 15$‰ supporting both a minor if any contribution of *trans*-hyponitrite decomposition to HNO dimerization and an independent decomposition mechanism of the *trans*-hyponitrite anion. The differences in the *cis*-/*trans*-hyponitrite anion decomposition mechanism were elucidated by performing detailed DFT studies of the optimized equilibrium structures and the related reaction dynamics. The interplay of orbital interactions and hydrogen bonding was found to affect the reaction coordinate such that the effect of isotopic substitution differs substantially for both isomers. In accordance with the experimental results, kinetic isotopomer effects alone yielded preferences of $^{14}N^{15}N^{16}O$ for *cis*-hyponitrite and preferences of $^{15}N^{14}N^{16}O$ for *trans*-hyponitrite. Taking into account fractionation effects of the underlying mechanisms in an appropriate manner, the final theoretical predictions of δ^{SP} is +40‰ for HNO dimerization and -3‰ for *trans*-hyponitrite decomposition. These values show similarities with results derived from biochemical formation pathways in which the role of the isomer structure has not been considered so far. As a comparison with recent quantum chemical simulations of the enzyme mechanism revealed the presence of the corresponding isomers, it may well be speculated that the isomer structure plays a role for isotopomer preference of biochemical pathways as well. For example, it has recently been shown that in the case of fungal denitrification nitrous oxide formation is related to the decomposition of the unbound hyponitrite species. For sure, more work - high precision experimental and high-level theoretical - is needed to elucidate all the relevant details of inorganic and biochemical pathways.

BIBLIOGRAPHY

[1] Möller, D. *Chemistry of the Climate System*; de Gruyter, Berlin, 2010.

[2] Arrhenius, S. On the influence of carbonic acid in the air upon the temperature of the ground. *Philos. Mag.* **1896**, *41*, 237–276.

[3] Keeling, C. D. The concentration and isotopic abundances of atmospheric carbon dioxide in rural areas. *Geochim. Cosmochim. Acta* **1958**, *13*, 322 – 334.

[4] IPCC, *Fourth Assessment Report: Climate Change 2007: Working Group I Report: The Physical Science Basis*; Cambridge University Press, 2007; p 996.

[5] Heard, D. E., Ed. *Analytical techniques for atmospheric measurements*; Wiley, 2006.

[6] Wolfsberg, M.; Hook, W. A. V.; Paneth, P. *Isotope Effects in the Chemical, Geological, and Bio Science*; Springer, 2010.

[7] Wuebbles, D. J. Nitrous Oxide: No Laughing Matter. *Science* **2009**, *326*, 56–57.

[8] Mebel, A. M.; Lin, M. C.; Morokuma, K.; Melius, C. F. Theoretical study of reactions of N_2O with NO and OH radicals. *Int. J. Chem. Kinet.* **1996**, *28*, 693–703.

[9] Crutzen, P. J. The influence of nitrogen oxides on the atmospheric ozone content. *Quart. J. R. Met. Soc.* **1970**, *96*, 320–325.

[10] Johnston, H. Reduction of Stratospheric Ozone by Nitrogen Oxide Catalysts from Supersonic Transport Exhaust. *Science* **1971**, *173*, 517–522.

[11] Ravishankara, A. R.; Daniel, J. S.; Portmann, R. W. Nitrous Oxide (N_2O): The Dominant Ozone-Depleting Substance Emitted in the 21^{st} Century. *Science* **2009**, *326*, 123–125.

[12] Crutzen, P. J.; Mosier, A. R.; Smith, K. A.; Winiwarter, W. N_2O release from agro-biofuel production negates global warming reduction by replacing fossil fuels. *Atmos. Chem. Phys.* **2008**, *8*, 389–395.

[13] Brenninkmeijer, C. A. M.; Janssen, C.; Kaiser, J.; Röckmann, T.; Rhee, T. S.; Assonov, S. S. Isotope Effects in the Chemistry of Atmospheric Trace Compounds. *Chem. Rev.* **2003**, *103*, 5125–5162.

[14] Yoshida, N.; Toyoda, S. Constraining the atmospheric N_2O budget from intramolecular site preference in N_2O isotopomers. *Nature* **2000**, *405*, 330–334.

[15] Westley, M. B.; Popp, B. N.; Rust, T. M. The calibration of the intramolecular nitrogen isotope distribution in nitrous oxide measured by isotope ratio mass spectrometry. *Rapid Commun. Mass Spectrom.* **2007**, *21*, 391–405.

[16] Bange, H. New Directions: The importance of oceanic nitrous oxide emissions. *Atmos. Environ.* **2006**, *40*, 198 – 199.

[17] Rhee, T. S.; Kettle, A. J.; Andreae, M. O. Methane and nitrous oxide emissions from the ocean: A reassessment using basin-wide observations in the Atlantic. *J. Geophys. Res.* **2009**, *114*, D12304.

[18] Toyoda, S.; Yoshida, N.; Miwa, T.; Matsui, Y.; Yamagishi, H.; Tsunogai, U.; Nojiri, Y.; Tsurushima, N. Production mechanism and global budget of N_2O inferred from its isotopomers in the western North Pacific. *Geophys. Res. Lett.* **2002**, *29*, 1037.

[19] Toyoda, S.; Mutobe, H.; Yamagishi, H.; Yoshida, N.; Tanji, Y. Fractionation of N_2O isotopomers during production by denitrifier. *Soil Biol. Biochem.* **2005**, *37*, 1535–1545.

[20] Toyoda, S.; Iwai, H.; Koba, K.; Yoshida, N. Isotopomeric analysis of N_2O dissolved in a river in the Tokyo metropolitan area. *Rapid Commun. Mass Spectrom.* **2009**, *23*, 809–821.

[21] Sutka, R. L.; Ostrom, N. E.; Ostrom, P. H.; Gandhi, H.; Breznak, J. A. Nitrogen isotopomer site preference of N_2O produced by Nitrosomonas europaea and Methylococcus capsulatus Bath. *Rapid Commun. Mass Spectrom.* **2003**, *17*, 738–745.

[22] Sutka, R. L.; Ostrom, N. E.; Ostrom, P. H.; Breznak, J. A.; Gandhi, H.; Pitt, A. J.; Li, F. Distinguishing Nitrous Oxide Production from Nitrification and Denitrification on the Basis of Isotopomer Abundances. *Appl. Environ. Microbiol.* **2006**, *72*, 638–644.

[23] Sutka, R. L.; Adams, G. C.; Ostrom, N. E.; Ostrom, P. H. Isotopologue fractionation during N_2O production by fungal denitrification. *Rapid Commun. Mass Spectrom.* **2008**, *22*, 3989–3996.

[24] Ostrom, N. E.; Sutka, R.; Ostrom, P. H.; Grandy, A. S.; Huizinga, K. M.; Gandhi, H.; von Fischer, J. C.; Robertson, G. P. Isotopologue data reveal bacterial denitrification as the primary source of N_2O during a high flux event following cultivation of a native temperate grassland. *Soil Biol. Biochem.* **2010**, *42*, 499 – 506.

[25] Köster, J. R.; Cárdenas, L.; Senbayram, M.; Bol, R.; Well, R.; Butler, M.; Mühling, K. H.; Dittert, K. Rapid shift from denitrification to nitrification in soil after biogas residue application as indicated by nitrous oxide isotopomers. *Soil Biol. Biochem.* **2011**, *43*, 1671 – 1677.

[26] Toyoda, S.; Suzuki, Y.; Hattori, S.; Yamada, K.; Fujii, A.; Yoshida, N.; Kouno, R.; Murayama, K.; Shiomi, H. Isotopomer Analysis of Production and Consumption Mechanisms of N_2O and CH_4 in an Advanced Wastewater Treatment System. *Environ. Sci. Technol.* **2011**, *45*, 917–922.

[27] Hino, T.; Matsumoto, Y.; Nagano, S.; Sugimoto, H.; Fukumori, Y.; Murata, T.; Iwata, S.; Shiro, Y. Structural Basis of Biological N_2O Generation by Bacterial Nitric Oxide Reductase. *Science* **2010**, *330*, 1666–1670.

[28] Moënne-Loccoz, P.; Fee, J. A. Catalyzing NO to N_2O in the Nitrogen Cycle. *Science* **2010**, *330*, 1632–1633.

[29] Varotsis, C.; Ohta, T.; Kitagawa, T.; Soulimane, T.; Pinakoulaki, E. The Structure of the Hyponitrite Species in a Heme Fe-Cu Binuclear Center. *Angew. Chem.* **2007**, *119*, 2260–2264.

[30] Xu, N.; Campbell, A. L. O.; Powell, D. R.; Khandogin, J.; Richter-Addo, G. B. A Stable Hyponitrite-Bridged Iron Porphyrin Complex. *J. Am. Chem. Soc.* **2009**, *131*, 2460–2461.

[31] Lehnert, N.; Praneeth, V.; Paulat, F. Electronic structure of iron (II)–porphyrin nitroxyl complexes: Molecular mechanism of fungal nitric oxide reductase (P450nor). *J. Comput. Chem.* **2006**, *27*, 1338–1351.

[32] Riplinger, C.; Neese, F. The Reaction Mechanism of Cytochrome P450 NO Reductase: A Detailed Quantum Mechanics/Molecular Mechanics Study. *ChemPhysChem* **2011**, *12*, 3192–3203.

[33] Garber, E. A.; Hollocher, T. C. Positional isotopic equivalence of nitrogen in N2O produced by the denitrifying bacterium Pseudomonas stutzeri. Indirect evidence for a nitroxyl pathway. *J. Biol. Chem.* **1982**, *257*, 4705–4708.

[34] Walker, C. B. et al. Nitrosopumilus maritimus genome reveals unique mechanisms for nitrification and autotrophy in globally distributed marine crenarchaea. *Proc. Natl. Acad. Sci. U. S. A.* **2010**, *107*, 8818–8823.

[35] Hughes, M.; Stedman, G. Kinetics and mechanism of the reaction between nitrous acid and hydroxylamine. Part I. *J. Chem. Soc.* **1963**, 2824–2830.

[36] Hussain, M. A.; Stedman, G.; Hughes, M. N. Kinetics and mechanism of the reaction between nitrous acid and hydroxylamine. Part III. The formation of hyponitrous acid. *J. Chem. Soc. B* **1968**, 597–603.

[37] Morgan, T. D. B.; Stedman, G.; Hughes, M. N. Kinetics and mechanism of the reaction between nitrous acid and hydroxylamine. Part II. The alkyl hydroxylamines. *J. Chem. Soc. B* **1968**, 344–349.

[38] Raman, S.; Ashcraft, R. W.; Vial, M.; Klasky, M. L. Oxidation of Hydroxylamine by Nitrous and Nitric Acids. Model Development from First Principle SCRF Calculations. *J. Phys. Chem. A* **2005**, *109*, 8526–8536.

[39] Ashcraft, R. W.; Raman, S.; Green, W. H. Predicted Reaction Rates of HxNyOz Intermediates in the Oxidation of Hydroxylamine by Aqueous Nitric Acid. *J. Phys. Chem. A* **2008**, *112*, 7577–7593.

[40] Ashcraft, R. W.; Raman, S.; Green, W. H. Ab Initio Aqueous Thermochemistry: Application to the Oxidation of Hydroxylamine in Nitric Acid Solution. *J. Phys. Chem. B* **2007**, *111*, 11968–11983.

[41] Garber, E. A.; Hollocher, T. C. ^{15}N,^{18}O tracer studies on the activation of nitrite by denitrifying bacteria. Nitrite/water-oxygen exchange and nitrosation

reactions as indicators of electrophilic catalysis. *J. Biol. Chem.* **1982**, *257*, 8091–8097.

[42] Spott, O.; Russow, R.; Stange, C. F. Formation of hybrid N_2O and hybrid N_2 due to codenitrification: First review of a barely considered process of microbially mediated N-nitrosation. *Soil Biol. Biochem.* **2011**, *43*, 1995 – 2011.

[43] Schmidt, H.-L.; Werner, R. A.; Yoshida, N.; Well, R. Is the isotopic composition of nitrous oxide an indicator for its origin from nitrification or denitrification? A theoretical approach from referred data and microbiological and enzyme kinetic aspects. *Rapid Commun. Mass Spectrom.* **2004**, *18*, 2036–2040.

[44] Stein, L. Y.; Yung, Y. L. Production, isotopic composition, and atmospheric fate of biologically produced nitrous oxide. *Annu. Rev. Earth Planet. Sci.* **2003**, *31*, 329–356.

[45] Anderson, D. Z.; Frisch, J. C.; Masser, C. S. Mirror reflectometer based on optical cavity decay time. *Appl. Opt.* **1984**, *23*, 1238–1245.

[46] O'Keefe, A.; Deacon, D. A. G. Cavity ring-down optical spectrometer for absorption measurements using pulsed laser sources. *Rev. Sci. Instrum.* **1988**, *59*, 2544–2551.

[47] Busch, K. W., Busch, M. A., Eds. *Cavity-Ringdown Spectroscopy: An Ultratrace-Absorption Measurement Technique*; Oxford University Press, 1999.

[48] Romanini, D.; Kachanov, A. A.; Sadeghi, N.; Stoeckel, F. CW cavity ring down spectroscopy. *Chem. Phys. Lett.* **1997**, *264*, 316 – 322.

[49] He, Y.; Orr, B. J. Rapidly swept, continuous-wave cavity ringdown spectroscopy with optical heterodyne detection: single- and multi-wavelength sensing of gases. *Appl. Phys. B* **2002**, *75*, 267–280.

[50] Berden, G., Engeln, R., Eds. *Cavity Ring-Down Spectrscopy: Techniques and Applications*; Wiley, 2009.

[51] Hodges, J. T.; Ciurylo, R. Automated high-resolution frequency-stabilized cavity ring-down absorption spectrometer. *Rev. Sci. Instrum.* **2005**, *76*, 023112.

[52] Hodges, J. T.; Layer, H. P.; Miller, W. W.; Scace, G. E. Frequency-stabilized single-mode cavity ring-down apparatus for high-resolution absorption spectroscopy. *Rev. Sci. Instrum.* **2004**, *75*, 849–863.

[53] Ye, C. *Tunable external cavity diode lasers*; World Scientific Pub Co Inc, 2004.

[54] Demtröder, W. *Laserspektroskopie*, 5th ed.; Springer, Berlin, 2007.

[55] Lehmann, K. L.; Romanini, D. The superposition principle and cavity ring-down spectroscopy. *J. Chem. Phys.* **1996**, *105*, 10263–10277.

[56] Friedman, L.; Bigeleisen, J. Oxygen and Nitrogen Isotope Effects in the Decomposition of Ammonium Nitrate. *J. Chem. Phys.* **1950**, *18*, 1325–1331.

[57] Toyoda, S.; Yoshida, N. Determination of Nitrogen Isotopomers of Nitrous Oxide on a Modified Isotope Ratio Mass Spectrometer. *Anal. Chem.* **1999**, *71*, 4711–4718.

[58] Kaiser, J.; Park, S.; Boering, K.; Brenninkmeijer, C.; Hilkert, A.; Röckmann, T. Mass spectrometric method for the absolute calibration of the intramolecular nitrogen isotope distribution in nitrous oxide. *Anal. Bioanal. Chem.* **2004**, *378*, 256–269.

[59] Esler, M. B.; Griffith, D. W. T.; Turatti, F.; Wilson, S. R.; Rahn, T.; Zhang, H. N_2O concentration and flux measurements and complete isotopic analysis by FTIR spectroscopy. *Chemosphere: Global Change Sci.* **2000**, *2*, 445 – 454.

[60] Griffith, D. W. T.; Parkes, S. D.; Haverd, V.; Paton-Walsh, C.; Wilson, S. R. Absolute Calibration of the Intramolecular Site Preference of ^{15}N Fractionation in Tropospheric N_2O by FT-IR Spectroscopy. *Anal. Chem.* **2009**, *81*, 2227–2234.

[61] Uehara, K.; Yamamoto, K.; Kikugawa, T.; Yoshida, N. Site-selective nitrogen isotopic ratio measurement of nitrous oxide using 2 μm diode lasers. *Spectrochim. Acta Part A* **2003**, *59*, 957–962.

[62] Nakayama, T.; Fukuda, H.; Kamikawa, T.; Sugita, A.; Kawasaki, M.; Morino, I.; Inoue, G. Measurements of the $3\nu_3$ band of $^{14}N^{15}N^{16}O$ and $^{15}N^{14}N^{16}O$ using continuous-wave cavity ring-down spectroscopy. *Appl. Phys. B* **2007**, *88*, 137–140.

[63] Waechter, H.; Mohn, J.; Tuzson, B.; Emmenegger, L.; Sigrist, M. W. Determination of N_2O isotopomers with quantum cascade laser based absorption spectroscopy. *Opt. Express* **2008**, *16*, 9239–9244.

[64] Mohn, J.; Guggenheim, C.; Tuzson, B.; Vollmer, M. K.; Toyoda, S.; Yoshida, N.; Emmenegger, L. A liquid nitrogen-free preconcentration unit for measurements of ambient N_2O isotopomers by QCLAS. *Atmos. Meas. Tech.* **2010**, *3*, 609–618.

[65] Balslev-Clausen, D. M. Application of cavity ring down spectroscopy to isotopic bio-, geo-, & climate-sciences & the development of a mid-infrared CRDS analyzer for continuous measurements of N_2O isotopomers. Ph.D. thesis, University of Copenhagen, 2011.

[66] Rothman, L. et al. The HITRAN 2008 molecular spectroscopic database. *J. Quant. Spectrosc. Radiat. Transfer* **2009**, *110*, 533 – 572.

[67] Song, K.; Liu, A.; Ni, H.; Hu, S. Fourier-transform spectroscopy of $^{15}N^{14}N^{16}O$ in the 3500-9000 cm^{-1} region. *J. Mol. Spectrosc.* **2009**, *255*, 24–31.

[68] Ni, H.-Y.; Song, K.-F.; Perevalov, V.; Tashkun, S.; Liu, A.-W.; Wang, L.; Hu, S.-M. Fourier-transform spectroscopy of $^{14}N^{15}N^{16}O$ in the 3800-9000 cm^{-1} region and global modeling of its absorption spectrum. *J. Mol. Spectrosc.* **2008**, *248*, 41–60.

[69] Lyulin, O.; Jacquemart, D.; Lacome, N.; Tashkun, S.; Perevalov, V. Line parameters of $^{15}N_2^{16}O$ from Fourier transform measurements in the 5800-7600 cm^{-1}

region and global fitting of line positions from 1000 to 7600 cm^{-1}. *J. Quant. Spectrosc. Radiat. Transfer* **2010**, *111*, 345 – 356.

[70] Lapinski, A.; Spanget-Larsen, J.; Waluk, J.; Radziszewski, J. G. Vibrations of nitrous oxide: Matrix isolation Fourier transform infrared spectroscopy of twelve N_2O isotopomers. *J. Chem. Phys.* **2001**, *115*, 1757–1764.

[71] Toth, R. A. Line Positions and Strengths of N_2O between 3515 and 7800 cm^{-1}. *J. Mol. Spectrosc.* **1999**, *197*, 158 – 187.

[72] Liu, A.; Kassi, S.; Perevalov, V.; Tashkun, S.; Campargue, A. High sensitivity *cw*-Cavity Ring Down Spectroscopy of N_2O near 1.5 µm (II). *J. Mol. Spectrosc.* **2007**, *244*, 48–62.

[73] Bernath, P. F. *Spectra of Atoms and Molecules*; Oxford University Press, 1995.

[74] Fried, A.; Richter, D. *Analytical Techniques for Atmospheric Measurements*; Blackwell Publishing, 2006.

[75] Cohen, E. R.; Frey, J. G.; Kuchitsu, K.; Mills, I.; Quack, M.; Strauss, H.; Thor, A. J.; Cvitas, T.; Holmstroem, B.; Marquardt, R.; Pavese, F.; Stohner, J.; Takami, M. *Quantities, Units and Symbols in Physical Chemistry*, 3rd ed.; RCS Publishing, Cambridge, 2007.

[76] Voigt, W. Über das Gesetz der Intensitätsverteilung innerhalb der Linien eines Gasspektrums. *K. Bayern Akad. München.*, **1912**, 603–620.

[77] Dicke, R. H. The Effect of Collisions upon the Doppler Width of Spectral Lines. *Phys. Rev.* **1953**, *89*, 472–473.

[78] Galatry, L. Simultaneous Effect of Doppler and Foreign Gas Broadening on Spectral Lines. *Phys. Rev.* **1961**, *122*, 1218–1223.

[79] Herbert, F. Spectrum line profiles: A generalized Voigt function including collisional narrowing. *J. Quant. Spectrosc. Radiat. Transfer* **1974**, *14*, 943 – 951.

[80] Ouyang, X.; Varghese, P. L. Reliable and efficient program for fitting Galatry and Voigt profiles to spectral data on multiple lines. *Appl. Opt.* **1989**, *28*, 1538–1545.

[81] Rautian, S. G.; Sobel'man, I. I. The effect of collisions on the doppler broadening of spectral lines. *Sov. Phys. Usp.* **1967**, *9*, 701.

[82] Frame, C. H.; Casciotti, K. L. Biogeochemical controls and isotopic signatures of nitrous oxide production by a marine ammonia-oxidizing bacterium. *Biogeosciences* **2010**, *7*, 2695–2709.

[83] Olivier, J. L.; Locht, R.; Momigny, J. A dissociative electroionization study of nitrous oxide. The NO^+ and N_2^+ dissociation channels. *Chem. Phys.* **1982**, *68*, 201–211.

[84] Daumont, L.; Auwera, J.; Teffo, J.-L.; Perevalov, V.; Tashkun, S. Line Intensity Measurements in $^{14}N_2^{16}O$ and Their Treatment Using the Effective Dipole Moment Approach: I. The 4300 to 5200 cm^{-1} Region. *J. Mol. Spectrosc.* **2001**, *208*, 281–291.

[85] Henry, A.; Hurtmans, D.; Margottin-Maclou, M.; Valentin, A. Confinement narrowing and absorber speed dependent broadening effects on CO lines in the fundamental band perturbed by Xe, Ar, Ne, He and N_2. *J. Quant. Spectrosc. Radiat. Transfer* **1996**, *56*, 647–671.

[86] Bell, K. E.; Kelly, H. C. Acid-Catalyzed Amine-Borane Reduction of Nitrite. *Inorg. Chem.* **1996**, *35*, 7225–7228.

[87] Angeli, A. *Gazz. Chim. Ital.* **1903**, *33*, 245.

[88] Brown, H. W.; Pimentel, G. C. Photolysis of Nitromethane and of Methyl Nitrite in an Argon Matrix; Infrared Detection of Nitroxyl, HNO. *J. Chem. Phys.* **1958**, *29*, 883–888.

[89] Grätzel, M.; Taniguchi, S.; Henglein, A. Pulsradiolytische Untersuchung kurzlebiger Zwischenprodukte der NO-Reduktion in wäßriger Lösung. *Ber. Bunsenges. Phys. Chem.* **1970**, *74*, 1003–1010.

[90] Seel, F.; Bliefert, C. Der Mechanismus der Zersetzung des Natriumsalzes der Benzolsulfhydroxamsäure in wässriger Lösung. *Z. Anorg. Allg. Chem.* **1972**, *394*, 187–196.

[91] Bartberger, M. D.; Fukuto, J. M.; Houk, K. N. On the acidity and reactivity of HNO in aqueous solution and biological systems. *Proc. Natl. Acad. Sci. U. S. A.* **2001**, *98*, 2194–2198.

[92] Shafirovich, V.; Lymar, S. V. Nitroxyl and its anion in aqueous solutions: Spin states, protic equilibria, and reactivities toward oxygen and nitric oxide. *Proc. Natl. Acad. Sci. U. S. A.* **2002**, *99*, 7340–7345.

[93] Bartberger, M. D.; Liu, W.; Ford, E.; Miranda, K. M.; Switzer, C.; Fukuto, J. M.; Farmer, P. J.; Wink, D. A.; Houk, K. N. The reduction potential of nitric oxide (NO) and its importance to NO biochemistry. *Proc. Natl. Acad. Sci. U. S. A.* **2002**, *99*, 10958–10963.

[94] Miranda, K. M. The chemistry of nitroxyl (HNO) and implications in biology. *Coord. Chem. Rev.* **2005**, *249*, 433 − 455.

[95] Maier, G.; Reisenauer, H. P.; De Marco, M. Isonitroso Hydrogen (Hydroxy Nitrene, HON). *Angew. Chem. Int. Ed.* **1999**, *38*, 108–110.

[96] Strausz, O. P.; Gunning, H. E. Reaction of hydrogen atoms with nitric oxide. *Trans. Faraday Soc.* **1964**, *60*, 347–358.

[97] Kohout, F. C.; Lampe, F. W. On the Role of the Nitroxyl Molecule in the Reaction of Hydrogen Atoms with Nitric Oxide. *J. Am. Chem. Soc.* **1965**, *87*, 5795–5796.

[98] Callear, A. B.; Carr, R. W. Thermal decomposition of HNO. *J. Chem. Soc., Faraday Trans.* **1975**, *71*, 1603–1609.

[99] Bryukov, M.; Kachanov, A.; Timonnen, R.; Seetula, J.; Vandoren, J.; Sarkisov, O. Kinetics of HNO reactions with O_2 and HNO. *Chem. Phys. Lett.* **1993**, *208*, 392–398.

[100] Lin, M. C.; He, Y.; Melius, C. F. Theoretical interpretation of the kinetics and mechanisms of the HNO + HNO and HNO + 2NO reactions with a unified model. *Int. J. Chem. Kinet.* **1992**, *24*, 489–516.

[101] Lüttke, W.; Skancke, P. N.; Traetteberg, M. On the dimerization process of nitroso compounds. *Theor. Chem. Acc.* **1994**, *87*, 321–333.

[102] Ruud, K.; Helgaker, T.; Uggerud, E. Mechanisms, energetics and dynamics of a key reaction sequence during the decomposition of nitromethane: HNO + HNO –> N_2O + H_2O. *J. Mol. Struct.* **1997**, *393*, 59 – 71.

[103] Bazylinski, D. A.; Hollocher, T. C. Evidence from the reaction between trioxodinitrate(II) and nitrogen-15-labeled nitric oxide that trioxodinitrate(II) decomposes into nitrosyl hydride and nitrite in neutral aqueous solution. *Inorg. Chem.* **1985**, *24*, 4285–4288.

[104] Bennett, M. R.; Maya, L.; Brown, G. M.; Posey, F. A. Oxidation of hydroxylamine by nitrous and nitric acids. *Inorg. Chem.* **1982**, *21*, 2461–2468.

[105] Jensen, F. *Introduction to Computational Chemistry*; Wiley-VCH, Weiheim, 2003.

[106] Hohenberg, P.; Kohn, W. Inhomogeneous Electron Gas. *Phys. Rev.* **1964**, *136*, B864–B871.

[107] Ho, J.; Coote, M. L. pK_a Calculation of Some Biologically Important Carbon Acids - An Assessment of Contemporary Theoretical Procedures. *J. Chem. Theory Comput.* **2009**, *5*, 295–306.

[108] Kee, R.; Ruply, F.; Miller, J. Chemkin-II: A Fortran Chemical Kinetics Package for the Analysis of Gas-Phase Chemical Kinetics; Sandia Report SAND89-8009, Sandia National Laboratories, Livermore, CA, 1989.

[109] Bonner, F. T.; Ko, Y. Kinetic, isotopic, and nitrogen-15 NMR study of N-hydroxybenzenesulfonamide decomposition: an nitrosyl hydride (HNO) source reaction. *Inorg. Chem.* **1992**, *31*, 2514–2519.

[110] Loechler, E. L.; Schneider, A. M.; Schwartz, D. B.; Hollocher, T. C. Covalent electrophilic catalysis of the breakdown of hyponitrite to nitrous oxide by aldehydes, ketones, and carbon dioxide. *J. Am. Chem. Soc.* **1987**, *109*, 3076–3087.

[111] Guggenheim, E. On the determination of the velocity constant of a unimolecular reaction. *Philos. Mag.* **1926**, *2*, 538–543.

[112] Swinbourne, E. Method for obtaining the rate coefficient and final concentration of a first-order reaction. *J. Chem. Soc.* **1960**, *473*, 2371–2372.

[113] Santoro, A. E.; Buchwald, C.; McIlvin, M. R.; Casciotti, K. L. Isotopic Signature of N_2O Produced by Marine Ammonia-Oxidizing Archaea. *Science* **2011**, *333*, 1282–1285.

[114] Bonner, F. T.; Kada, J.; Phelan, K. G. Symmetry of the intermediate in the hydroxylamine-nitrous acid reaction. *Inorg. Chem.* **1983**, *22*, 1389–1391.

[115] Morgenstern, M.; Schowen, R. Prediction of isotope effects for anticipated intermediate structures in the course of bacterial denitrification. *Z. Naturforsch. A* **1989**, *44*, 450–458.

[116] Samarkin, V. A.; Madigan, M. T.; Bowles, M. W.; Casciotti, K. L.; Priscu, J. C.; McKay, C. P.; Joye, S. B. Abiotic nitrous oxide emission from the hypersaline Don Juan Pond in Antarctica. *Nat. Geosci.* **2010**, *3*, 341–344.

[117] Bigeleisen, J.; Mayer, M. G. Calculation of Equilibrium Constants for Isotopic Exchange Reactions. *J. Chem. Phys.* **1947**, *15*, 261–267.

[118] Frisch, M. J. et al. Gaussian 09 Revision A.02. Gaussian Inc. Wallingford CT 2009.

[119] Irikura, K. K.; Johnson, R. D.; III,; Kacker, R. N.; Kessel, R. Uncertainties in scaling factors for ab initio vibrational zero-point energies. *J. Chem. Phys.* **2009**, *130*, 114102.

[120] Anisimov, V.; Paneth, P. ISOEFF98. A program for studies of isotope effects using Hessian modifications. *J. Math. Chem.* **1999**, *26*, 75–86.

[121] Addison, C. C.; Gamlen, G. A.; Thompson, R. The ultra-violet absorption spectra of sodium hyponitrite and sodium α-oxyhyponitrite : the analysis of mixtures with sodium nitrite and nitrate. *J. Chem. Soc.* **1952**, 338–345.

[122] Bonner, F. T.; Ravid, B. Thermal decomposition of oxyhyponitrite (sodium trioxodinitrate(II)) in aqueous solution. *Inorg. Chem.* **1975**, *14*, 558–563.

[123] Zevallos, J.; Toro-Labbé, A.; Mó, O.; Yáñez, M. The Role of Intramolecular Hydrogen Bonds vs. Other Weak Interactions on the Conformation of Hyponitrous Acid and Its Mono- and Dithio-Derivatives. *Struct. Chem.* **2005**, *16*, 295–303.

[124] Montgomery, L. K.; Schueller, K.; Bartlett, P. D. Cycloaddition. II. Evidence of a Biradical Intermediate in the Thermal Addition of 1,1-Dichloro-2,2-difluoroethylene to the Geometrical Isomers of 2,4-Hexadiene. *J. Am. Chem. Soc.* **1964**, *86*, 622–628.

[125] Feldmann, C.; Jansen, M. Zur Kenntnis von cis-Natriumhyponitrit. *Z. Anorg. Allg. Chem.* **1997**, *623*, 1803–1809.

[126] Robinson, D. M.; Hoppe, T. J.; Paslay, T. J.; Purser, G. H. Kinetics and mechanism of the reduction of monochloramine by hydroxylamine and hydroxylammonium ion. *Int. J. Chem. Kinet.* **2006**, *38*, 124–135.

[127] Soni, V.; Mehrotra, R. N. Kinetics and mechanism of oxidation of hydroxylamine by tetrachloroaurate(III) ion. *Transit. Metal Chem.* **2003**, *28*, 893–898.

[128] Hughes, M. N.; Nicklin, H. G. Autoxidation of hydroxylamine in alkaline solutions. *J. Chem. Soc. A* **1971**, 164–168.

[129] Vincent, M. A.; Hillier, I. H.; Ge, J. How is N-N bond formation facilitated by P450 NO reductase? A DFT study. *Chem. Phys. Lett.* **2005**, *407*, 333 – 336.

[130] Xu, N.; Yi, J.; Richter-Addo, G. B. Linkage Isomerization in Heme-NOx Compounds: Understanding NO, Nitrite, and Hyponitrite Interactions with Iron Porphyrins. *Inorg. Chem.* **2010**, *49*, 6253–6266.

[131] Schopfer, M. P.; Wang, J.; Karlin, K. D. Bioinspired Heme, Heme/Nonheme Diiron, Heme/Copper, and Inorganic NO_x Chemistry: ·NO(g) Oxidation, PeroxynitriteMetal Chemistry, and ·NO(g) Reductive Coupling. *Inorg. Chem.* **2010**, *49*, 6267–6282.

[132] Blomberg, L. M.; Blomberg, M. R.; Siegbahn, P. E. Reduction of nitric oxide in bacterial nitric oxide reductase - a theoretical model study. *Biochim. Biophys. Acta* **2006**, *1757*, 240 – 252.

APPENDIX

A.1 MATLAB SOURCE CODE

Listing A.1: MATLAB implementation of the galatry profile function

```
function [y] = galatry(x,center,amp,coll,narrow,TEMPINP,molmas1)
% x=exp. frequency value; center=center of the line; amp=line center intensity
% coll=line brodening parameter (scaled with 2 * sqrt(ln2)) / FWHM Doppler
    width);
% narrow=line narrowing parameter (scaled with 2 * sqrt(ln2)) / FWHM Doppler
    width);
% TEMPINP=Temperature in K; molmas1=molecular mass of the absorber
N = 16384;
% Number of points of the time correlation function (Higher number increases
    accuarcy, should be chosen as a power of 2)
Time=200;
% Max. time of the time correlation function
doppler=7.1608E-7*center*sqrt(TEMPINP/molmas1)/2/sqrt(log(2));
% Doppler broadening
deltatau=Time/(N-1);
% Time interval of the correlation function
tau=(0:deltatau:Time)';
% Array of discrete time values
Correl = exp(-1.*coll*tau+1./(2.*narrow^2)*(1.-narrow*tau-exp(-narrow*tau)));
% Calculation of the time correlation function
basic=1./sqrt(pi)*real(fft(Correl,N));
% FFT of the time correlation function
freq=(0:(2*pi/Time):(N-1)*pi/Time);
% Frequency spacing of the Fourier transformed function
baseline=basic(N/2);
% Baseline of the calculated line profile function
value=amp*(basic(1:N/2)-baseline);
% Normalization and scaling of the profile
xnew=abs((x-center))/doppler;
% Rescaling of the experimental frequency values
if (xnew<(N-1)*pi/Time);
% Check whether the experimental value is within the frequency interval
    determied by the chosen parameters
y=interp1(freq,value,xnew);
% Calculation of the interpolated value of the profile function
else y=0; end;
% based on the code as described in Xiang Ouyang and Philip L. Varghese, "
    Reliable and efficient program for fitting Galatry and Voigt profiles to
    spectral data on multiple lines," Appl. Opt. 28, 1538-1545 (1989).
```

A.2 OPTIMIZED QUANTUM CHEMICAL STRUCTURES AND ENERGIES

A.2.1 *Optimized ground state structures*

The following Tables list (a) the optimized geometries of all intermediate species in solution (B3LYP/aug-cc-pVTZ/IEFPCM) and (b) the corresponding electronic energies and free enthalpies of formation in the gas phase and solution.

Table A.1: HNO (**1**).

	X	Y	Z
N	0.013997	0.000000	-0.000597
H	-0.005594	0.000000	1.053368
O	1.155806	0.000000	-0.372858

(a) Solution structure in Cartesian coordinates

	in Hartree	in kJ/mol
E_{gas}	-130.5276	-
E_{soln}	-130.5315	-
ΔE_{solv}	-0.0040	-10.4
ΔG^*_{gas}	-130.5350	-
ΔG^*_{soln}	-130.5387	-
ΔG^*_{solv}	-0.0038	-9.9

(b) Gas phase and solution energies

Table A.2: *cis*-NHONHO (**2**).

	X	Y	Z
N	0.000000	0.000000	0.000000
O	0.000000	0.000000	1.249027
H	0.870474	0.000000	-0.540388
N	-1.072332	0.000000	-0.726908
H	-0.891648	0.000000	-1.735242
O	-2.232615	0.000000	-0.264122

(a) Solution structure in Cartesian coordinates

	Hartree	kJ/mol
E_{gas}	-261.1001	-
E_{soln}	-261.1225	-
ΔE_{solv}	-0.0224	-58.9
ΔG^*_{gas}	-261.0878	-
ΔG^*_{soln}	-261.1096	-
ΔG^*_{solv}	-0.0218	-57.2

(b) Gas phase and solution energies

Table A.3: *trans*-NHONHO (**3**).

	X	Y	Z
N	0.000000	0.000000	0.000000
O	0.000000	0.000000	1.258331
H	0.869843	0.000000	-0.546627
N	-1.063158	0.000000	-0.729724
H	-1.933001	0.000000	-0.183096
O	-1.063158	0.000000	-1.988054

(a) Solution structure in Cartesian coordinates

	in Hartree	in kJ/mol
E_{gas}	-261.1025	-
E_{soln}	-261.1162	-
ΔE_{solv}	-0.0137	-35.9
ΔG^*_{gas}	-261.0903	-
ΔG^*_{soln}	-261.1034	-
ΔG^*_{solv}	-0.0130	-34.2

(b) Gas phase and solution energies

Table A.4: *cis*-NHONO$^-$ (**4**).

	X	Y	Z
N	-0.001820	0.000000	-0.014448
N	0.076776	0.000000	1.274710
O	1.108102	0.000000	-0.647040
O	1.135276	0.000000	2.031624
H	-0.840485	0.000000	1.714406

(a) Solution structure in Cartesian coordinates

	in Hartree	in kJ/mol
E_{gas}	-260.5729	-
E_{soln}	-260.6777	-
ΔE_{solv}	-0.1048	-275.2
ΔG^*_{gas}	-260.5739	-
ΔG^*_{soln}	-260.6782	-
ΔG^*_{solv}	-0.1043	-274.0

(b) Gas phase and solution energies

Table A.5: *trans*-NHONO$^-$ (**5**).

	X	Y	Z
N	-0.012968	0.000000	-0.033729
N	-0.049814	0.000000	1.242136
O	1.183316	0.000000	-0.524727
O	-1.134732	0.000000	1.966943
H	0.868509	0.000000	1.708631

(a) Solution structure in Cartesian coordinates

	in Hartree	in kJ/mol
E_{gas}	-260.5743	-
E_{soln}	-260.6726	-
ΔE_{solv}	-0.0983	-258.1
ΔG^*_{gas}	-260.5758	-
ΔG^*_{soln}	-260.6739	-
ΔG^*_{solv}	-0.0981	-257.6

(b) Gas phase and solution energies

Table A.6: *cis*-$NONO^{2-}$ (**6**).

	X	Y	Z
N	0.000000	0.000000	0.000000
N	0.000000	0.000000	1.276394
O	1.162585	0.000000	-0.677374
O	1.162585	0.000000	1.953768

(a) Solution structure in Cartesian coordinates

	in Hartree	in kJ/mol
E_{gas}	-259.8022	-
E_{soln}	-260.1744	-
ΔE_{solv}	-0.3723	-977.4
ΔG^*_{gas}	-259.8159	-
ΔG^*_{soln}	-260.1878	-
ΔG^*_{solv}	-0.3719	-976.3

(b) Gas phase and solution energies

Table A.7: *cis*-N(H)ONOH (**7**).

	X	Y	Z
N	-0.058829	0.000000	-0.009476
N	-0.008481	0.000000	1.255488
O	1.186656	0.000000	-0.530240
O	1.052869	0.000000	1.944734
H	-0.922569	0.000000	1.713051
H	1.797866	0.000000	0.247254

(a) Solution structure in Cartesian coordinates

	in Hartree	in kJ/mol
E_{gas}	-261.1337	-
E_{soln}	-261.1426	-
ΔE_{solv}	-0.0088	-23.2
ΔG^*_{gas}	-261.1208	-
ΔG^*_{soln}	-261.1298	-
ΔG^*_{solv}	-0.0090	-23.6

(b) Gas phase and solution energies

Table A.8: *cis*-NON(H)OH (**8**).

	X	Y	Z
N	0.032498	-0.144108	0.016624
N	-0.000213	-0.054043	1.297027
O	1.216643	-0.159390	-0.666358
O	1.131786	0.018475	1.819470
H	1.855621	-0.087810	0.083392
H	-0.809928	-0.216493	-0.535066

(a) Solution structure in Cartesian coordinates

	in Hartree	in kJ/mol
E_{gas}	-261.1299	-
E_{soln}	-261.1392	-
ΔE_{solv}	-0.0093	-24.4
ΔG^*_{gas}	-261.1195	-
ΔG^*_{soln}	-261.1285	-
ΔG^*_{solv}	-0.0089	-23.4

(b) Gas phase and solution energies

Table A.9: *trans*-NON(H)OH (**9**).

	X	Y	Z
N	0.129798	0.057047	0.194623
N	-0.100908	-0.251008	1.443705
O	1.298997	-0.406853	-0.356868
O	-1.247951	-0.016422	1.812260
H	1.889589	0.358969	-0.417426
H	-0.638120	0.254773	-0.447207

(a) Solution structure in Cartesian coordinates

	in Hartree	in kJ/mol
E_{gas}	-261.1200	-
E_{soln}	-261.1305	-
ΔE_{solv}	-0.0105	-27.5
ΔG^*_{gas}	-261.1097	-
ΔG^*_{soln}	-261.1204	-
ΔG^*_{solv}	-0.0108	-28.2

(b) Gas phase and solution energies

Table A.10: *trans*-N(H)ONOH (**10**).

	X	Y	Z
N	0.000031	0.000860	-0.000058
N	0.000016	0.000260	1.258067
O	1.324204	0.002154	-0.417886
O	-1.031592	-0.000953	1.966603
H	0.923241	0.000819	1.723332
H	1.255363	0.002727	-1.381342

(a) Solution structure in Cartesian coordinates

	in Hartree	in kJ/mol
E_{gas}	-261.1204	-
E_{soln}	-261.1321	-
ΔE_{solv}	-0.0117	-30.7
ΔG^*_{gas}	-261.1090	-
ΔG^*_{soln}	-261.1206	-
ΔG^*_{solv}	-0.0116	-30.5

(b) Gas phase and solution energies

Table A.11: *trans*-$NONO^{2-}$ (**11**).

	X	Y	Z
N	-0.000792	0.000000	-0.000008
N	0.000792	0.000000	1.255637
O	1.227964	0.000000	-0.568486
O	-1.227964	0.000000	1.824116

(a) Solution structure in Cartesian coordinates

	in Hartree	in kJ/mol
E_{gas}	-259.8094	-
E_{soln}	-260.1750	-
ΔE_{solv}	-0.3655	-959.7
ΔG^*_{gas}	-259.8233	-
ΔG^*_{soln}	-260.1884	-
ΔG^*_{solv}	-0.3651	-958.5

(b) Gas phase and solution energies

Table A.12: *cis*-NONOH$^-$ (**12**).

	X	Y	Z
N	0.046947	0.000000	0.000324
N	-0.024581	0.000000	1.258725
O	1.245313	0.000000	-0.534576
O	1.261522	0.000000	1.872715
H	1.827767	0.000000	1.052699

(a) Solution structure in Cartesian coordinates

	in Hartree	in kJ/mol
E_{gas}	-260.5987	-
E_{soln}	-260.6939	-
ΔE_{solv}	-0.0951	-249.8
ΔG^*_{gas}	-260.6002	-
ΔG^*_{soln}	-260.6955	-
ΔG^*_{solv}	-0.0952	-250.1

(b) Gas phase and solution energies

Table A.13: *cis*-NOHNOH (**13**).

	X	Y	Z
N	-0.000029	0.000000	0.014832
N	0.002715	0.000000	1.242146
O	1.206108	0.000000	-0.646114
H	1.916953	0.000000	0.021443
O	1.288399	0.000000	1.800033
H	1.124567	0.000000	2.752100

(a) Solution structure in Cartesian coordinates

	in Hartree	in kJ/mol
E_{gas}	-261.1429	-
E_{soln}	-261.1503	-
ΔE_{solv}	-0.0074	-19.6
ΔG^*_{gas}	-261.1318	-
ΔG^*_{soln}	-261.1394	-
ΔG^*_{solv}	-0.0076	-20.0

(b) Gas phase and solution energies

Table A.14: *trans*-NOHNOH (**14**).

	X	Y	Z
N	-0.058038	0.000000	-0.010861
N	0.022029	0.000000	1.210750
O	1.187893	0.000000	-0.592009
H	1.852190	0.000000	0.124025
O	-1.252818	0.000000	1.749995
H	-1.087596	0.000000	2.702539

(a) Solution structure in Cartesian coordinates

	in Hartree	in kJ/mol
E_{gas}	-261.1388	-
E_{soln}	-261.1470	-
ΔE_{solv}	-0.0082	-21.5
ΔG^*_{gas}	-261.1276	-
ΔG^*_{soln}	-261.1359	-
ΔG^*_{solv}	-0.0083	-21.8

(b) Gas phase and solution energies

Table A.15: *trans*-NONOH$^-$ (**15**).

	X	Y	Z
N	0.001651	0.000000	0.045977
N	0.068646	0.000000	1.297448
O	1.135678	0.000000	-0.580155
O	-1.263454	0.000000	1.835257
H	-1.842167	0.000000	1.051361

(a) Solution structure in Cartesian coordinates

	in Hartree	in kJ/mol
E_{gas}	-260.5823	-
E_{soln}	-260.6808	-
ΔE_{solv}	-0.0985	-258.7
ΔG^*_{gas}	-260.5845	-
ΔG^*_{soln}	-260.6831	-
ΔG^*_{solv}	-0.0986	-258.8

(b) Gas phase and solution energies

Table A.16: NNO (**16**).

	X	Y	Z
N	0.000000	0.000000	0.000000
N	0.000000	0.000000	1.119643
O	0.000000	0.000000	-1.183588

(a) Solution structure in Cartesian coordinates

	in Hartree	in kJ/mol
E_{gas}	-184.7380	-
E_{soln}	-184.7401	-
ΔE_{solv}	-0.0021	-5.5
ΔG^*_{gas}	-184.7482	-
ΔG^*_{soln}	-184.7503	-
ΔG^*_{solv}	-0.0022	-5.6

(b) Gas phase and solution energies

A.2.2 *Transition state structures of the initial HNO dimerization*

The following Tables list (a) geometry optimized TS structures of the initial dimerization reaction and (b) the corresponding electronic energies and free enthalpies of formation, as well as the sole imaginary frequency of the TS.

Table A.17: Gas phase transition state for reaction (**1**) ⇌ (**3**).

	X	Y	Z
N	-0.009195	-0.007735	-0.003208
O	-0.004531	-0.005550	1.198045
H	0.974204	-0.010390	-0.382159
N	-0.755713	-1.847509	-1.184564
H	-1.739113	-1.844853	-0.805613
O	-0.760377	-1.849694	-2.385817

(a) Gas phase structure in Cartesian coordinates

	in Hartree
E_{soln}	-261.0588
ΔG^*_{soln}	-261.0567
	in cm^{-1}
ν_{imag}	-60

(b) Gas phase energies and imaginary frequency

Table A.18: Transition state in solution for reaction (**1**) ⇌ (**3**).

	X	Y	Z
N	-0.002692	-0.006633	-0.008882
O	-0.010325	-0.008027	1.194910
H	0.981011	-0.006433	-0.375705
N	-0.760300	-1.860130	-1.203843
H	-1.743770	-1.860797	-0.836385
O	-0.753437	-1.858836	-2.407633

(a) Solution structure in Cartesian coordinates

	in Hartree
E_{soln}	-261.0643
ΔG^*_{soln}	-261.0637
	in cm^{-1}
ν_{imag}	-73

(b) Solution energies and imaginary frequency

A.2.3 *Transition state structures of cis-trans-isomerizations*

The following Tables list (a) the geometry optimized TS structures of all *cis-trans* isomerizations and (b) the corresponding electronic energies and free enthalpies of formation in solution, as well as the sole imaginary frequency of the TS.

Table A.19: Transition state for $NHONO^-$ (**4**,**5**) isomerization.

	X	Y	Z
N	-0.010200	0.026809	-0.146419
N	-0.386266	-0.073228	1.388074
O	1.154245	0.023403	-0.355944
O	0.223841	1.006747	2.005129
H	0.165621	-0.915578	1.622926

(a) Solution structure in Cartesian coordinates

	in Hartree
E_{soln}	-260.6071
ΔG^*_{soln}	-260.6112
	in cm^{-1}
ν_{imag}	-541

(b) Solution energies and imaginary frequency

Table A.20: Transition state for NON(H)OH (**8**,**9**) isomerization.

	X	Y	Z
N	0.008034	0.397767	-0.150174
N	-0.272476	0.069368	1.349576
O	1.167040	-0.402506	-0.395531
O	-0.000687	0.982179	2.026605
H	1.890227	0.236903	-0.377251
H	-0.721301	-0.149054	-0.610024

(a) Solution structure in Cartesian coordinates

	in Hartree
E_{soln}	-261.1024
ΔG^*_{soln}	-261.0925
	in cm^{-1}
ν_{imag}	-195

(b) Solution energies and imaginary frequency

Table A.21: Transition state for N(H)ONOH (**7**,**10**) isomerization.

	X	Y	Z
N	0.197394	-0.179500	0.140128
N	0.037016	0.052386	1.402759
O	1.462916	-0.012589	-0.466244
O	-0.318542	1.107520	1.904301
H	-0.006618	-0.755429	2.056208
H	1.854812	-0.899268	-0.481476

(a) Solution structure in Cartesian coordinates

	in Hartree
E_{soln}	-261.0376
ΔG^*_{soln}	-261.0283
	in cm^{-1}
ν_{imag}	-1296

(b) Solution energies and imaginary frequency

Table A.22: Transition state for $NONOH^-$ (**12**,**15**) isomerization.

	X	Y	Z
N	-0.006646	-0.235202	-0.038336
N	0.149301	-0.002084	1.355865
O	0.956720	0.056088	-0.715734
O	-0.354080	1.391486	1.509088
H	0.407011	1.946227	1.297573

(a) Solution structure in Cartesian coordinates

	in Hartree
E_{soln}	-260.5924
ΔG^*_{soln}	-260.5970
	in cm^{-1}
ν_{imag}	-1109

(b) Solution energies and imaginary frequency

A.2.4 *Transition state structures of direct hydrogen transfer reactions*

The following Tables list (a) the geometry optimized TS structures of all hydrogen transfer reactions and (b) the corresponding electronic energies and free enthalpies of formation in solution, as well as the sole imaginary frequency of the TS.

Table A.23: Transition state for reaction (**2**) ⇌ (**7**).

	X	Y	Z
N	0.017929	-0.013737	0.000105
N	0.006085	0.044240	1.285544
O	1.251020	0.023469	-0.605213
O	0.996952	-0.046332	2.023048
H	-0.940794	0.083988	1.678685
H	0.147093	0.699213	-0.881543

(a) Solution structure in Cartesian coordinates

	in Hartree
E_{soln}	-261.0424
ΔG^*_{soln}	-261.0360
	in cm^{-1}
ν_{imag}	-1898

(b) Solution energies and imaginary frequency

Table A.24: Transition state for reaction (**3**) ⇌ (**9**).

	X	Y	Z
N	-0.112871	0.041462	0.081722
N	-0.166793	-0.050388	1.363751
O	1.188698	0.055961	-0.229474
O	-1.161346	-0.095637	2.072777
H	-0.879203	0.092320	-0.585140
H	1.131515	-0.043719	1.164853

(a) Solution structure in Cartesian coordinates

	in Hartree
E_{soln}	-261.0663
ΔG^*_{soln}	-261.0599
	in cm^{-1}
ν_{imag}	-1792

(b) Solution energies and imaginary frequency

Table A.25: Transition state for reaction (**3**) ⇌ (**10**).

	X	Y	Z
N	-0.266839	-0.300211	0.152735
N	-0.041804	-0.029978	1.382285
O	0.766473	-0.000412	-0.728682
O	-0.873142	-0.082258	2.298043
H	0.953668	0.180816	1.580728
H	-0.538356	0.232043	-0.816620

(a) Solution structure in Cartesian coordinates

	in Hartree
E_{soln}	-261.0357
ΔG^*_{soln}	-261.0302
	in cm^{-1}
ν_{imag}	-1892

(b) Solution energies and imaginary frequency

Table A.26: Transition state for reaction (**9**) ⇌ (**14**).

	X	Y	Z
N	-0.002435	-0.001610	-0.001436
H	0.000141	-0.004937	1.264576
O	0.586861	-0.007121	-1.239296
H	1.345145	-0.604115	-1.148278
N	-1.213880	0.299630	0.101845
O	-1.365856	0.318915	1.405670

(a) Solution structure in Cartesian coordinates

	in Hartree
E_{soln}	-261.0803
ΔG^*_{soln}	-261.0753
	in cm^{-1}
ν_{imag}	-1814

(b) Solution energies and imaginary frequency

Table A.27: Transition state for reaction (**14**) ⇌ (**10**).

	X	Y	Z
N	-0.049113	-0.025459	-0.033498
N	-0.307646	-0.009475	1.169093
O	1.296325	0.014778	-0.300717
O	-1.590813	-0.042301	1.618896
H	-0.469470	0.013609	2.309028
H	1.787103	0.048848	0.541744

(a) Solution structure in Cartesian coordinates

	in Hartree
E_{soln}	-261.0497
ΔG^*_{soln}	-261.0452
	in cm^{-1}
ν_{imag}	-2018

(b) Solution energies and imaginary frequency

Table A.28: Transition state for reaction (**8**) ⇌ (**7**).

	X	Y	Z
N	-0.002925	0.000000	-0.051318
N	0.036701	0.000000	1.224135
O	1.220576	0.000000	-0.482258
O	1.232313	0.000000	1.784211
H	1.712305	0.000000	0.672068
H	-0.809534	0.000000	1.780916

(a) Solution structure in Cartesian coordinates

	in Hartree
E_{soln}	-261.1306
ΔG^*_{soln}	-261.1221
	in cm^{-1}
ν_{imag}	-1344

(b) Solution energies and imaginary frequency

Table A.29: Transition state for reaction (**7**) ⇌ (**13**).

	X	Y	Z
N	0.063267	-0.107497	-0.223928
N	-0.229337	-0.053189	0.978245
O	1.404858	-0.011991	-0.436102
O	0.723479	0.090806	1.964828
H	-0.573816	0.000333	2.074876
H	1.823310	0.081539	0.451285

(a) Solution structure in Cartesian coordinates

	in Hartree
E_{soln}	-261.0587
ΔG^*_{soln}	-261.0545
	in cm^{-1}
ν_{imag}	-2018

(b) Solution energies and imaginary frequency

Table A.30: Transition state for the intramolecular transfer in (**12**).

	X	Y	Z
N	-0.091004	0.000000	-0.049190
N	-0.090107	0.000000	1.216937
O	1.177814	0.000000	-0.546325
O	1.179532	0.000000	1.712076
H	1.628206	0.000000	0.582286

(a) Solution structure in Cartesian coordinates

	in Hartree
E_{soln}	-260.6882
ΔG^*_{soln}	-260.6930
	in cm^{-1}
ν_{imag}	-1194

(b) Solution energies and imaginary frequency

A.2.5 *Transition state structures of decomposition reactions*

The following Tables list (a) the geometry optimized TS structures of all decomposition reactions and (b) the corresponding electronic energies and free enthalpies of formation in solution, as well as the sole imaginary frequency of the TS.

Table A.31: Transition state for reaction (**9**) $\rightleftharpoons$ (**16**).

	X	Y	Z
N	0.000000	0.000000	0.000000
N	0.000000	0.000000	1.311026
O	1.613907	0.000000	-0.380143
O	-1.129638	-0.159005	1.768625
H	1.605296	0.542652	-1.188223
H	0.730642	-0.820174	-0.510491

(a) Solution structure in Cartesian coordinates

	in Hartree
E_{soln}	-261.0435
ΔG^*_{soln}	-261.0403
	in cm^{-1}
ν_{imag}	-1781

(b) Solution energies and imaginary frequency

Table A.32: Transition state for reaction (**10**) $\rightleftharpoons$ (**16**).

	X	Y	Z
N	-0.022422	0.023797	0.030119
N	-0.020095	0.004201	1.314781
O	1.481738	0.007370	-0.081637
O	-1.049245	0.064061	1.982020
H	1.355800	-0.054563	1.119957
H	1.727203	-0.851525	-0.471599

(a) Solution structure in Cartesian coordinates

	in Hartree
E_{soln}	-261.0752
ΔG^*_{soln}	-261.0688
	in cm^{-1}
ν_{imag}	-1525

(b) Solution energies and imaginary frequency

Table A.33: Transition state for reaction (**13**) ⇌ (**16**).

	X	Y	Z
N	-0.011523	-0.003726	0.006938
N	0.001429	0.002538	1.205327
O	1.114766	0.004081	1.868885
O	1.667525	0.056493	-0.380422
H	1.794616	-0.021879	0.786325
H	1.801494	-0.798442	-0.815750

(a) Solution structure in Cartesian coordinates

	in Hartree
E_{soln}	-261.1212
ΔG^*_{soln}	-261.1153
	in cm^{-1}
ν_{imag}	-1265

(b) Solution energies and imaginary frequency

Table A.34: Transition state for the decomposition of (**12**).

	X	Y	Z
N	0.035040	0.000000	0.043084
N	-0.005564	0.000000	1.211225
O	0.877012	0.000000	-0.887121
O	1.776072	0.000000	1.947970
H	2.281901	0.000000	1.125681

(a) Solution structure in Cartesian coordinates

	in Hartree
E_{soln}	-260.6777
ΔG^*_{soln}	-260.6832
	in cm^{-1}
ν_{imag}	-330

(b) Solution energies and imaginary frequency

Table A.35: Transition state for the decomposition of (**15**).

	X	Y	Z
N	0.055080	0.000000	0.129499
N	0.160097	0.000000	1.288478
O	0.837815	0.000000	-0.886419
O	-1.600370	0.000000	2.040415
H	-2.064788	0.000000	1.193328

(a) Solution structure in Cartesian coordinates

	in Hartree
E_{soln}	-260.6488
ΔG^*_{soln}	-260.6551
	in cm^{-1}
ν_{imag}	-500

(b) Solution energies and imaginary frequency

A.2.6 *Transition state structures of water assisted hydrogen transfer reactions*

The following Tables list (a) the geometry optimized TS structures of all water assisted hydrogen transfer reactions and (b) the corresponding electronic energies and free enthalpies of formation in solution, as well as the sole imaginary frequency of the TS.

Table A.36: Water assisted transition state for reaction (**3**) ⇌ (**9**).

	X	Y	Z
N	0.089019	0.042886	-0.050652
H	0.009110	0.019090	1.332925
O	1.024681	-0.028146	-0.883819
N	-1.112954	0.205931	-0.471147
O	-2.148727	0.290434	0.342625
H	-0.447433	0.773630	2.865921
O	-0.633539	0.016337	2.292300
H	-1.493537	0.192565	1.723449
H	-1.260495	0.270345	-1.481259

(a) Solution structure in Cartesian coordinates

	in Hartree
E_{soln}	-337.5820
ΔG^*_{soln}	-337.5528
	in cm^{-1}
ν_{imag}	-959

(b) Solution energies and imaginary frequency

Table A.37: Water assisted transition state for reaction (**3**) ⇌ (**10**).

	X	Y	Z
N	-0.061780	0.004064	0.059602
N	0.068047	0.010997	1.322208
O	0.901144	0.028525	-0.778041
O	-1.042547	-0.020776	2.008412
H	1.354118	0.030678	2.158465
O	-0.059174	-0.046834	4.418185
H	-0.284101	0.723254	4.952531
H	-0.606541	-0.005868	3.566267
O	1.963421	0.082262	3.029841
H	1.209189	0.026763	3.795307
H	2.557786	-0.680626	3.073267
H	-1.034906	-0.024069	-0.275687

(a) Solution structure in Cartesian coordinates

	in Hartree
E_{soln}	-414.0703
ΔG^*_{soln}	-414.0183
	in cm^{-1}
ν_{imag}	-169

(b) Solution energies and imaginary frequency

Table A.38: Water assisted transition state for reaction (**9**) ⇌ (**14**).

	X	Y	Z
N	-0.014886	-0.026027	-0.015488
H	-0.009946	-0.029761	1.312728
O	0.997599	-0.089690	-0.967429
H	1.753152	-0.446715	-0.481395
N	-1.132951	0.208249	-0.534372
O	-2.103683	0.326162	0.322238
H	-0.437816	0.782216	2.855502
O	-0.649297	0.012636	2.307985
H	-1.494787	0.212783	1.716412

(a) Solution structure in Cartesian coordinates

	in Hartree
E_{soln}	-337.5914
ΔG^*_{soln}	-337.5642
	in cm^{-1}
ν_{imag}	-1154

(b) Solution energies and imaginary frequency

Table A.39: Water assisted transition state for reaction (**14**) ⇌ (**10**).

	X	Y	Z
N	0.106475	-0.019627	0.058670
N	-0.000757	-0.025293	1.295073
O	1.486941	0.011268	-0.248319
O	-1.218565	-0.054732	1.769194
H	1.079137	-0.015553	2.399201
H	1.486427	0.015316	-1.213144
O	-0.766050	-0.073284	4.284283
H	-1.090328	0.709353	4.744209
H	-1.101162	-0.037610	3.310320
O	1.491520	0.036895	3.380872
H	0.567618	-0.014281	3.969821
H	2.060929	-0.726974	3.548539

(a) Solution structure in Cartesian coordinates

	in Hartree
E_{soln}	-414.0828
ΔG^*_{soln}	-414.0321
	in cm^{-1}
ν_{imag}	-303

(b) Solution energies and imaginary frequency

Table A.40: Water assisted transition state for reaction (**7**) ⇌ (**13**).

	X	Y	Z
N	0.073055	-0.032802	0.032908
N	-0.059752	-0.025343	1.276274
O	1.399397	0.001273	-0.373907
O	1.028040	0.013810	2.026894
H	-1.407833	-0.034865	2.119731
H	1.892923	0.024531	0.481082
O	-0.027945	0.039407	4.360061
H	0.171996	-0.733181	4.901785
H	0.548768	0.000646	3.512827
O	-2.005545	-0.084784	2.975159
H	-1.203895	-0.027764	3.765344
H	-2.598868	0.678391	3.009180

(a) Solution structure in Cartesian coordinates

	in Hartree
E_{soln}	-414.0931
$\Delta G^{*}_{\text{soln}}$	-414.0420
	in cm^{-1}
ν_{imag}	-364

(b) Solution energies and imaginary frequency

Table A.41: Water assisted transition state for reaction (**10**) ⇌ (**16**).

	X	Y	Z
N	-0.130960	-0.003526	-0.054592
N	-0.115689	-0.050216	1.206761
O	1.312871	-0.060975	-0.490142
O	-1.260087	-0.068736	1.755703
H	1.615448	0.204868	2.004309
H	1.354708	0.569901	-1.222602
O	2.508985	0.270591	1.568080
H	2.905346	1.132359	1.770460
H	2.104495	0.201278	0.504351

(a) Solution structure in Cartesian coordinates

	in Hartree
E_{soln}	-337.5791
$\Delta G^{*}_{\text{soln}}$	-337.5508
	in cm^{-1}
ν_{imag}	-389

(b) Solution energies and imaginary frequency

Table A.42: Water assisted transition state for reaction (**13**) $\rightleftharpoons$ (**16**).

	X	Y	Z
N	0.025401	-0.036275	-0.023003
N	-0.020231	-0.120960	1.160638
O	0.992780	0.142245	-0.858848
H	2.074849	0.737451	-0.337915
O	1.535621	-0.043703	1.901797
H	1.262505	0.236940	2.783304
O	2.841954	1.228847	0.300720
H	3.724196	0.880458	0.113472
H	2.442455	0.771964	1.181308

(a) Solution structure in Cartesian coordinates

	in Hartree
E_{soln}	-337.6013
$\Delta G^{*}_{\text{soln}}$	-337.5748
	in cm^{-1}
ν_{imag}	-806

(b) Solution energies and imaginary frequency

ACKNOWLEDGMENTS (IN GERMAN)

Abschließend möchte ich mich bei allen bedanken, die zu dieser Arbeit in der einen oder anderen Weise beigetragen haben. Im speziellen gilt mein Dank:

- Meinem Betreuer Prof. Dr. Gernot Friedrichs für die Möglichkeit diese Arbeit in seinem Arbeitskreis anzufertigen zu können. Die offene Diskussionsbereitschaft für Fachliches, der stetig vermittelte Optimismus zur Lösung anliegender Probleme, berechtige kritische Anmerkungen und die Unterstützung bei grundsätzlichen Fragestellungen haben zweifellos die Erstellung dieser Arbeit beflügelt.

- Meinen zusätzlichen Betreuern im Rahmen der ISOS, Prof. Dr. Friedrich Temps und Prof. Dr. Douglas Wallace, für Ihre Zeit und Mühe, die sie in die durchgeführten Advisory Group Meetings investiert haben. Insbesondere zu Beginn halfen die Anmerkungen und Kommentare dabei potenziell interessante Aspekte der Arbeit herauszuarbeiten.

- Prof. Dr. Martin Beyer und dessen Arbeitskreis insbesondere Christian van der Linde für die hochauflösenden FT-ICR-MS-Messungen, die eine detaillierte Charakterisierung der angereicherten Isotopomerenproben erst ermöglichten.

- Prof. Dr. Frank Sönnichsen und Mitarbeitern der spektroskopischen Abteilung der organischen Chemie für die durchgeführten ^{1}H-, ^{14}N- und ^{15}N-NMR-Messungen und die anregende und konstruktive Diskussion der erhaltenen Spektren.

- PD Dr. Avan Antia und dem gesamten ISOS-Team für den engagierten Aufbau und die vielfältigen, informativen Veranstaltungen und Angebote des Graduiertenprogrammes.

- Dr. Jan Kaiser von der University of East Angelia, für die Zurverfügungstellung der N_2O Standardproben und die IRMS-Messungen des Referenzgases CAU-I, das im Rahmen dieser Arbeit zu Testzwecken verwendet worden ist.

- PD Dr. Hermann Bange für weiterführende Diskussionen und Literatur zur N_2O Thematik.

- Dr. Joachim Gripp für viele gute und pragmatische Ratschläge und Unterweisungen im Umgang mit Spektrometern, Vakuumtechnik und Chemikalien.

- Kerstin Mühlig und Dr. Icksoon Park der Firma Sacher Lasertechnik, die mir die Eigenheiten von Diodenlasern vor Augen führten und mit denen es immer eine Freude war die anfallende Laserprobleme zu diskutieren und zu lösen.

- Dr. Carolin Löscher für die Durchführung von Inkubationsexperimenten mit verschiedenen Kulturen zur Darstellung von ^{15}N-isotopen angereichertem N_2O und einen anregenden wie auch informativen Gedankenaustausch, der mir die Perspektive der Mikrobiologie etwas näher brachte.

- Meinen Laborkollegen, Dr. Kristian Lass und Joscha Kleber, für die verlässlichen Absprachen und das aufgebrachte Verständnis, wenn erstere für kurzfristige Messungen noch einmal geändert werden mussten.

- Meinen Büronachbarn, Dr. Johannes Dammeier und Nancy Fassheber, für vielfältige, kurzweilige Gespräche und fachliche Diskussionen sowie Nancy Fassheber im speziellen für das abschließende Korrekturlesen dieser Arbeit.

- Dem gesamten AK Friedrichs und AK Temps für diverse gemeinsame Veranstaltungen und das Glück einige sehr bewundernswerte Charakterzüge zu erleben, deren angemessene Wertschätzung ich häufig nicht genüge getan habe. An dieser Stelle sei insbesondere auch Dr. Ron Siewertsen, Thomas Michalak und Mayra Stuhldreier gedankt, die individuell und gemeinsam zur Steigerung meiner Arbeitsmoral beigetragen haben.

- Den Mitarbeitern der Institutswerkstatt, Klaus-Dieter Will, Frank Herzog, Frank Laasch, Olaf Wendt und Andreas Sievers, sowie Michael Karstens für eine Vielzahl von Aufbauten und kurzfristigen Problemlösungen im Rahmen dieser Arbeit. Insbesondere die detaillierten Planungen und technischen Zeichnungen, die teils aufwendige Bearbeitung und die weitergehenden Ideen (Lackierung, spezielle Halterungen), die in den Aufbau des CRD Spektrometers eingegangen sind, verdienen meinen aufrichtigsten Dank.

- Den Elektronikern, Klaus Warns für die tadellose, maßgeschneiderte Fertigung der zahlreichen elektronischen Komponenten des Versuchsaufbaus und Uwe Eggers für die Hilfe bei speziellen Soft- und Hardwareproblemen.

- Der Deutschen Forschungsgemeinschaft im Rahmen des Excellenzclusters "The Future Ocean" und des SFB 677 sowie dem Land Schleswig-Holstein für die Finanzierung.

- Meiner Familie und Freunden für die anhaltende vielfältige Unterstützung, den notwendigen Ausgleich und viel Verständnis über die gesamte Zeit.

PUBLICATION LIST

Some ideas and figures have appeared previously in the following publications and conference contributions:

JOURNAL ARTICLES

1. Carsten Fehling and Gernot Friedrichs, *A precise high-resolution near infrared continuous wave cavity ringdown spectrometer using a fourier transform based wavelength calibration*, *Rev. Sci. Instrum.* **2010**, *81*, 053109.
doi: 10.1063/1.3422254
http://link.aip.org/link/doi/10.1063/1.3422254

2. Carsten Fehling and Gernot Friedrichs, *Dimerization of HNO in Aqueous Solution: An Interplay of Solvation Effects, Fast Acid Base Equilibria, and Intramolecular Hydrogen Bonding?*, *J. Am. Chem. Soc.* **2011**, *133*, 17912-17922.
doi: 10.1021/ja2075949
http://dx.doi.org/10.1021/ja2075949

CONFERENCE CONTRIBUTIONS

1. C. Fehling and G. Friedrichs, "Origin of ^{15}N site selectivity in nitrous oxide from HNO dimerization in aqueous solution", Poster presentation at 110^{th} Bunsentagung in Berlin, Germany, June 2011.

2. C. Fehling and G. Friedrichs, "Formation Process Induced Site-Preference of Nitrous Oxide Studied by High Resolution Near Infrared *cw* Cavity Ringdown Spectroscopy", Talk at 5^{th} International Symposium on Isotopomers in Amsterdam, The Netherlands, June 2010.

3. C. Fehling and G. Friedrichs, "High Resolution Near Infrared Cavity Ringdown Spectroscopy for Site Preference Determination of Nitrous Oxide", Talk at 109^{th} Bunsentagung 2010 in Bielefeld, Germany, May 2010.

4. C. Fehling and G. Friedrichs, "A New High-Resolution Detection Scheme for Isotopomeric Ratio Measurements of N_2O Based on Near-Infrared Cavity Ringdown Spectroscopy", Poster presentation at SOLAS Open Science Conference 2009 in Barcelona, Spain, November 2009.

5. C. Fehling and G. Friedrichs, "Application of *cw*-CRDS in the Near Infrared (1625 - 1690 nm) for Marine Trace Gas Detection", Poster presentation at 108^{th} Bunsentagung 2009 in Cologne, Germany, May 2009.

6. G. Friedrichs, J. Bock, and C. Fehling, "NIR-*cw*-(*ew*)-CRDS: A Tool for Monitoring Isotope Ratios and Heterogeneous Chemistry", Talk at European Geosciences Union (EGU) General Assembly 2009 in Vienna, Austria, April 2009.

7. C. Fehling and G. Friedrichs, "Near-Infrared Cavity Ringdown Spectroscopy: From the Gas Phase to the Interface", Poster presentation at 107^{th} Bunsentagung 2008 in Saarbrücken, Germany, May 2008.

8. C. Fehling, G. Friedrichs, and F. Temps, "Set-up of a Near-Infrared Cavity Ringdown Spectrometer for Quantitative Surface Coverage Measurements on Quartz Glass", Poster presentation at 7^{th} Cavity Ring-Down User Meeting in Greifswald, Germany, September 2007.

DECLARATION

I hereby declare that the work presented in this thesis was prepared and worked out by myself with no other help than the referenced sources except for guidance of my supervisor Prof. Dr. Gernot Friedrichs.

This is my first dissertation and this work has neither been used as a whole nor in parts in any other dissertation attempts.

The dissertation complies to the good scientific practice rules as proposed by the German Research Foundation (DFG).

Kiel, 2012

Carsten Fehling